Chapter 1

INTRODUCTION

1.1 Introduction

Recently, optical microfibers have attracted growing interest to its vast potential as building components for photonic devices and integrated photonic system. They offer many unique characteristics such as strong evanescent field, flexible, high nonlinearity, high configurability, and controllable dispersion. Recent development in low-loss microfibers has opened up new opportunities for various micro-photonic devices including microresonators [1], fiber couplers [2], and industrial sensors [3, 4] using microfibers. Biconical tapered fibers that preserve their low loss connection with the original single mode fibers (SMF) provide the greatest advantage of achieving low-loss micro-photonic devices. The performance of these microfiber devices is comparable with the optical planar waveguides [5]. Generally, micro-photonic devices are fabricated using lithographic technique that involves expensive fabrication process but they suffer from high losses in coupling with fibers and poor wall surface roughness. As a fundamental functional block, microfiber structures in the forms of loop, knot and coil, have shown unique optical quality. A microfiber loop resonator (MLR) with a Q-factor of 120,000 has been demonstrated [6]. In addition, microfiber based devices have exhibited promising potential in numerous applications including optical communications, laser systems [7], optical signal processing [8, 9], spectroscopy, industrial sensors for temperature, refractive index, chemistry, biomedical and pressure.

In this thesis, the work mainly focuses on microfiber devices which are made of microfibers. The main objective of this research is to develop the understanding of

microfiber devices ranging from the waveguide characteristics to the theory, from design to fabrication of these microfiber devices.

1.2 Recent Development of Microfiber Devices

There has been a great deal of resources and efforts put into development of microfiber devices and exploration of their characteristics and potential in applications. The most common optical components made of microfibers are optical fiber couplers which have been commercially available for decades. When two microfibers are put in close contact, the strong evanescent fields of these two microfibers allow exchange of energy between them. Splitting or combining of light power can be realized in fibers using fiber couplers. The same mechanism is involved in many other optical microfiber devices such as MLR [10, 11], microfiber coil resonator (MCR) [5, 12-14], microfiber knot resonator (MKR) [1, 3, 15], reef knot microfiber resonator as an add/drop filter [16], microfiber Mach-Zehnder interferometer (MMZI) [17, 18], microfiber loop mirror [19] and etc.

Most of these microfiber devices have exhibited promising functionalities in a variety of applications such as sensors, miniature lasers [7, 20], optical filters [16, 21] and dispersion compensating [22, 23]. Among all, sensors are the major applications of most microfiber devices [4, 6, 14, 15, 24-31]. Microfibers are ultra-sensitive to condition of ambient mediums due to their strong evanescent field; however it is difficult to exploit this property without integrating them with external interferometry or making them as parts of interferometer or resonator configurations. The fringes in the transmission spectra of microfiber resonator and interferometers are the output result of wave interference within the microfiber structures. Any changes in a form of refractive index [14, 26], temperature [4, 15] and amount of chemical substance or molecules [24, 31] in the gas or liquid near in surrounding of microfibers can be seen from

transmission spectra of the microfiber devices. Numerous sensors have been developed based on these properties such as biomedical sensor, humidity sensors, chemical sensors, current sensor and etc. Generally, the sensing results can be collected based on the variations in three characteristics of the transmission spectra in response to the sensing subjects, they are free spectral range (FSR) [32], resonance wavelength shift [3, 4, 15] and extinction ratio [6]. The sensing results can be generated from one or the combination of two or three of the characteristics depending on the requirement of the users.

1.3 Objectives

The main objective of this work is to master the fabrication techniques, understand the characteristics and explore the potential applications of microfiber devices. The work begins with the fabrication of adiabatic tapered fibers where the optimal shapes of tapers should meet certain specifications to minimize the insertion loss of the tapered fibers. Several aspects related to the fabrication technique are fathomed and implemented precisely to ensure fabrication of good quality tapered fibers. Adiabatic tapered fibers are employed in the fabrication of various optical microfiber devices such as MLR, MKR and MMZI. To protect the microfibers and microfiber devices from the environmental perturbations, some protective measures are taken and investigated. In the characterization of these microfiber devices, the analysis of their experimental data is accompanied by theoretical models to provide more in-depth understanding and explanation on the characteristics of these microfiber devices such as the transmission spectra, resonance condition, coupling ratio, temperature response, polarization dependent characteristics and etc. In the analytical study and characterization of this research, quantitative analysis on the experimental data is carried out using several softwares such as Matlab and Microsoft Excel. Lastly, the new

applications of microfiber devices are also explored and demonstrated. By exploiting their unique characteristics, the microfiber devices are deployed in the applications namely multiwavelength laser system, temperature sensor and current sensor.

1.4 Thesis Outline

This thesis presents research works on microfibers, microfiber devices and their applications. This work covers from the fabrication of the adiabatic tapered fibers until the applications of microfiber devices. The demonstration of the fabrication and theoretical analysis on the characteristic of the microfiber devices are presented in detail. One of chapters in the thesis presents the applications of the microfiber devices. The following is the thesis outline: -

Chapter 2 presents the literature reviews on fabrication techniques of microfibers and their important optical properties. Some of the important functionalities and applications of these devices are reviewed in the chapter. Chapter 3 demonstrates the fabrication techniques for tapered fiber especially on the flame brushing technique. The theory of adiabaticity and optimal shape for tapered fiber are discussed. Several different taper profiles are experimentally demonstrated based on different parameters in the tapering process. To counter the aging effect on tapered fiber in the air, two protective measures are introduced and investigated in this chapter. In Chapter 4, the experimental demonstration of several microfiber devices are presented, namely MLR, MKR and MMZI. The fabrication techniques and procedures are presented in detail. To achieve better understanding of the microfiber devices' characteristics, theoretical model of each microfiber device is incorporated in the analysis and compared with the experimental result. Chapter 5 presents the application of microfiber resonators. Microfiber resonator with a small FSR makes a good optical filter for multiwavelength laser system. Besides that, new temperature sensor and current sensor [3] based on

microfiber knot resonators are presented in this chapter. This work is concluded in Chapter 6.

References

[1] X. Jiang, L. Tong, G. Vienne, X. Guo, A. Tsao, Q. Yang, and D. Yang, "Demonstration of optical microfiber knot resonators," *Applied Physics Letters*, vol. 88, no. 22, pp. 223501-223501-3, 2006.

[2] Y. Jung, G. Brambilla, and D. J. Richardson, "Optical microfiber coupler for broadband single-mode operation," *Opt. Express*, vol. 17, no. 7, pp. 5273-5278, 2009.

[3] K. S. Lim, S. W. Harun, S. S. A. Damanhuri, A. A. Jasim, C. K. Tio, and H. Ahmad, "Current sensor based on microfiber knot resonator," *Sensors and Actuators A: Physical*, vol. 167, no. 1, pp. 377–381, 2011.

[4] X. Zeng, Y. Wu, C. Hou, J. Bai, and G. Yang, "A temperature sensor based on optical microfiber knot resonator," *Optics Communications*, vol. 282, no. 18, pp. 3817-3819, 2009.

[5] M. Sumetsky, "Basic Elements for Microfiber Photonics: Micro/Nanofibers and Microfiber Coil Resonators," *J. Lightwave Technol.*, vol. 26, no. 1, pp. 21-27, 2008.

[6] M. Sumetsky, Y. Dulashko, J. M. Fini, A. Hale, and D. J. DiGiovanni, "The microfiber loop resonator: theory, experiment, and application," *Lightwave Technology, Journal of*, vol. 24, no. 1, pp. 242-250, 2006.

[7] X. Jiang, Q. Song, L. Xu, J. Fu, and L. Tong, "Microfiber knot dye laser based on the evanescent-wave-coupled gain," *Applied Physics Letters*, vol. 90, no. 23, pp. 233501-3, 2007.

[8] K. Amarnath, R. Grover, S. Kanakaraju, and H. Ping-Tong, "Electrically pumped InGaAsP-InP microring optical amplifiers and lasers with surface passivation," *Photonics Technology Letters, IEEE*, vol. 17, no. 11, pp. 2280-2282, 2005.

[9] S. W. Harun, K. S. Lim, A. A. Jasim, and H. Ahmad, "Dual wavelength erbium-doped fiber laser using a tapered fiber," *Journal of Modern Optics,* vol. 57, no. 21, pp. 2111 - 2113, 2010.

[10] S. Harun, K. Lim, A. Jasim, and H. Ahmad, "Fabrication of tapered fiber based ring resonator," *Laser Physics,* vol. 20, no. 7, pp. 1629-1631, 2010.

[11] M. Sumetsky, Y. Dulashko, J. M. Fini, and A. Hale, "Optical microfiber loop resonator," *Applied Physics Letters,* vol. 86, no. 16, pp. 161108-161108-3, 2005.

[12] M. Sumetsky, Y. Dulashko, and S. Ghalmi, "Fabrication of miniature optical fiber and microfiber coils," *Optics and Lasers in Engineering,* vol. 48, no. 3, pp. 272-275, 2010.

[13] F. Xu and G. Brambilla, "Embedding optical microfiber coil resonators in Teflon," *Opt. Lett.,* vol. 32, no. 15, pp. 2164-2166, 2007.

[14] F. Xu, P. Horak, and G. Brambilla, "Optical microfiber coil resonator refractometric sensor," *Opt. Express,* vol. 15, no. 12, pp. 7888-7893, 2007.

[15] Y. Wu, Y.-J. Rao, Y.-h. Chen, and Y. Gong, "Miniature fiber-optic temperature sensors based on silica/polymer microfiber knot resonators," *Opt. Express,* vol. 17, no. 20, pp. 18142-18147, 2009.

[16] G. Vienne, A. Coillet, P. Grelu, M. El Amraoui, J.-C. Jules, F. Smektala, and L. Tong, "Demonstration of a reef knot microfiber resonator," *Opt. Express,* vol. 17, no. 8, pp. 6224-6229, 2009.

[17] Y.-H. W. Chen, Yu; Rao, Yun-Jiang; Deng, Qiang; Gong, Yuan, "Hybrid Mach-Zehnder interferometer and knot resonator based on silica microfibers," *Optics Communications,* vol. 283, no. 14, p. 4, 2010.

[18] Y. Li and L. Tong, "Mach-Zehnder interferometers assembled with optical microfibers or nanofibers," *Opt. Lett.,* vol. 33, no. 4, pp. 303-305, 2008.

[19] S.-S. Wang, Z.-F. Hu, Y.-H. Li, and L.-M. Tong, "All-fiber Fabry-Perot resonators based on microfiber Sagnac loop mirrors," *Opt. Lett.,* vol. 34, no. 3, pp. 253-255, 2009.

[20] J. Xiaoshun, T. Limin, S. Qinghai, and X. Lei, "Evanescent-Wave Pumped Microfiber Knot Laser," in *Lasers and Electro-Optics, 2007. CLEO 2007. Conference on,* 2007, pp. 1-2.

[21] X. Jiang, Y. Chen, G. Vienne, and L. Tong, "All-fiber add-drop filters based on microfiber knot resonators," *Opt. Lett.,* vol. 32, no. 12, pp. 1710-1712, 2007.

[22] C. K. Madsen and G. Lenz, "Optical all-pass filters for phase response design with applications for dispersion compensation," *Photonics Technology Letters, IEEE,* vol. 10, no. 7, pp. 994-996, 1998.

[23] O. Schwelb, "Transmission, group delay, and dispersion in single-ring optical resonators and add/drop filters-a tutorial overview," *Lightwave Technology, Journal of,* vol. 22, no. 5, pp. 1380-1394, 2004.

[24] J. M. Corres, I. R. Matias, J. Bravo, and F. J. Arregui, "Tapered optical fiber biosensor for the detection of anti-gliadin antibodies," *Sensors and Actuators B: Chemical,* vol. 135, no. 1, pp. 166-171, 2008.

[25] F. Gu, L. Zhang, X. Yin, and L. Tong, "Polymer Single-Nanowire Optical Sensors," *Nano Letters,* vol. 8, no. 9, pp. 2757-2761, 2008.

[26] X. Guo and L. Tong, "Supported microfiber loops for optical sensing," *Opt. Express,* vol. 16, no. 19, pp. 14429-14434, 2008.

[27] E. Harris, Y. Li, L. Chen, and X. Bao, "Fiber-optic Mach-Zehnder interferometer as a high-precision temperature sensor: effects of temperature fluctuations on surface biosensing," *Appl. Opt.,* vol. 49, no. 29, pp. 5682-5685, 2010.

[28] S. Soria, S. Berneschi, M. Brenci, F. Cosi, G. Nunzi Conti, S. Pelli, and G. C. Righini, "Optical Microspherical Resonators for Biomedical Sensing," *Sensors*, vol. 11, no. 1, pp. 785-805, 2011.

[29] M. Sumetsky, R. S. Windeler, Y. Dulashko, and X. Fan, "Optical liquid ring resonator sensor," *Opt. Express*, vol. 15, no. 22, pp. 14376-14381, 2007.

[30] F. Xu, V. Pruneri, V. Finazzi, and G. Brambilla, "An embedded optical nanowire loop resonator refractometric sensor," *Opt. Express*, vol. 16, no. 2, pp. 1062-1067, 2008.

[31] J. Yang and L. J. Guo, "Optical sensors based on active microcavities," *Selected Topics in Quantum Electronics, IEEE Journal of*, vol. 12, no. 1, pp. 143-147, 2006.

[32] W. Yu, Z. Xu, H. Changlun, B. Jian, and Y. Guoguang, "A tunable all-fiber filter based on microfiber loop resonator," *Applied Physics Letters*, vol. 92, no. 19, pp. 191112-2, 2008.

Chapter 2

LITERATURE REVIEW

2.1 Introduction

Tapered fibers come under different names for instance subwavelength wires, fiber tapers, micro- / nanowires, sub-micron diameter fibers, microfibers and nanofibers. They can be fabricated from single-mode fibers or bulk glass [1] and their diameters are in the range of several tens of nanometers to several microns. Due to the small core diameter, the large index contrast between the glass and surrounding medium enables strong confinement of light within the core of the tapered fiber. Besides, there are many other interesting properties such as strong evanescent field, large dispersion / dispersion slope, strong near field interaction, capable of small bending radius and etc. In this chapter, the background theories are reviewed and discussed. In the first section, the development of tapered fibers ranging from the fabrication techniques to the optical properties is discussed. In the following section, the applications and functionalities of tapered fibers are reviewed.

2.2 Fabrication techniques

Throughout the years of development, several fabrication techniques for microfibers have been suggested. One of these techniques is chemical etching which uses hydrofluoric acid as an etchant for silica fiber. The greatest advantage of this technique is its capability for simultaneous production where more than one and within an acceptable number of conical tapered fibers can be produced simultaneous using the same pool of etchant solution [2-4]. However, fabrication of biconical tapered fibers by

chemical etching requires a modified fabrication rig [5]. The setbacks in chemical etching technique includes the poor surface roughness, the difficulty in controlling the shape of the taper and achieving long taper waist. Electric arc [6] has also been suggested for the fabrication of tapered fiber but only limited length of tapered fiber can be produced using this technique due to the restriction of the fabrication rig. Sumetsky et. al. uses CO_2 laser to fabricate micro / nanofibers. In this technique, a single mode fiber (SMF) is inserted into a sapphire tube which is then exposed to the radiation [7]. The radiated sapphire tube acts as a microfurnace which can produce a micro / nanofiber. With the proper control of the beam size of the laser, position and elongation of the SMF, the tapered fiber can be shaped into the desired form. Symmetrical biconical tapered fiber with a waist length of around 6mm had been demonstrated using this method. Besides tapered fibers, CO_2 laser can also be employed to fabricate miniatured devices such as fused fiber microcoupler, long period grating on a microtaper and whispering gallery mode microcavity [8, 9]. Low loss splicing for two microfibers can be done using CO_2 laser[10]. In the effort to fabricate nanofiber, Tong et. al. [11] has developed a two-step drawing process which involves a sapphire tip and a burner. In the first step, a tapered fiber with a diameter of several microns is fabricated by using conventional flame technique. Then the tapered fiber is wrapped on the tip of the sapphire and the sapphire is heated by the burner at the position not far from the tip. The heat is conducted by sapphire and delivered to the tapered fiber wrapped on the tip. The softened tapered fiber is pulled away from the sapphire tip and finally a thin nanowire is drawn. A free standing nanowire with an extremely thin diameter as narrow as 50 nm had been demonstrated. Direct drawing technique enables fabrication of microfibers from a bulk glass [1]. Similar to the previous technique, direct drawing requires a sapphire fiber in the drawing of nanowires. First, the sapphire fiber is heated with a CO_2 laser or flame while the sapphire fiber end is immersed into a bulk glass

through local melting. A small portion of the molten glass coated on the sapphire fiber when it is removed from the bulk glass. A second sapphire fiber is brought in and it touches the melt glass coating on the first sapphire fiber. A thin nanowire is drawn between two sapphire fibers when one of them is pulled away from the other one. This technique allows drawing of nanowires using a small starting volume of material. Unlike the other techniques that requires a glass material in an initial form of fiber, direct drawing technique is suitable for any initial geometry of the glass.

Flame brushing technique appears to be one of the most commonly used fabrication technique for tapered fiber / microfibers and fiber couplers [12, 13]. In this technique, an SMF is clamped by two fiber holders on translation stages. A gas burner with small flame width provides a uniform heat on a segment of the fiber in an oscillatory manner in parallel with the SMF. The diameter of heated glass fiber is reduced when the SMF is stretched by two fiber holders. With the aid of computer and other peripherals, a tapered fiber can be fabricated to a specific length and shape at an extremely high precision. The shape of the tapered fiber happens to be one of the most important criteria in achieving adiabatic tapered fibers [14]. Long nanowires with radii as small as 30nm have been demonstrated using this technique [15]. However, there are setbacks in using gas burner in the fabrication of tapered fiber especially in the case where the gas burner provides direct heating to the fiber. The air-convection from the torch nozzle often disrupts and bends the heated fiber during the process of tapering. In addition, due to the usage of hydrocarbon gas as fuel gas in the burning, some amount of hydroxyl ions may be introduced to the tapered fiber. Hydroxyl ions have the high absorption at 1.38 μm which is very near to one of the communication bands. These issues can be addressed by using modified flame brushing technique [16] in which the gas burner is replaced with an electric microheater. Another advantage of this improved technique is the flexible control of the temperature of the electric microheater. It can be

adjusted to coincide with the melting temperatures of any glass compounds or soft glass such as charcogenide [17, 18] and bismuth [19, 20] so that microfibers can be fabricated from them. Similar to the conventional flame brushing technique, the shape of tapered fiber can be manufactured at high accuracy with the replaced electric microheater. All fabrication techniques that involve heating have enabled production of tapered fibers with incomparably good quality in terms of uniformity and surface roughness. Those are the important criteria for low-loss optical devices. Beside glass, polymers have also been used as a raw material for microfibers [21-23]. Polymer microfibers provide comparable optical properties with glass microfibers with additional advantage in the ease of fabrication because of the lower melting temperature and good flexibility [24]. To provide protection to the microfiber devices, they are embedded in a UV-curable resin that has a refractive index lower than that of silica glass but higher than that of air. Initially, the resin comes in a form of liquid and it is solidified after curing with UV light. The wave guiding property of the microfiber devices is stabilized after it is embedded in the resin. Besides prolonging the lifespan of the microfiber devices, the resin can improve the resonance condition of the microfiber resonators.

2.2 Optical Properties of Tapered Fibers

Tapered fibers offer many interesting optical properties which are found useful in many applications. One of properties is the low insertion loss in the connection with the optical devices fabricated from microfibers. These devices are assembled from adiabatic tapered fibers which are generally known for their low insertion loss. They do not have the problem of fiber-waveguide-fiber coupling that usually introduces very high excess loss to the devices. Adiabatic tapered fibers can be fabricated by ensuring the shape of tapered fiber fulfills the adiabaticity criteria [14] in which the power of fundamental mode in the SMF is conserved as much as possible by preventing the

mode-interaction between fundamental mode with the higher order modes when propagating through the tapered fiber of varying radius. Higher order modes will be suppressed when entering taper waists of small radii and they lose power. Therefore, adiabaticity is crucially important when it comes to fabrication of single-mode microfibers.

Another important property of tapered fiber is the large evanescent field. The variation of mode field diameter (MFD) in the varying tapered fiber diameter was discussed by Love [25]. In a conventional SMF, the fundamental mode field can be well described by Gaussian distribution where a significant large fraction of field power is confined within the core of fiber but a small fraction of modal power is in the cladding near to the core-cladding boundary. The MFD is that at which the power of the field $1/e^2$ of maximum intensity of the mode. MFD has a strong dependency on the diameter and numerical aperture (NA) of the tapered fiber. Their relationship can be well-related through V-number as given by

$$V = \frac{2\pi \cdot \rho \cdot NA}{\lambda} \tag{2.1}$$

where ρ is the core / cladding radius of the tapered fiber.

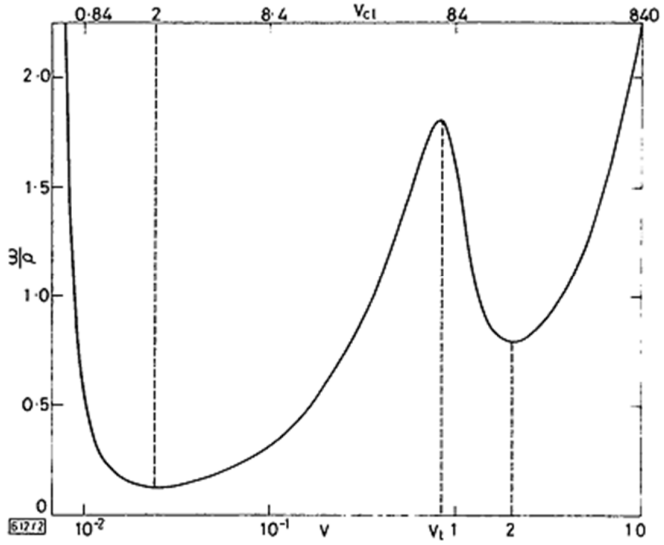

Figure 2.1: Graph of absolute spot size ω/ρ versus V-numbers of core and cladding [25]

Figure 2.1 shows the plot of absolute spot size against the V-number of a tapered fiber. As seen in the figure, the MFD is decreasing with the decreasing core diameter and it reaches its minimum at $V_{\text{core}} \approx 2$. As the radius of the fiber continues to decrease, the diffraction effect begins to dominate and the MFD begins to increase. Until certain point where the effective index of the fundamental mode in the fiber core is equivalent to that of cladding, the confining effect has countered the effect of diffraction and the MFD is decreasing again. Starting from this point, the light in the fiber is guided by air-cladding interface and the effect of the core can be neglected. The MFD reaches the minimum again when $V_{\text{cladding}} \approx 2$. The nonlinear effect is optimum at this point because of the strong confinement of light intensity within this tapered fiber. As the down-tapering continues, the MFD is increasing monotonically with decreasing cladding diameter. The mode field spreads out of the cladding of the fiber and the portion of field guided outside of the fiber is called evanescent field. Typically, stronger evanescent field can be achieved with a tapered fiber of smaller radius and the power in the evanescent field can reach as much as 90% of the total power [26]. Figure 2.2(a) shows the relationship between fractional power inside an air-clad silica micro- / nanofiber (MNF) and its diameter. The confinement of light power within micro- / nanofiber decreases with decreasing diameter which results to strong evanescent field. This effect is wavelength dependent and the longer wavelength has stronger evanescent field. Figure 2.2(b) shows a typical evanescent field of an MNF. The strongest evanescent field strength is at the point near to the MNF and it decays with the increasing distance from the MNF. Evanescent field is an important property of tapered fiber that makes evanescent coupling in microfiber devices possible through near field interaction [11, 27]. In fact, this property is an imperative element in the operating principle of most microfiber devices [23, 28-38].

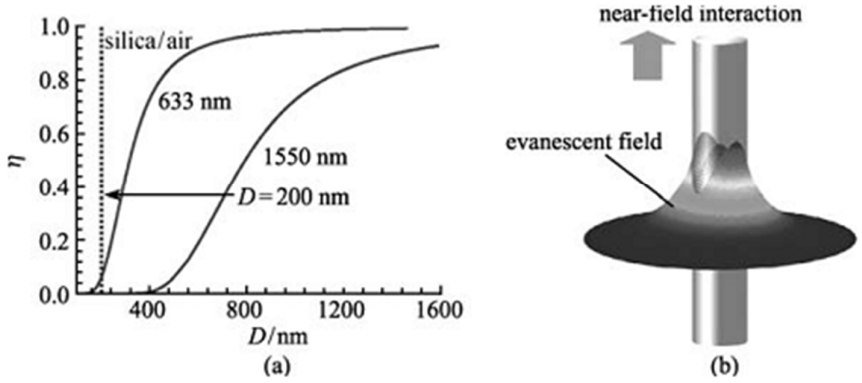

Figure 2.2: (a) Relationship between the fractional power inside an air-clad silica micro-/ nanofiber and its diameter with wavelengths of 633 nm and 1550 nm. (b) Schematic illustration of evanescent field [39].

By virtue of the large air-silica index-contrast (~0.44), microfibers can bear small bending radius with very little bending loss [11]. Restricted by the elastic force, microfibers have their limit in bending radii without breaking themselves. Jiang et. al. have assembled a 35 μm diameter microfiber knot resonator from a 1 μm diameter microfiber and the free spectral range (FSR) is 14.9 nm [39]. Depending on the microfiber diameter, a 360-nm-diameter silica nanofiber with a bending radius as small as 3 μm has been demonstrated as shown in Figure 2.3. This property enables manufacture of miniaturized optical components using microfibers with comparable dimension and functionalities with the conventional devices based on lithographic waveguides.

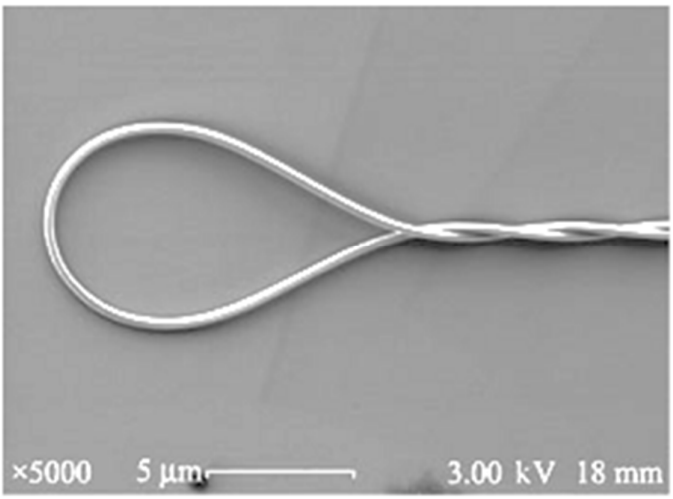

Figure 2.3: A 360 nm diameter silica nanofiber with a minimum bending radius of about 3 µm [39].

Chromatic dispersion is one of the important characteristics in optical waveguides that is associated with pulse width broadening and decreasing pulse peak power. It is always imperative to take dispersion characteristics into consideration when in the design of optical waveguides and photonic components. As the pulses propagate along the fiber in the region far from the zero dispersion wavelength, they tend to disperse and error may be introduced to optical signal that carries data and information. As a result of the dispersion, the peak power of the pulse decreases with increasing propagating distance. In connection with optical nonlinearity, it is essentially important to ensure the operating wavelength is located within the region of low dispersion and low dispersion slope as the nonlinear effect is optimal at zero-dispersion wavelength. In year 2000, Birks et. al. have successfully demonstrated supercontinuum generation in silica tapered fibers [40]. To achieve optimum supercontinuum effect, the taper waist diameter is deliberately tailored to have its zero-dispersion wavelength coincides with source wavelength. Since then, supercontinuum generation using tapered fibers of different glass materials such as charcogenide and bismuth silicate have been demonstrated. The understanding of the dispersion characteristics of these tapered fibers

is essential in these studies [19, 41]. Besides supercontinuum, four-wave mixing effect (FWM) is another nonlinear effect that is critical to the dispersion characteristic of the transmission medium. FWM is inhibited by the walk-off effect in a dispersive region but the effect can be alleviated by implementing the FWM in low dispersion region [42]. Intense investigations and simulation results on the dispersion based on Maxwell's equations can be found in the literatures [26, 43, 44].

2.3 Applications and Functionalities

Microfibers have exhibited great potential for a variety of applications. The dispersion properties of the microfibers have enabled them to be employed for dispersion compensation in mode-locking system to achieve zero dispersion in the cavity and reduce the pulse width [45]. The radii of microfibers can be tailored in a way to achieved large dispersion and large dispersion slope. Short length of microfibers is sufficient to provide dispersion compensation for any target system. The zero-dispersion wavelength can also be engineered to coincide with the desired operating wavelength to optimize the functionalities of the devices in a variety of fiber optic systems [43, 46, 47]. Single-mode operation is always desired in many fiber-optic systems because of the many advantages including large capacity in long distance transmission, low attenuation loss, simplicity in operation and etc. In favour of that, microfibers can be employed to filter the higher order modes (HOMs) in the fibers. Donlagic [48] has developed a HOMs filter based on tapered long highly uniform tapered fiber and the suppression on the HOMs are up to 39 dB while the fundamental mode only suffers an insertion loss less than 0.15 dB. MFD mismatch occurs in the coupling or splicing between two waveguides of different spot sizes particularly in the fiber-planar waveguide coupling and the excess loss induced can be unbearably high. This problem can be alleviated through spot-size conversion using tapered fiber. Adiabatic coupling is achieved by

varying the MFD of a fiber to match with the MFD of the other fiber or waveguide through tapering [20, 49, 50]. The strong evanescent fields of microfibers are useful for near-field interaction between microfibers and other photonics components or any chemical substances. This property is employed for many applications where microfibers are used to couple the light in and out of microresonators such as whispering gallery mode [17, 51], microdisk resonator [52], microtoroid [53], optical tweezers [54, 55] and etc. Some of these high-Q resonators are used as industrial sensors for biomedicine [56, 57], small molecules detection [58] and gas temperature [59]. Figure 2.4 shows an example of a ~300 µm diameter silica microsphere.

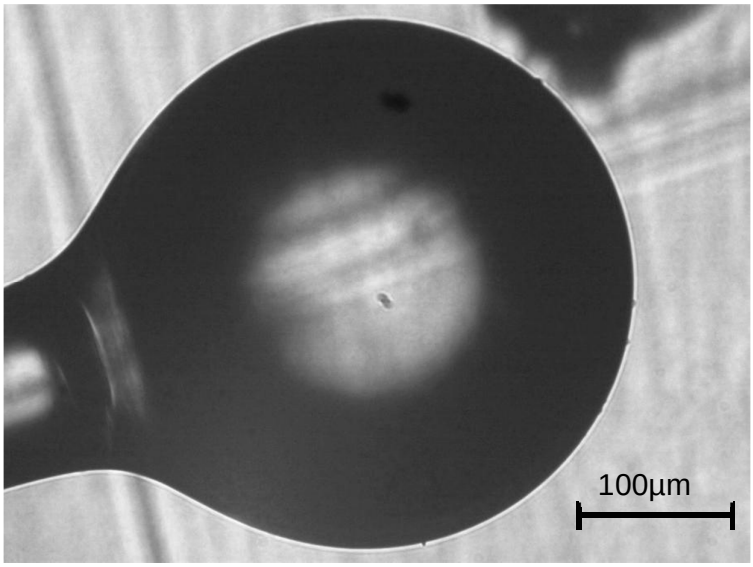

Figure 2.4: Optical microscope image of a ~300 µm-diameter silica microsphere.

References

[1] L. Tong, L. Hu, J. Zhang, J. Qiu, Q. Yang, J. Lou, Y. Shen, J. He, and Z. Ye, "Photonic nanowires directly drawn from bulk glasses," *Opt. Express,* vol. 14, no. 1, pp. 82-87, 2006.

[2] R. Stockle, C. Fokas, V. Deckert, R. Zenobi, B. Sick, B. Hecht, and U. P. Wild, "High-quality near-field optical probes by tube etching," *Applied Physics Letters,* vol. 75, no. 2, pp. 160-162, 1999.

[3] D. R. C. T. Turner, Morris County, NJ), "Etch procedure for optical fibers," United States Patent, 1984.

[4] P. K. Wong, Wang, T., Ho, C.,, "Optical fiber tip fabricated by surface tension controlled etching," in *Proceedings of Solid. State Sensor* Actuator and Microsystems Workshop Transducers Research Foundation, Cleveland, Ohio, 2002, pp. 94-97.

[5] H. S. Haddock, P. M. Shankar, and R. Mutharasan, "Fabrication of biconical tapered optical fibers using hydrofluoric acid," *Materials Science and Engineering B,* vol. 97, no. 1, pp. 87-93, 2003.

[6] J. M. Corres, I. R. Matias, J. Bravo, and F. J. Arregui, "Tapered optical fiber biosensor for the detection of anti-gliadin antibodies," *Sensors and Actuators B: Chemical,* vol. 135, no. 1, pp. 166-171, 2008.

[7] M. Sumetsky, Y. Dulashko, and A. Hale, "Fabrication and study of bent and coiled free silica nanowires: Self-coupling microloop optical interferometer," *Opt. Express,* vol. 12, no. 15, pp. 3521-3531, 2004.

[8] G. Kakarantzas, T. E. Dimmick, T. A. Birks, R. Le Roux, and P. S. J. Russell, "Miniature all-fiber devices based on CO2 laser microstructuring of tapered fibers," *Opt. Lett.,* vol. 26, no. 15, pp. 1137-1139, 2001.

[9] P. Pal and W. H. Knox, "Fabrication and Characterization of Fused Microfiber Resonators," *Photonics Technology Letters, IEEE,* vol. 21, no. 12, pp. 766-768, 2009.

[10] P. Pal and W. H. Knox, "Low loss fusion splicing of micron scale silica fibers," *Opt. Express,* vol. 16, no. 15, pp. 11568-11573, 2008.

[11] L. Tong, R. R. Gattass, J. B. Ashcom, S. He, J. Lou, M. Shen, I. Maxwell, and E. Mazur, "Subwavelength-diameter silica wires for low-loss optical wave guiding," *Nature,* vol. 426, no. 6968, pp. 816-819, 2003.

[12] F. Bilodeau, K. O. Hill, S. Faucher, and D. C. Johnson, "Low-loss highly overcoupled fused couplers: fabrication and sensitivity to external pressure," *Lightwave Technology, Journal of,* vol. 6, no. 10, pp. 1476-1482, 1988.

[13] B. Pal, "Fabrication and Modeling of Fused Biconical Tapered Fiber Couplers," *Fiber and Integrated Optics,* vol. 22, no. 2, pp. 97-117, 2003/01/01 2003.

[14] T. A. Birks and Y. W. Li, "The shape of fiber tapers," *Lightwave Technology, Journal of,* vol. 10, no. 4, pp. 432-438, 1992.

[15] G. Brambilla, F. Xu, and X. Feng, "Fabrication of optical fibre nanowires and their optical and mechanical characterisation," *Electronics Letters,* vol. 42, no. 9, pp. 517-519, 2006.

[16] G. Brambilla, Y. Jung, and F. Renna, "Optical fiber microwires and nanowires manufactured by modified flame brushing technique: properties and applications," *Frontiers of Optoelectronics in China,* vol. 3, no. 1, pp. 61-66, 2010.

[17] C. Grillet, S. N. Bian, E. C. Magi, and B. J. Eggleton, "Fiber taper coupling to chalcogenide microsphere modes," *Applied Physics Letters,* vol. 92, no. 17, pp. 171109-3, 2008.

[18] F. Libin, D. P. Mark, C. M. Eric, G. T. e. Vahid, and J. E. Benjamin, "Enhanced Nonlinearity Tapered Chalcogenide Fiber for All-Optical Wavelength Conversion of 40 Gb/s Signals," 2008, p. OThJ2.

[19] G. Brambilla, F. Koizumi, V. Finazzi, and D. J. Richardson, "Supercontinuum generation in tapered bismuth silicate fibres," *Electronics Letters,* vol. 41, no. 14, pp. 795-797, 2005.

[20] T. Hasegawa, T. Nagashima, and N. Sugimoto, "A simple tapered bismuth-based nonlinear optical fiber for low-loss coupling to single-mode silica fibers," in *Optical Fiber Communication Conference, 2006 and the 2006 National Fiber Optic Engineers Conference. OFC 2006*, 2006, p. 3 pp.

[21] F. Gu, L. Zhang, X. Yin, and L. Tong, "Polymer Single-Nanowire Optical Sensors," *Nano Letters,* vol. 8, no. 9, pp. 2757-2761, 2008.

[22] C. Pulido and Ó. Esteban, "Improved fluorescence signal with tapered polymer optical fibers under side-illumination," *Sensors and Actuators B: Chemical,* vol. 146, no. 1, pp. 190-194, 2010.

[23] Y. Wu, Y.-J. Rao, Y.-h. Chen, and Y. Gong, "Miniature fiber-optic temperature sensors based on silica/polymer microfiber knot resonators," *Opt. Express,* vol. 17, no. 20, pp. 18142-18147, 2009.

[24] Q. Yang, X. Jiang, F. Gu, Z. Ma, J. Zhang, and L. Tong, "Polymer micro or nanofibers for optical device applications," *Journal of Applied Polymer Science,* vol. 110, no. 2, pp. 1080-1084, 2008.

[25] J. D. Love, "Spot size, adiabaticity and diffraction in tapered fibres," *Electronics Letters,* vol. 23, no. 19, pp. 993-994, 1987.

[26] L. Tong, J. Lou, and E. Mazur, "Single-mode guiding properties of subwavelength-diameter silica and silicon wire waveguides," *Opt. Express,* vol. 12, no. 6, pp. 1025-1035, 2004.

[27] Y. Jung, G. Brambilla, and D. J. Richardson, "Optical microfiber coupler for broadband single-mode operation," *Opt. Express,* vol. 17, no. 7, pp. 5273-5278, 2009.

[28] Y.-H. W. Chen, Yu; Rao, Yun-Jiang; Deng, Qiang; Gong, Yuan, "Hybrid Mach-Zehnder interferometer and knot resonator based on silica microfibers," *Optics Communications,* vol. 283, no. 14, p. 4, 2010.

[29] X. Jiang, L. Tong, G. Vienne, X. Guo, A. Tsao, Q. Yang, and D. Yang, "Demonstration of optical microfiber knot resonators," *Applied Physics Letters,* vol. 88, no. 22, pp. 223501-223501-3, 2006.

[30] Y. Jung, G. S. Murugan, G. Brambilla, and D. J. Richardson, "Embedded Optical Microfiber Coil Resonator With Enhanced High-Q," *Photonics Technology Letters, IEEE,* vol. 22, no. 22, pp. 1638-1640, 2010.

[31] Y. Li and L. Tong, "Mach-Zehnder interferometers assembled with optical microfibers or nanofibers," *Opt. Lett.,* vol. 33, no. 4, pp. 303-305, 2008.

[32] K. S. Lim, S. W. Harun, S. S. A. Damanhuri, A. A. Jasim, C. K. Tio, and H. Ahmad, "Current sensor based on microfiber knot resonator," *Sensors and Actuators A: Physical,* vol. 167, no. 1, pp. 377–381, 2011.

[33] M. Sumetsky, Y. Dulashko, J. M. Fini, and A. Hale, "Optical microfiber loop resonator," *Applied Physics Letters,* vol. 86, no. 16, pp. 161108-161108-3, 2005.

[34] M. Sumetsky, Y. Dulashko, J. M. Fini, A. Hale, and D. J. DiGiovanni, "The microfiber loop resonator: theory, experiment, and application," *Lightwave Technology, Journal of,* vol. 24, no. 1, pp. 242-250, 2006.

[35] M. Sumetsky, Y. Dulashko, and S. Ghalmi, "Fabrication of miniature optical fiber and microfiber coils," *Optics and Lasers in Engineering,* vol. 48, no. 3, pp. 272-275, 2010.

[36] G. Vienne, A. Coillet, P. Grelu, M. El Amraoui, J.-C. Jules, F. Smektala, and L. Tong, "Demonstration of a reef knot microfiber resonator," *Opt. Express,* vol. 17, no. 8, pp. 6224-6229, 2009.

[37] F. Xu, P. Horak, and G. Brambilla, "Optical microfiber coil resonator refractometric sensor," *Opt. Express,* vol. 15, no. 12, pp. 7888-7893, 2007.

[38] X. Zeng, Y. Wu, C. Hou, J. Bai, and G. Yang, "A temperature sensor based on optical microfiber knot resonator," *Optics Communications,* vol. 282, no. 18, pp. 3817-3819, 2009.

[39] L. Tong, "Brief introduction to optical microfibers and nanofibers," *FRONTIERS OF OPTOELECTRONICS,* vol. 3, no. 1, pp. 54-60, 2010.

[40] T. A. Birks, W. J. Wadsworth, and P. S. J. Russell, "Supercontinuum generation in tapered fibers," *Opt. Lett.,* vol. 25, no. 19, pp. 1415-1417, 2000.

[41] Y. Dong-Il, C. M. Eric, R. L. Michael, F. Libin, and J. E. Benjamin, "Low-Threshold Supercontinuum Generation in Dispersion Engineered Highly Nonlinear Chalcogenide Fiber Nanowires," 2008, p. OTuB5.

[42] K. S. Abedin, J. T. Gopinath, E. P. Ippen, C. E. Kerbage, R. S. Windeler, and B. J. Eggleton, "Highly nondegenerate femtosecond four-wave mixing in tapered microstructure fiber," *Applied Physics Letters,* vol. 81, no. 8, pp. 1384-1386, 2002.

[43] R. Zhang, J. Teipel, X. Zhang, D. Nau, and H. Giessen, "Group velocity dispersion of tapered fibers immersed in different liquids," *Opt. Express,* vol. 12, no. 8, pp. 1700-1707, 2004.

[44] R. Zhang, X. Zhang, D. Meiser, and H. Giessen, "Mode and group velocity dispersion evolution in the tapered region of a single-mode tapered fiber," *Opt. Express,* vol. 12, no. 24, pp. 5840-5849, 2004.

[45] R. Herda, M. Rusu, S. Kivistö, and O. G. Okhotnikov, "Mode-locked ytterbium fiber laser with dispersion compensation by a fiber taper," in *Ultrafast Phenomena XV*. vol. 88, P. Corkum, *et al.*, Eds., ed: Springer Berlin Heidelberg, 2007, pp. 83-85.

[46] J. Mora, A. Diez, M. V. Andres, P. Y. Fonjallaz, and M. Popov, "Tunable dispersion compensator based on a fiber Bragg grating written in a tapered fiber," *Photonics Technology Letters, IEEE*, vol. 16, no. 12, pp. 2631-2633, 2004.

[47] J. Zhang, P. Shum, X. P. Cheng, N. Q. Ngo, and S. Y. Li, "Analysis of linearly tapered fiber Bragg grating for dispersion slope compensation," *Photonics Technology Letters, IEEE*, vol. 15, no. 10, pp. 1389-1391, 2003.

[48] D. Donlagic, "In-line higher order mode filters based on long highly uniform fiber tapers," *Lightwave Technology, Journal of*, vol. 24, no. 9, pp. 3532-3539, 2006.

[49] J. K. Chandalia, B. J. Eggleton, R. S. Windeler, S. G. Kosinski, X. Liu, and C. Xu, "Adiabatic coupling in tapered air-silica microstructured optical fiber," in *Optical Fiber Communication Conference and Exhibit, 2001. OFC 2001*, 2001, pp. TuC2-1-TuC2-3 vol.2.

[50] G. E. Town and J. T. Lizier, "Tapered holey fibers for spot size and numerical aperture conversion," in *Lasers and Electro-Optics, 2001. CLEO '01. Technical Digest. Summaries of papers presented at the Conference on*, 2001, p. 261.

[51] M. Hossein-Zadeh and K. J. Vahala, "Fiber-taper coupling to Whispering-Gallery modes of fluidic resonators embedded in a liquid medium," *Opt. Express*, vol. 14, no. 22, pp. 10800-10810, 2006.

[52] T. Zhaobing, C. Chen, and D. V. Plant, "Single- and Dual-Wavelength Fiber Ring Laser Using Fiber Microdisk Resonator," *Photonics Technology Letters, IEEE,* vol. 22, no. 22, pp. 1644-1646, 2010.

[53] H. K. Hunt, C. Soteropulos, and A. M. Armani, "Bioconjugation Strategies for Microtoroidal Optical Resonators," *Sensors,* vol. 10, no. 10, pp. 9317-9336, 2010.

[54] Z. Liu, C. Guo, J. Yang, and L. Yuan, "Tapered fiber optical tweezers for microscopic particle trapping: fabrication and application," *Opt. Express,* vol. 14, no. 25, pp. 12510-12516, 2006.

[55] F. Xu, G. Brambilla, and D. J. Richardson, "Adiabatic SNOM tips for optical tweezers," ed, 2006.

[56] S. Soria, S. Berneschi, M. Brenci, F. Cosi, G. Nunzi Conti, S. Pelli, and G. C. Righini, "Optical Microspherical Resonators for Biomedical Sensing," *Sensors,* vol. 11, no. 1, pp. 785-805, 2011.

[57] J. Yang and L. J. Guo, "Optical sensors based on active microcavities," *Selected Topics in Quantum Electronics, IEEE Journal of,* vol. 12, no. 1, pp. 143-147, 2006.

[58] I. M. White, N. M. Hanumegowda, and X. Fan, "Subfemtomole detection of small molecules with microsphere sensors," *Opt. Lett.,* vol. 30, no. 23, pp. 3189-3191, 2005.

[59] M. Gregor, C. Pyrlik, R. Henze, A. Wicht, A. Peters, and O. Benson, "An alignment-free fiber-coupled microsphere resonator for gas sensing applications," *Applied Physics Letters,* vol. 96, no. 23, pp. 231102-3, 2010.

Chapter 3

FABRICATION OF TAPERED FIBERS / MICROFIBERS

3.1 Introduction

Fabrication of microfibers is an important step in this research prior to the fabrication of optical microfiber devices such as microfiber loop resonator, microfiber knot resonator, microfiber coil resonator, Mach-Zehnder interferometer and microfiber loop mirror. The properties of the microfiber devices are highly dependent on the quality of the microfibers used. To produce high quality microfiber devices, the microfibers used should have the following properties: high adiabaticity, uniform microfiber diameter, low surface roughness, and suitable microfiber diameter with large evanescent field. The microfiber diameter has a direct influence in the evanescent field and coupling coefficient of the microfiber coupling region in most microfiber devices. Basically, microfibers with thinner diameter have stronger evanescent field and thus yield higher coupling coefficient between two or more microfibers when they are put in a close contact with each other. Therefore, most microfiber devices are assembled from microfibers with small diameter (0.8~3 μm). Besides, thin microfiber can be easily bent or coiled into smaller bending radius and thus smaller microfiber device can be produced. However, the difficulty in handling these microfibers increases with smaller diameter as thinner microfibers are very fragile and lossy. Microfiber have been fabricated based on various techniques: laser ablation [1], electron beam lithography [2], vapor–liquid–solid techniques [3], and fiber pulling [4, 5] or direct draw from bulk glasses [6]. Among those methods, the flame heating technique has proven to be the best method as it can produce microfiber with the best physical properties [4, 7]. In this

chapter, two microfiber fabrication techniques that had been practiced in our work will be discussed, namely chemical etching technique and flame brushing technique [8]. However, flame brushing technique will be the major technique used in the fabrication of tapered fiber. The fiber tapering rig operates based on flame brushing technique will be introduced. Fabrications of several different tapered fiber shapes are demonstrated and discussed. To overcome the fast aging problem of tapered fiber, two packaging techniques are suggested and demonstrated. One of them involves embedding the tapered fiber/ microfiber in a low-index material while the other one is encapsulating the long tapered fiber in an Acrylic case. The performances of the unpackaged and packaged tapered fibers are compared. Lastly in this chapter, dispersion measurement on a tapered fiber is performed based on Michelson Interferometry configuration. The measured dispersion is very close to the calculated dispersion.

3.2 Fabrication of Fiber Taper by Using Chemical Etching Technique

Chemical etching is a low cost and simple technique for the fabrication of fiber taper. Its ability of mass production in a single step makes this technique very attractive and widely used. In this technique, optical fiber is dipped in a hydrofluoride acid (HF) solution and the etching starts from the contact surface between the silica glass and HF. The removal of silica glass is caused by chemical reaction between silicon dioxide and HF.

$$SiO_2 + 6\ HF \rightarrow H_2SiF_6 + 2\ H_2O \qquad (3.1)$$

To form a sharp fiber tip, Turner [9, 10] suggests adding a layer of organic solvent to the HF solution where organic solvent is on top of the HF (Refer Figure 3.1). The meniscus between organic solvent and HF is formed around the fiber. The height of the meniscus decreases as fiber diameter decreases and HF stops attacking the part where

the fiber is in the organic solvent layer [9]. This mechanism helps the shaping of the fiber into a sharp tip with small tip angle of between 7° and 22°.

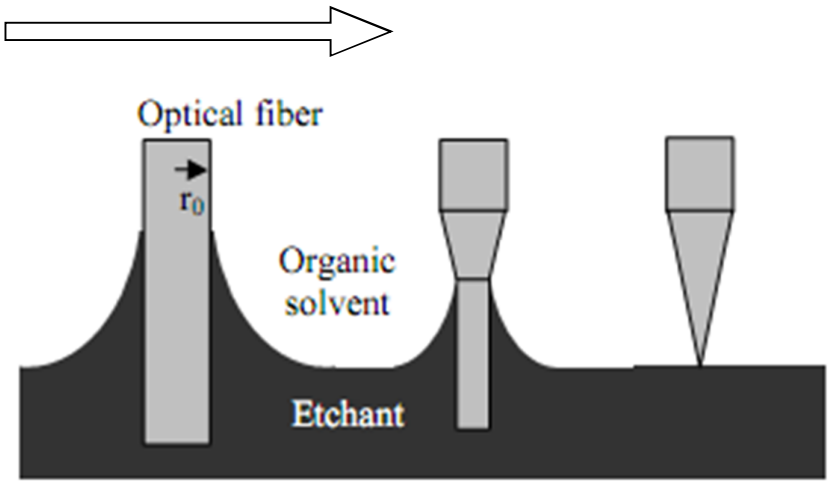

Figure 3.1: Schematic illustration of the fiber tip formation from a flat end (left) to sharp tip (right) [11].

In the experiment, an optical fiber is dipped into a HF solution of ~ 48% concentration (990 kg/m^3) which is overlaid with a layer of silicone oil (organic solvent) that had a smaller density (760 kg/m^3). At room temperature of 25℃, the etching rate is ~ 3.62 μm/min. Figures 3.2(a)-(c) show the formation of fiber taper at different time. After 15 minutes of etching, the optical fiber lost 54μm in diameter and became 72 μm as shown in Figure 3.2(a). The thinning process continued and at t = 30 minutes, the taper waist diameter had decreased down to 15μm as illustrated in Figure 3.2(b). However, the etching rate became a bit lower when it came to the core of the optical fiber. The Ge-dopants in the fiber core is held responsible for slowing down the etching process and eventually the fiber became a sharp taper 10 minutes later as shown in Figure 3.2(c).

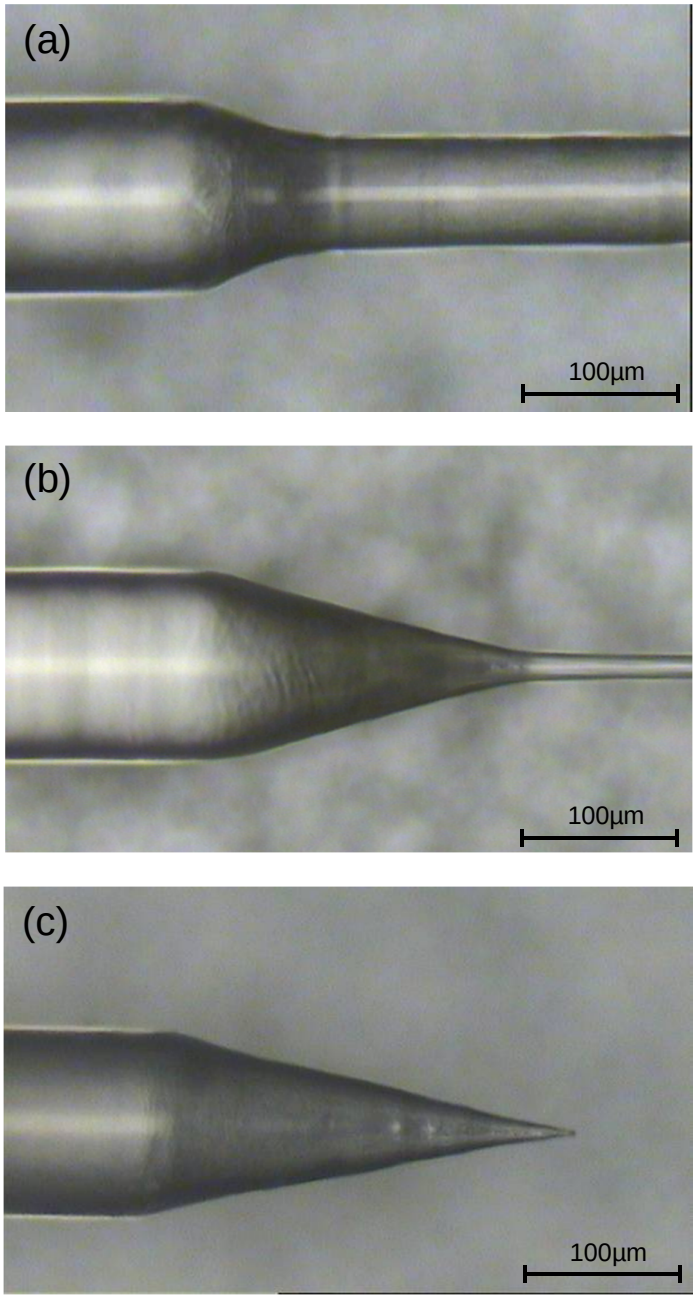

Figure 3.2: Fiber taper formation at (a) 15 minutes, (b) 30 minutes and (c) 40 minutes.

Some environmental perturbations may influence the etched taper geometry such as the vibration, temperature change and impurity in etchant solution. Asymmetry taper shape, large cone aperture and high surface roughness are the major setbacks that jeopardize the throughput power of the fiber taper. However, these problems can be overcome by using tube etching technique [12]. In this technique, the polymer coating of the optical fiber is not removed during the etching in the HF solution. The polymer

coating provides a cylindrical cavity and to enhance the tolerance of the etching process to the environmental perturbations. Figure 3.3 shows an example of the conical tapered fiber fabricated by tube etching technique. In comparison with the etched taper tip shown in Figure 3.2(c), tube etching outperforms the conventional technique in terms of achieving fiber tapers with reduced surface roughness, better symmetry in shape and sharper cone tips. However, chemical etching technique is not favoured for the fabrication of biconical tapered fibers which are highly desired for the manufacture of microfiber devices. Besides, the control on the shape, length and minimum taper waist diameter are limited with this technique. Flame brushing technique does not have the limitations of chemical technique and this makes it a better alternative for the fabrication of tapered fiber.

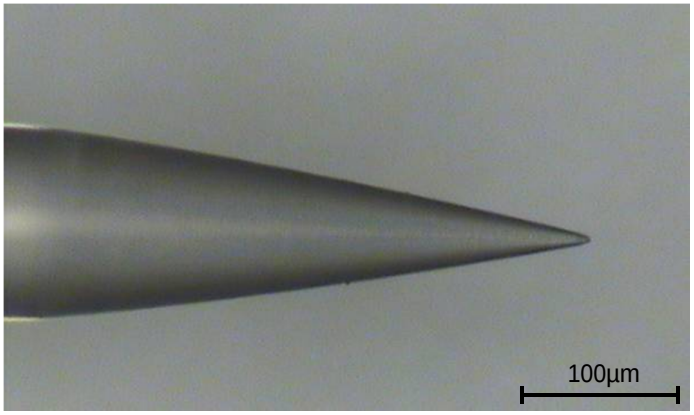

Figure 3.3: Conical tapered fiber fabricated by Tube Etching technique.

3.3 Fabrication of Microfiber by Using Flame Brushing Technique

Flame brushing technique [8, 13] is commonly used for the fabrication of fiber couplers and tapered fibers. It is also chosen in this research due to its high flexibility in controlling flame movement, fiber stretching length and speed. The dimension of the tapered fiber or microfiber can be fabricated with good accuracy and reproducibility. Most importantly, this technique enables fabrication of biconical tapered fibers which both ends of the tapered fiber are connected to single mode fiber (SMF). These

biconical tapered fibers are useful for the ensuing manufacture of microfiber based devices with low insertion loss [8, 14].

3.3.1 Fiber Tapering Rig

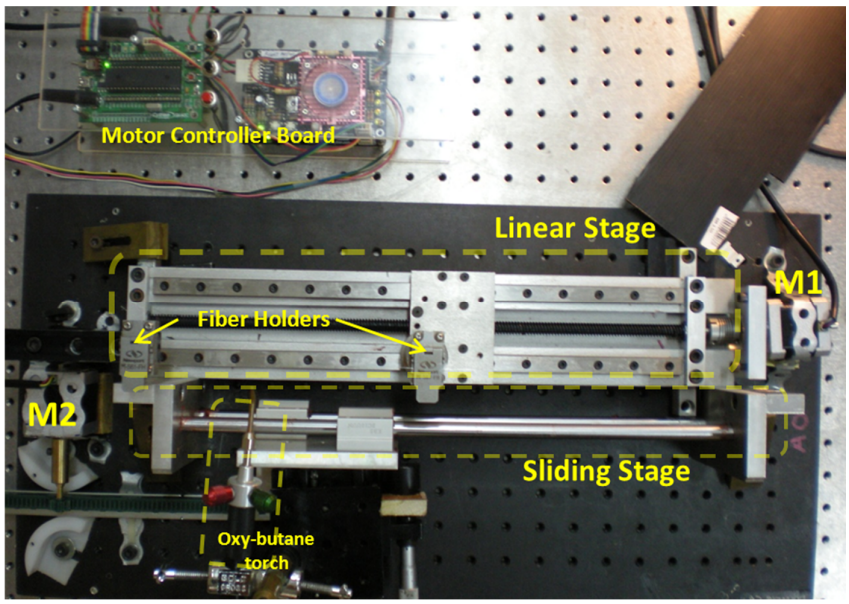

Figure 3.4: Picture of the fiber tapering rig assembled in the laboratory. M1 and M2 are the stepper motors of the linear stage and sliding stage respectively.

Figure 3.4 shows the picture of the fiber tapering rig assembled in the laboratory. It mainly comprises of two fiber holders on a linear translation stage, a sliding stage, an oxy-butane burner which is fixed on the sliding stage, two stepper motors and the motor controller board.

Oxygen and butane gas for the oxy-butane torch are supplied from separate gas cylinders. The mixing of both gases takes place in the torch chamber and the mixture is supplied to a ~1mm sized pin-point flame through a single orifice at the torch tip. Figure 3.5(a)-(c) show the torch flames of different oxygen supply pressure. In the practice of this research group, both oxygen and butane gas pressures are regulated at ~5 psi each as shown in Figure 3.5(b). The convective air flow from the flame is kept at an acceptably low level and the flame temperature is high enough to heat and soften the silica fiber. However, the flame temperature can be further increased by supplying

higher pressure of oxygen to the torch (Refer Figure 3.5(c)) but the flame may go out easily due to fast depletion of fuel gas and the fast convective air flow could result in bending the heated SMF and inducing high insertion loss in the tapered fiber.

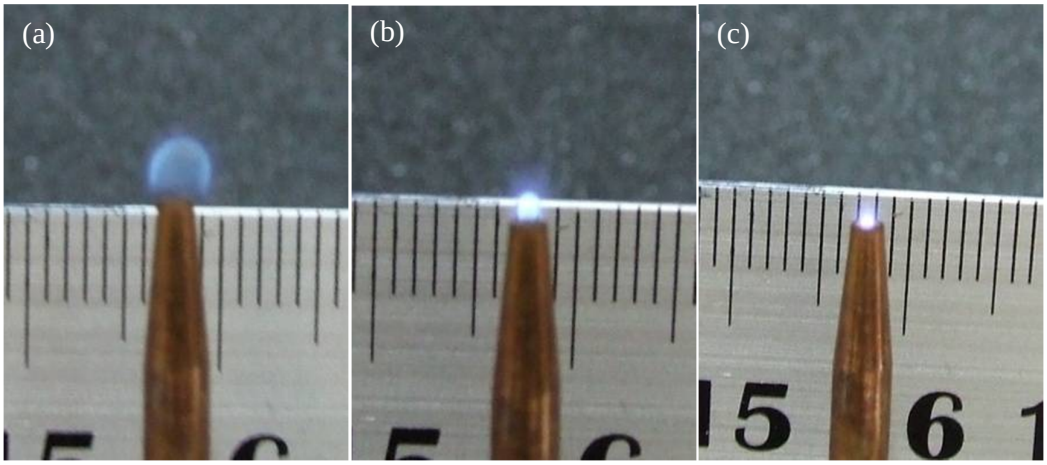

Figure 3.5: Torch flames at different oxygen supply pressure (a) none (b) equivalent pressure with fuel gas pressure (c) high oxygen

In controlling the linear stage and sliding stage travelling speed and position, two high precision stepper motors (LINIX Stepping Motor, Product Code: 42BYGHD-444) with a resolution of 1.8°/step are deployed. Translating the rotation resolution to the linear stage, the linear stage travels at a resolution of 2.5 µm/step and it can reach a maximum speed of 59.6 mm/s. Since, linear stage is responsible for stretching the heated SMF. To fabricate smooth and low loss tapered fibers, the linear stage is often travelling at a very low velocity (0.8 - 1.8 mm/s). In flame brushing a tapered fiber, the oxy-butane torch is required to travel at higher speed than the linear stage to provide a uniform heat to a long tapered fiber. In order to achieve that, the torch is mounted on a custom-made sliding stage that can travel at a very high speed in a linear direction. The sliding stage mainly consists of several pieces of aluminum blocks, two linear bearings and two long steel shafts (Refer Figures 3.6(a) and 3.6 (b)). Different from the movement of linear stage that is based on a gear shaft and leadscrew (Figures 3.6(c) and

3.6(d)), the sliding stage can be moved smoothly and freely in a linear direction with hand like a sliding window.

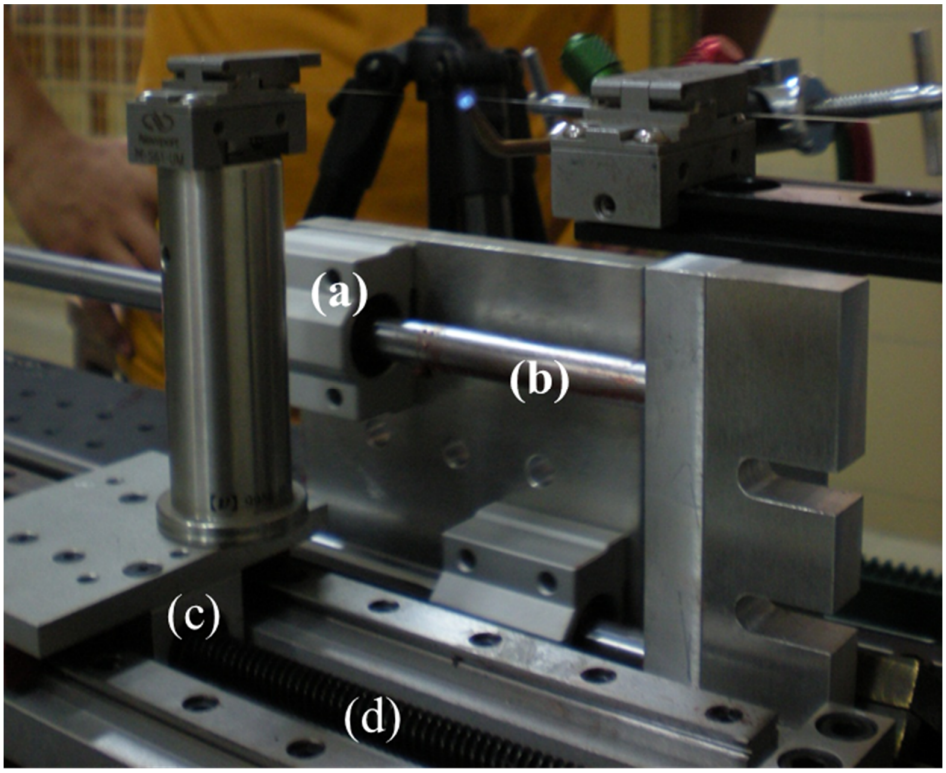

Figure 3.6: The movement of sliding stage is guided by (a) the linear bearings and (b) steel shafts while linear stage is guided by (c) leadscrew and (d) the gear shaft.

Without restriction of gearshaft and leadscrew, the torch that is mounted on the sliding stage can travel at the maximum speed of ~90 mm/s. However the sliding stage moving back and forth at this speed can generate a oscillatory vibration and it may bring damage to the tapered fiber and rig structure. In the practice, the sliding stage is programmed to travel at the moderate speed from 10 – 40 mm/s with a resolution of 317.5 μm/step.

3.3.2 Motor Control

The motor control system of the rig plays the most important part in controlling the stages position, speed and moving direction. The quality of the tapered fiber lies on the routine of the torch movement and linear stage pulling length and speed. With the incorporation of microcontroller in the system, the tapering routine can be written into a code and programmed into the microcontroller. With that, any microfibers with specific diameter and length can be fabricated accurately and reproduced based on the same tapering routine. Figure 3.7 shows the system diagram of the motor control system of the rig. The microcontroller sits at the top of the motor control system hierarchy, coordinating and controlling two different stepper motors. Each stepper motor is equipped with a motor driver (Refer Figure 3.8) and both combinations of motor driver and stepper motor are assigned to the linear stage and sliding stage respectively.

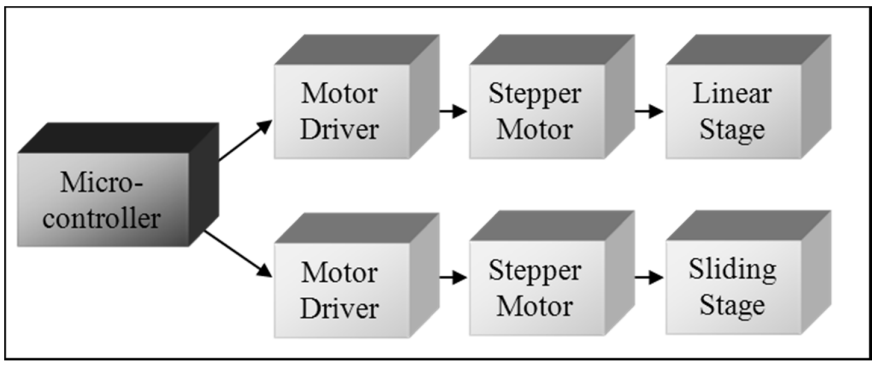

Figure 3.7: System Diagram of the Motor Control in the fiber tapering rig

Microchip PIC18F4520 is used as microcontroller in the system. The tapering routine is written in C language by using MPLAB IDE vs8.53. The code is then converted into a format that can be programmed into the microcontroller using PICkit 2 Development Programmer.

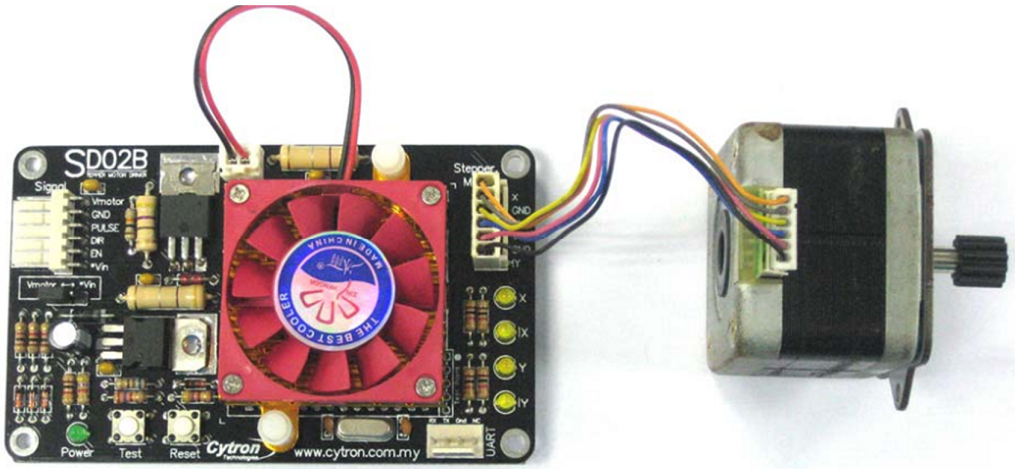

Figure 3.8: Motor Driver and Unipolar Stepper Motor

3.3.3 Fabrication of Tapered Fiber

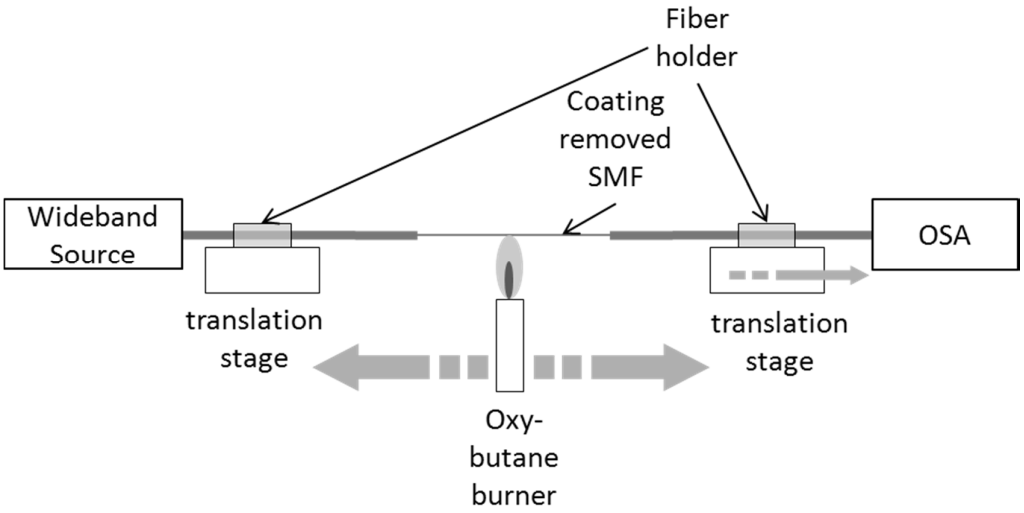

Figure 3.9: Schematic illustration of flame brushing technique

Figure 3.9 shows the schematic diagram of the tapered fiber fabrication based on flame brushing technique. First, coating length of several cm is removed from the SMF prior to the fabrication of tapered fiber. Then the SMF is placed horizontally on the translation stage and held by two fiber holders. During the tapering, the torch moves and heats along the uncoated segment of fiber while the fiber is being stretched. The moving torch provides a uniform heat to the fiber so that the tapered fiber can be produced with good uniformity along the heat region. To monitor the transmission spectrum of the microfiber during the fabrication, amplified spontaneous emission (ASE)

source from an Erbium-doped fiber amplifier (EDFA) is injected into one end of the SMF while the other end is connected to an optical spectrum analyser (OSA). Figure 3.10(a) show diameter variation of the biconical tapered fiber fabricated using the fiber tapering rig and Figure 3.10(b) shows the optical microscope image of waist of the tapered fiber, 1.7 µm in diameter. With proper tapering parameters, the taper waist diameter can be narrowed down to ~400 nm as shown in Figure 3.10(c).

(a)

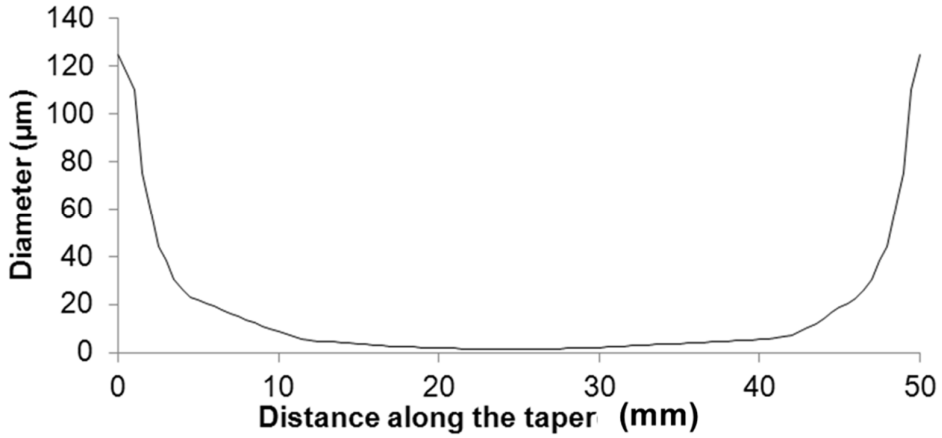

(b)

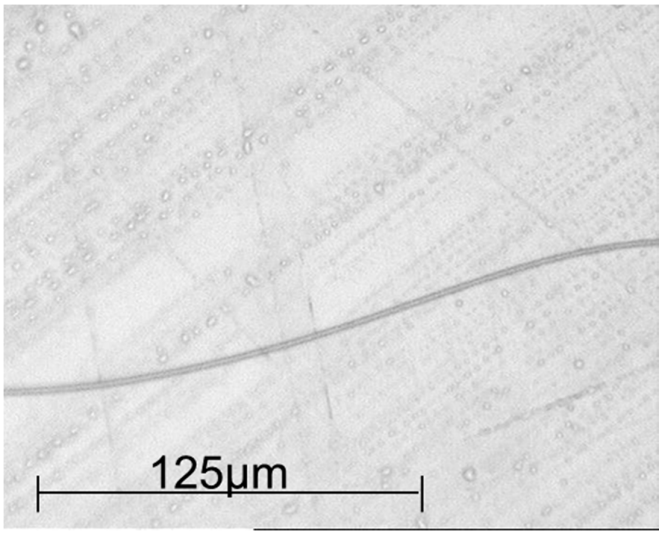

c)

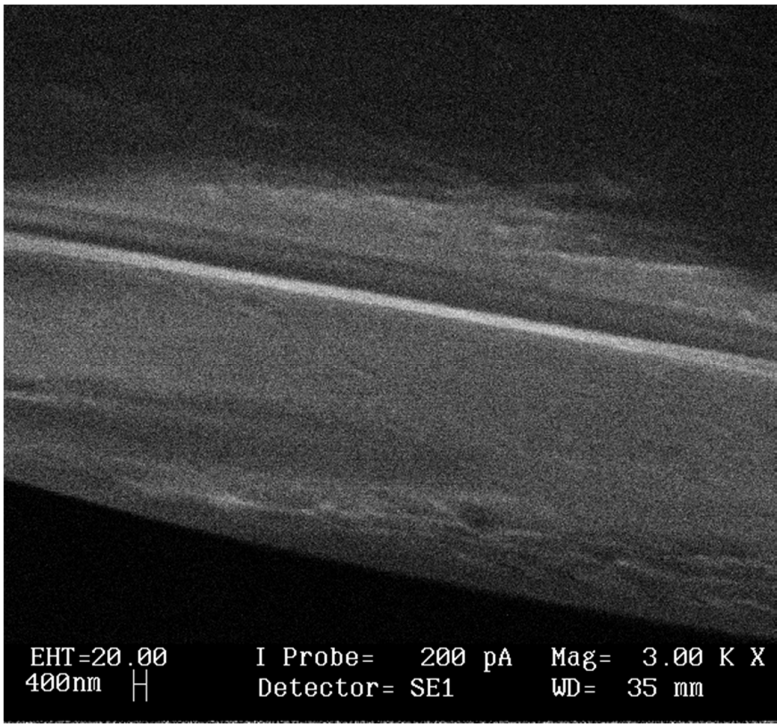

Figure 3.10: (a)The diameter variation of a biconical tapered fiber fabricated in the laboratory (b) Optical microscope image of taper waist, 1.7 μm in diameter (c) SEM image of a 400nm waist diameter tapered fiber

Adiabaticity is one of the important criteria in fabricating good quality tapered fibers. It is commonly known there is a loss of power when the fundamental mode couples to the higher order modes. Some fraction of power from higher order modes that survives propagating through the tapered fiber may recombine and interfere with fundamental mode. This phenomenon can be seen as interference between fundamental mode HE_{11} and its closest higher order mode HE_{12}. This results to a transmission spectrum with irregular fringes as shown by the dotted graph in Figure 3.11 and the insertion loss of the tapered fiber is ~0.6 dB [15, 16]. This tapered fiber is not suitable to be used in the ensuing fabrication of microfiber devices. The solid curve in the same figure shows the transmission of a low loss tapered fiber with approximately more than 4mm transition length and the insertion loss lower than 0.3 dB. Some analysis suggests that the coupling from fundamental mode to higher order modes can be minimized by optimizing shape of the tapers. In most practice, adiabaticity can be easily achieved by

using sufficiently slow diameter reduction rates when drawing tapered fibers or in other words manufacture tapered fibers with sufficiently long taper transition length. A detail discussion on the adiabatic criteria and optimal shapes for tapered fiber will be presented in the next section.

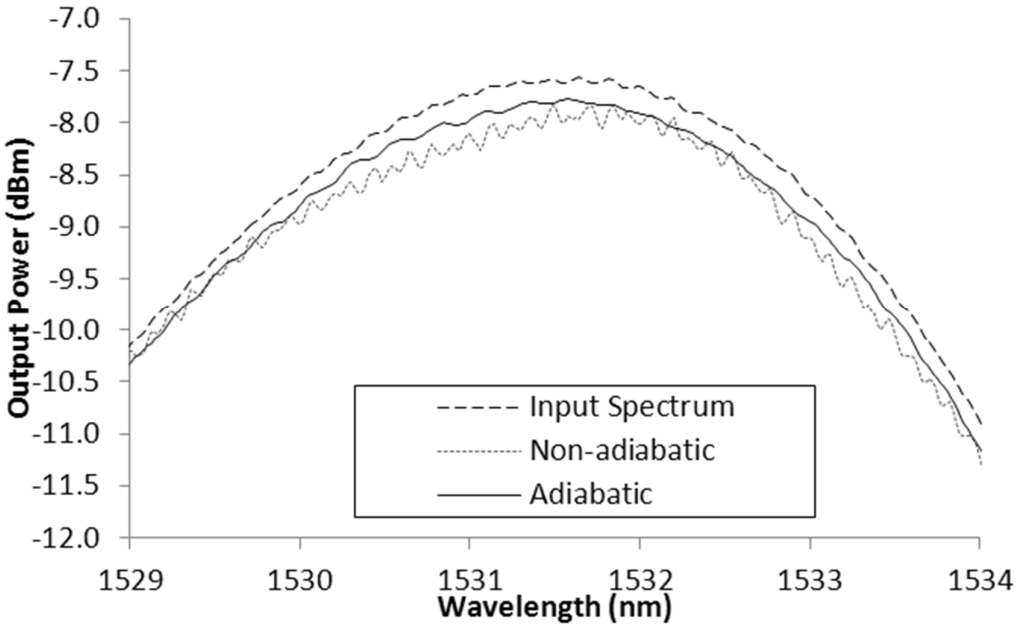

Figure 3.11: Output spectra from a microfiber with 10 cm long and ~3 µm waist diameter. Input spectrum from EDFA (dashed), adiabatic taper (solid) and non-adiabatic taper (dotted)

3.4 Adiabaticity Criteria

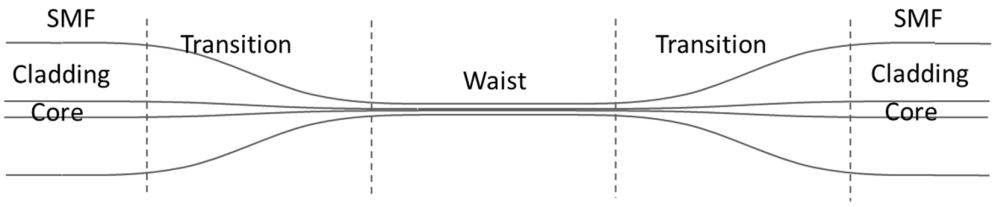

Figure 3.12: Typical diameter profile of a tapered fiber

Tapered fiber is fabricated by stretching a heated conventional SMF to form a structure of reducing core diameter. As shown in Figure 3.12, the smallest diameter part of the tapered fiber is called waist. Between the uniform unstretched SMF and waist are the transition regions whose diameters of the cladding and core are decreasing

from rated size of SMF down to the order micrometer or even nanometer. As the wave propagating through the transition regions, the field distribution varies with the change of core and cladding diameters along the way. Associate with the rate of diameter change of any local cross section, the propagating wave may experience certain level of energy transfer from the fundamental mode couples to a closest few higher order modes which are most likely to be lost. The accumulation of this energy transfer along the tapered fiber may result to a substantial loss of throughput. This excess loss can be minimized if the shape of the fabricated tapered fiber satisfies the adiabaticity criteria everywhere along the tapered fiber [14, 17].

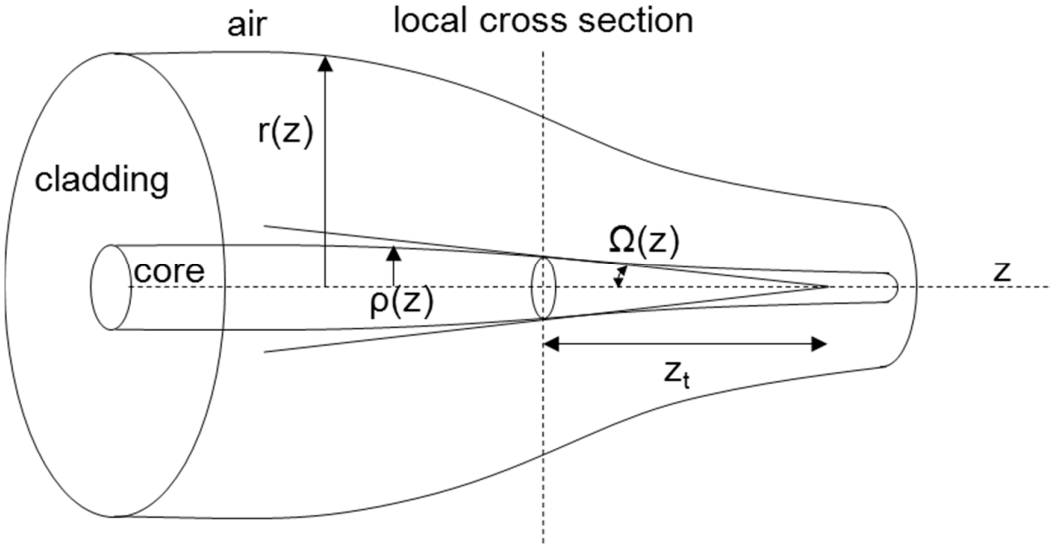

Figure 3.13: Illustration of the taper transition

Figure 3.13 gives an illustration of a tapered fiber with decreasing radius. z denotes the position along the tapered fiber. Theoretically, an adiabatic tapered fiber is based on the condition that the beat length between fundamental mode LP_{01} and second local mode is smaller than the local taper length-scale z_t.

$$z_b < z_t \tag{3.2}$$

Refer to illustration in Figure 3.13, z_t is given by

$$z_t = \rho / \tan\Omega \tag{3.3}$$

where ρ= ρ(z) is the local core radius and Ω= Ω(z) is the local taper angle.

The beat length between two modes is expressed as

$$z_b = \frac{2\pi}{\beta_1 - \beta_2} \tag{3.4}$$

where $\beta_1 = \beta_1(r)$ and $\beta_2 = \beta_2(r)$ are the propagation constants of fundamental mode and second local mode respectively. From the above equations, inequality of the tapered fiber can be derived as;

$$\left|\frac{d\rho}{dz}\right| = \tan\Omega < \frac{\rho(\beta_1 - \beta_2)}{2\pi} \tag{3.5}$$

where $\frac{d\rho}{dz}$ is the rate of change of local core radius with respect to the taper length and its magnitude is equivalent to $\tan\Omega$. For the convenience of usage and analysis, the inequality can also be rewritten as a function of local cladding radius r=r(z) as;

$$\left|\frac{dr}{dz}\right| < \frac{r(\beta_1 - \beta_2)}{2\pi} \tag{3.6}$$

Based on this condition, adiabatic tapered fiber can be acquired by tapering a fiber at a smaller reduction rate in diameter but this will result to a longer transition length. Considering practical limitations in the fabrication of fiber couplers or microfiber based devices, long tapered fiber may create difficulty in fabrication. For the purpose of miniaturization, short tapered fiber is preferable. To achieve balance between taper length and diameter reduction rate, a factor f is introduced to the inequality of (3.6) and yields

$$\frac{dr}{dz} = -\frac{fr(\beta_1 - \beta_2)}{2\pi} \tag{3.7}$$

where the value of f can be chosen between 0 to 1. Optimal profile is achieved when f = 1. Practically, tapered fiber with negligibly loss can be achieved with f = 0.5 but the transition length of the tapered fiber is twice longer than that of the optimal tapered fiber.

3.4.1 Theoretical Analysis on Shape of Tapered Fiber

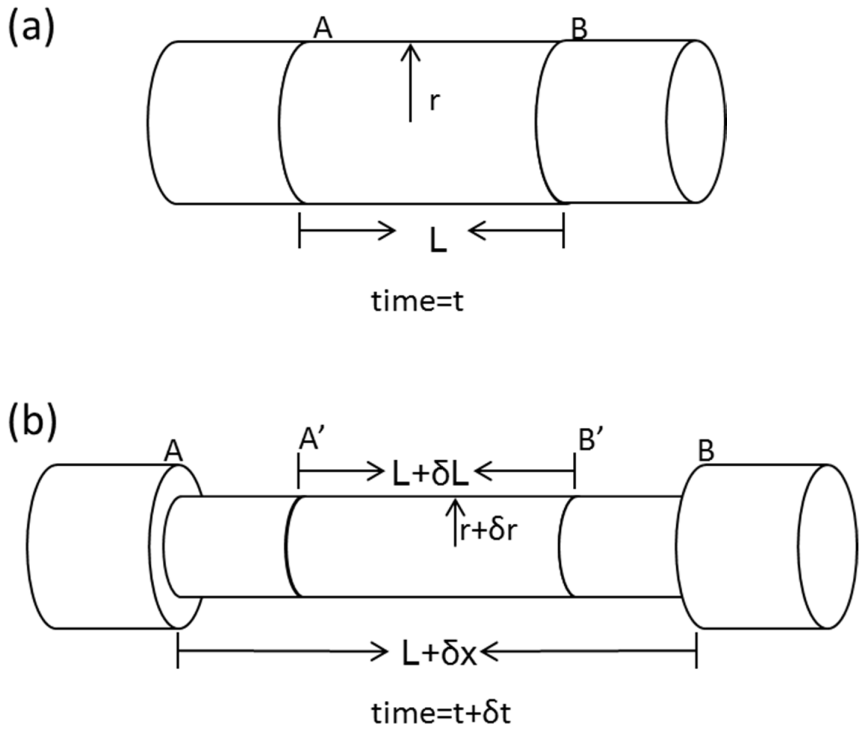

Figure 3.14: (a) The cylinder illustrates a heated SMF (b) A short while later, the diameter of the heated SMF has been reduced when it is stretched

When a glass element is heated, there is a small increment in the volume under the thermal expansion effect. However, the change in volume is negligibly small not to mention that the volume expansion wears off very quickly once the heat is dissipated from the mass. It is reasonable to assume that the total volume of the heated fiber is conserved throughout the entire tapering process. Based on this explanation, when a heated glass fiber is stretched, the waist diameter of the fiber is reduced. The calculation of varying waist diameter and length of extension can be made based on the idea of 'conservation of volume'[14]. Birks et. al. has presented simple mathematical equations to describe the relationship between shapes of tapered fiber, elongation distance and hot-zone length. Any specific shape of tapered fiber can be controlled by manipulating these parameters in the tapering process. Figure 3.14 provides schematic illustrations of

heated fiber with reducing waist diameter during the elongation process. At time t, the heated fiber bounded between cross sections A and B has a length equivalent to the hot-zone length L and the waist diameter is denoted by r. After a short interval of time δt, the heated fiber is stretched and the length is extended to $L + \delta x$. The diameter of heated fiber becomes $r + \delta r$ where δr denotes the change in the waist radius. The volume of the stretched fiber at time $t + \delta t$ should be the same with the volume at time t

$$\pi(r+\delta r)^2(L+\delta x)=\pi r^2 L \tag{3.8}$$

After some algebraic manipulations, a differential equation can be obtained from Eqn (3.8) by neglecting the higher order of δr and δx;

$$\frac{dr}{dx}=-\frac{r}{2L} \tag{3.9}$$

The function of radius profile is given by the integral

$$r(x)=r_0\exp\left(-\frac{1}{2}\int\frac{dx}{L}\right) \tag{3.10}$$

where r_0 denotes the initial radius of the fiber.

To relate the varying hot-zone length L with the elongation distance x during the tapering process, L can be replaced with any function of x. Linear function in (3.11) makes a convenient function for the integral in Eqn (3.10).

$$L(x)=L_0+\alpha x \tag{3.11}$$

where α is a constant ranges from -1 to 1.

$$r(x)=r_0\exp\left(-\frac{1}{2}\int\frac{dx}{L_0+\alpha x}\right) \tag{3.12}$$

$$r(x)=r_0\left(1+\frac{\alpha x}{L_0}\right)^{-1/2\alpha} \tag{3.13}$$

To relate elongation distance x with the position on taper transition z, another equation is derived by referring to model in Figure 3.15. L_o in Figure 3.15(a) denotes

the initial hot-zone length bounded by cross-sections *P* and *Q* of the fiber while *x* denotes the elongation distance. Consider the heated fiber is elongated to form a biconical shape. The elongation results in two identical extensions of taper on both sides of the hot zone, each length of *x*/2. After tapering for time = *t*, *P* and *Q* have been elongated for an extension of *x* and the length of the taper waist is *L*. Based on the above description, it is easy to obtain the following equation

$$2z + L = x + L_o \tag{3.14}$$

where $L = L(x)$.

Substituting Eqn (3.14) to Eqn (3.13) yields

$$r(z) = r_0\left(1+\frac{2\alpha z}{(1-\alpha)L_0}\right)^{-1/2\alpha} \tag{3.15}$$

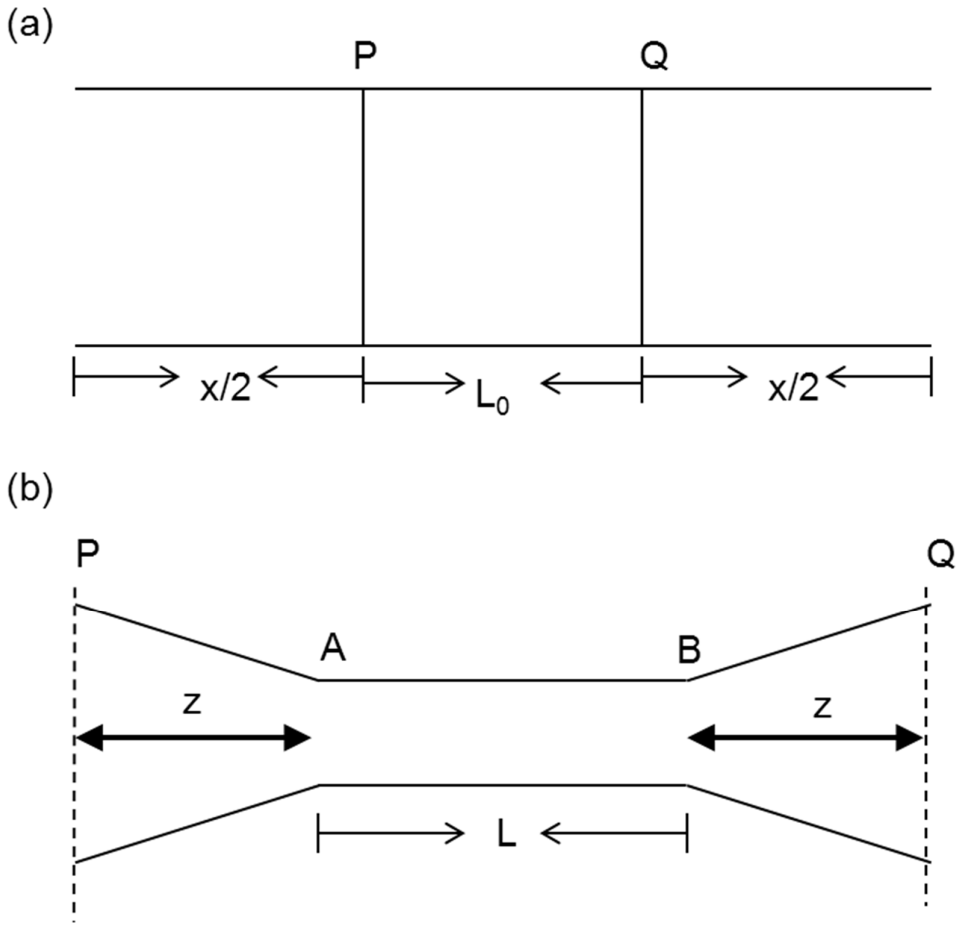

Figure 3.15: (a) Shape of a fiber at the beginning (*t* = 0) (b) shape of a tapered fiber after tapering (time = *t*)

By manipulating the value of α, several shapes of tapered fiber can be produced such as reciprocal curve, decaying-exponential, linear and concave curve. Several examples of calculated taper shape based on different values of α can be found in the literature of [14]. Consider the case of tapered fiber with decaying-exponential profile as shown in Figure 3.16, the fabrication of such tapered fiber requires a constant hot-zone length (α = 0). From the theoretical model presented above, the function for the decaying-exponential profile is given by

$$r(z) = r_o e^{-z/L_0} \tag{3.16}$$

Based on this profile function, narrower taper waist can be achieved by using a small hot-zone length in the fabrication or drawing the taper for a longer elongation distance. Tapered fiber with short transition length can achieved from reciprocal curve profile based on positive value of α particularly with α = 0.5.

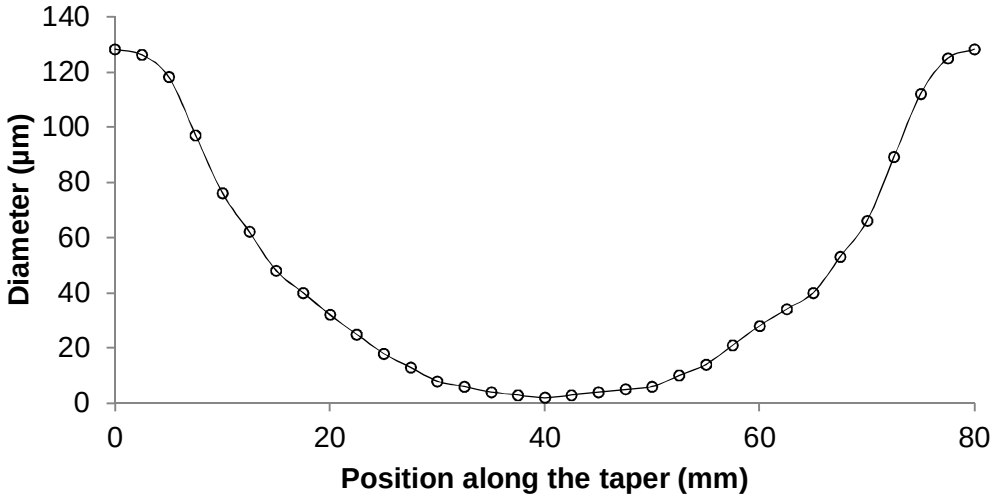

Figure 3.16: A tapered fiber with decaying-exponential profile fabricated using a constant hot-zone L_0 = 10 mm.

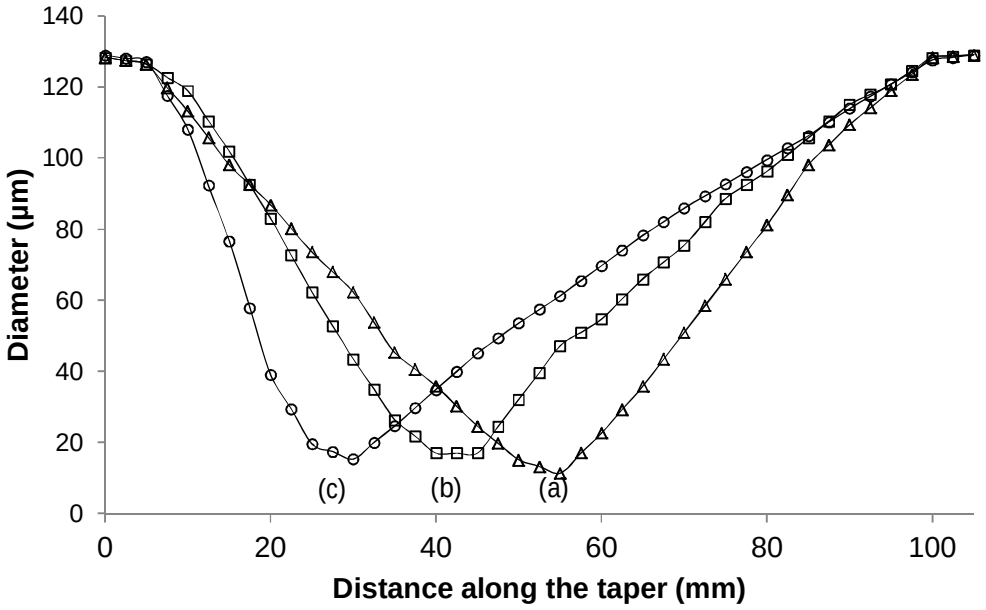

Figure 3.17: Three linear taper profiles (a-c) with its smallest waist point at different positions on the tapered fibers. Profile (a) has its smallest waist point at the center of the tapered fiber.

Linear taper profile can be produced using α = -0.5. Figure 3.17(a) shows a typical example of linear taper profile where its smallest waist point is at the center of the tapered fiber. By doing some simple modification on the tapering process, the smallest waist point can be shifted away from the center to one side of the tapered fiber as shown by profiles (b) and (c) of Figure 3.17. These profiles are found useful in the fabrication of wideband chirped fiber Bragg gratings (CFBG), in which the grating is written on the transitions of the tapered fiber. Long linear shape tapers make good candidates for the fabrication of such devices [18-21]. On the other hand, linear profile tapers can be used for optical tweezing because of its capability to converge the optical wave to a high intensity at the taper tip [22, 23]. Microscopic objects are attracted to the high intensity field driven by the large gradient force at the taper tip. Figure 3.18 gives a good example of such tapered fiber with 15cm linear taper profile. It is produced by using a long initial hot zone length L_o = 7cm and long elongation distance.

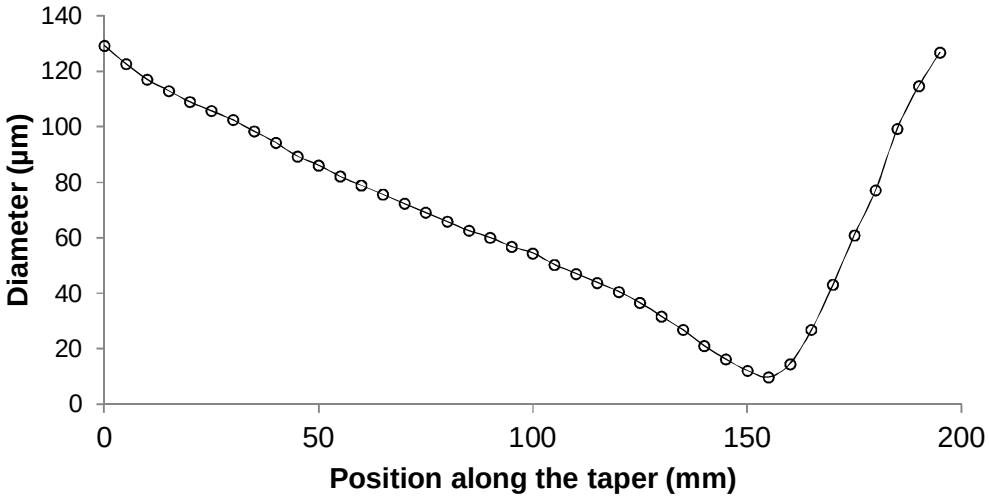

Figure 3.18: The diameter of tapered fiber is linearly decreasing from ~128 µm to ~10 µm along the 15 cm transition.

3.5 Throughput power of a degrading tapered fiber

The humidity in Malaysia is very high and it varies between 70-90% throughout the year. The concentration of water moisture in the air is extremely high and very 'hazardous' to tapered fibers. The deposition of particles (dust) and water moisture on the microfiber is one of the major factors that causes adsorption and scattering of light and the transmission of microfiber decays over time [15].

In an unprotected environment, freestanding tapered fibers may sway in the air due to the air turbulence. A small mechanical strength induced can cause cracks in the glass structure and result to an unrecoverable loss in the tapered fibers [24].

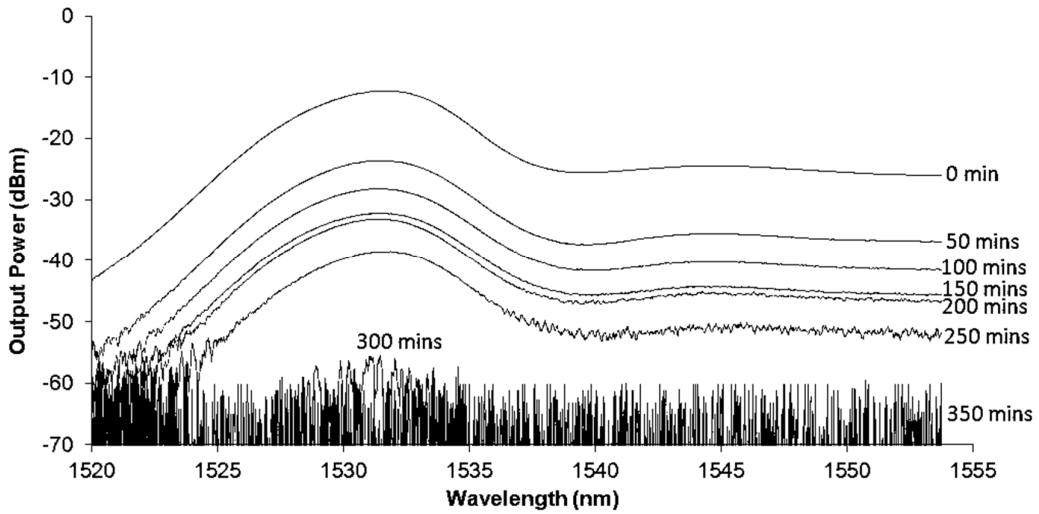

Figure 3.19: The throughput power of the 10 cm long and ~3 μm diameter tapered fiber degrades over time.

Figure 3.19 shows the output spectra of a tapered fiber with degrading transmission. After the tapered fiber was drawn, it was left hanging in an open air and transmission spectrum was scanned and recorded every 50 minutes as presented in Figure 3.19. Over the time, the deposition of dust and water molecules on the taper waist accumulated and formation of cracks increase the insertion loss of the tapered fiber. The output power of the tapered fiber dropped monotonically and eventually the power had gone too low and beyond detection after 350 minutes. The throughput of the tapered fiber can be recovered by flame brushing again as suggested in [24] but there is a risk that the tapered fiber can be broken after several times of flame brushing and this solution is not practical. However, more experimental study on the power degradation due to dust and vapour is essential to strengthen the understanding of this phenomenon. On the other hand, free standing tapered fibers are vulnerable to air turbulence or any sharp objects. Therefore, new strategies for handling these tapered fibers are crucial for the ensuing research and fabrication of microfiber devices. In order to achieve that, we have been motivated to devise a packaging method to address all the problems mentioned earlier which will be discussed in the next section.

3.6 Embedding Microfiber Photonic Devices in the Low-index material

Besides the fast aging of bare microfiber in the air, the portability is another issue encountered when the microfiber is required at a different location. Moving the fabrication rig to the desired location is one way of solving the problem but it is not a practical solution. Without a proper technique, it is risky to remove the tapered fiber from the fiber tapering rig and delivering it intact to another location. Xu et. al. [25] had demonstrated embedding microfiber coil resonators in the low-index material named Teflon. Microfiber or microfiber device can be coated with or embedded in Teflon by applying some Teflon resin in solution on them and leave the solution to dry for several ten minutes. The resin is solidified after the solvent has evaporated from the solution, the optical properties and mechanical properties of the microfiber devices can be well preserved in the material for a very long time. Jung et. al. had taken slightly different approach by embedding microfiber devices in a low-index UV-curable resin. The resin is solidified by curing it with ultra-violet light (UV) [26]. In the following section, the demonstration of the microfiber device embedded in the low-index UV-curable resin is presented.

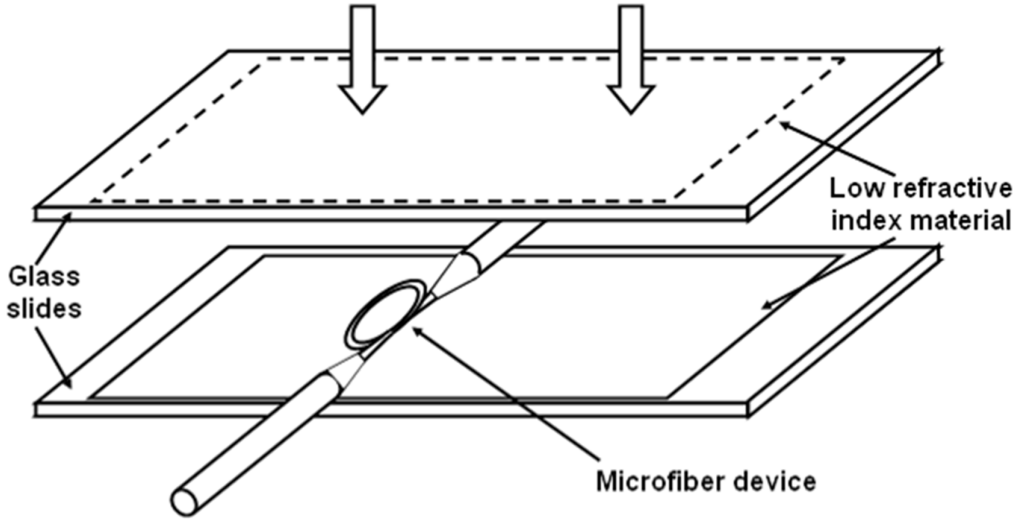

Figure 3.20: Illustration of microfiber device embedded in a low refractive index material and sandwiched between two glass plates.

First, the assembled microfiber device is laid on an earlier prepared glass plate with a thin and flat layer of low refractive index (RI) material (UV-Opti-clad 1.36RCM from OPTEM Inc.) that has an RI of 1.36 at 1550 nm as shown in Figure 3.20. The thickness of the low RI material is approximately 0.5 mm which is thick enough to prevent leakage of optical power from the microfiber to the glass plate. Some uncured resin is also applied to the surrounding of the microfiber device before it is sandwiched by another glass plate with the same low RI resin layer from the top. It is essentially important to ensure that minimum air bubbles and impurity are trapped around the fiber area between the two plates. This is to prevent RI non-uniformity in the surrounding of microfiber that may introduce loss to the system. During the tapering, coiling and coating processes, we monitored both the output spectrum and the insertion loss of the device in real time using the ASE source in conjunction with the OSA. The uncured resin is solidified by the UV light exposure for 3 ~7 minutes and the optical properties of the microfiber device are stabilized. The image of the end product is as shown in Figure 3.21.

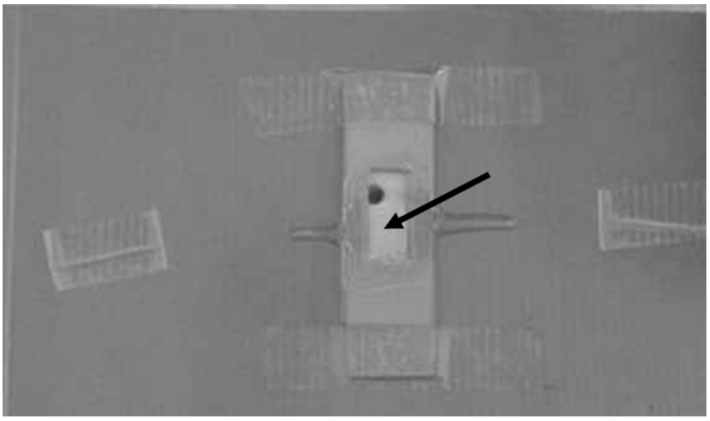

Figure 3.21: The image of the end product of an embedded MLR in the low-index resin.

3.7 Transmission Spectrum Variation During Embedding Process

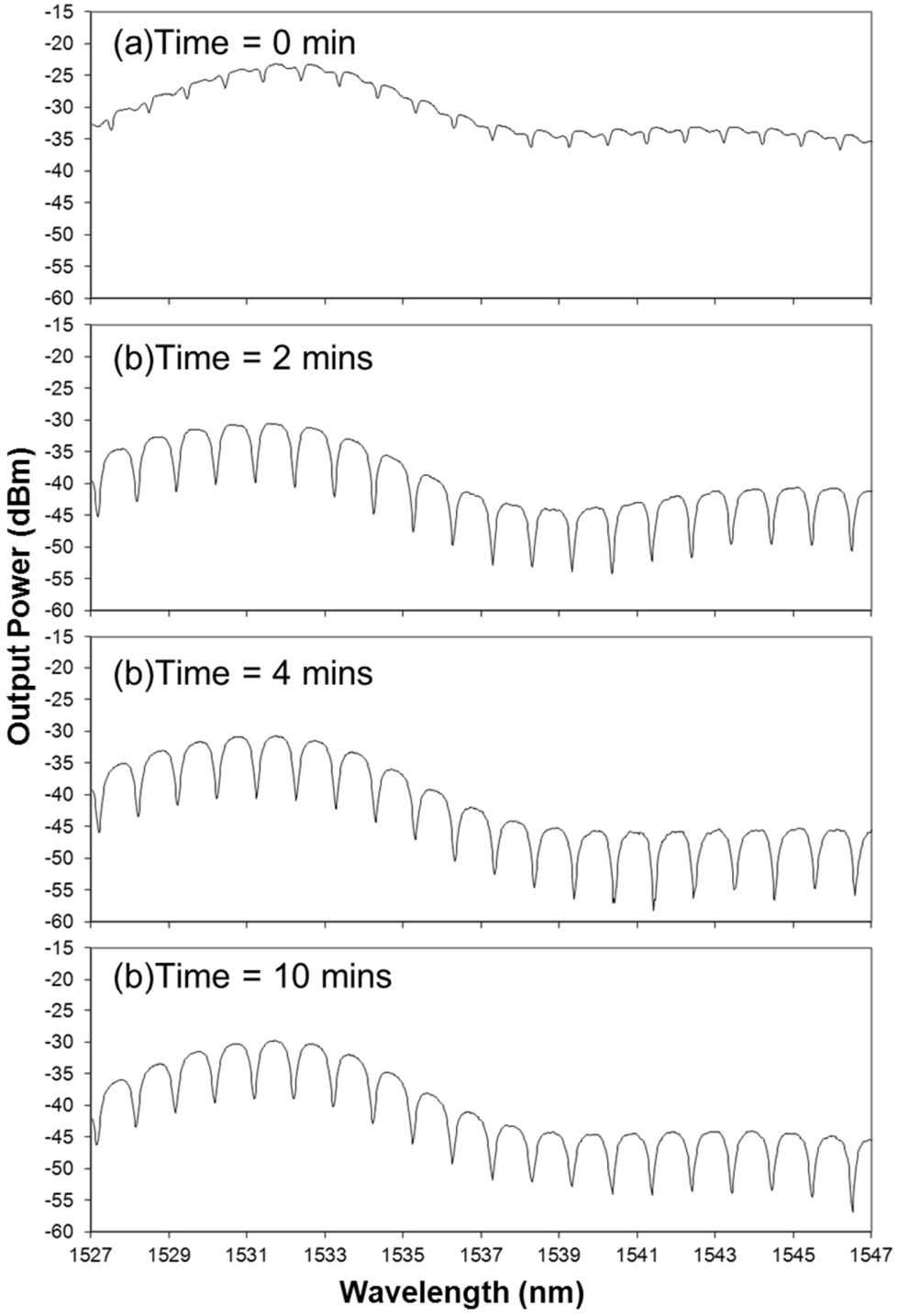

Figure 3.22: Embedding an MKR in a low-index material. The time in each graph indicates when the output spectrum of the MKR is recorded. a) MKR is freestanding in the air b) some low-index resin applied on the MKR c) UV curing is initiated and d) resin is solidified.

Figure 3.22 shows recorded output spectra of the microfiber knot resonator (MKR) at several intermediate times during the process of embedding it in a low-index UV-curable resin. The first spectrum in Figure 3.22(a) was recorded right after a MKR was assembled. The fringes in the spectrum indicate that the resonance condition has been achieved in the MKR but the resonance extinction ratio remained appalling at ~3 dB. The MKR was benignly laid on an earlier prepared glass slide with thin layer of low RI material. After that, some low-index resin (RI ~1.36) in solution was applied onto the MKR by using a micropipette. Figure 3.22(b) shows the stabilized output spectrum of the MKR and the improved resonance extinction ratio, ~10 dB. This phenomenon can be attributed to the reduction of microfiber-ambient index contrast; the mode field diameter (MFD) of the microfiber was expanded when it was immersed in the resin and the coupling efficiency of the MKR was altered. The changes of coupling coefficient and round-trip loss of the MKR may have induced critical coupling condition in the MKR and improve the resonance extinction ratio. At time = 4 minutes, UV-curing was initiated and a little bit of fluctuation was observed in the output power and extinction ratio (refer Figure 3.22(c)) during the curing process. After UV-curing for 6 minutes, the output spectrum became very stable and the resin was solidified. Figure 3.23 shows the optical microscope image of the embedded MKR in UV-curable resin.

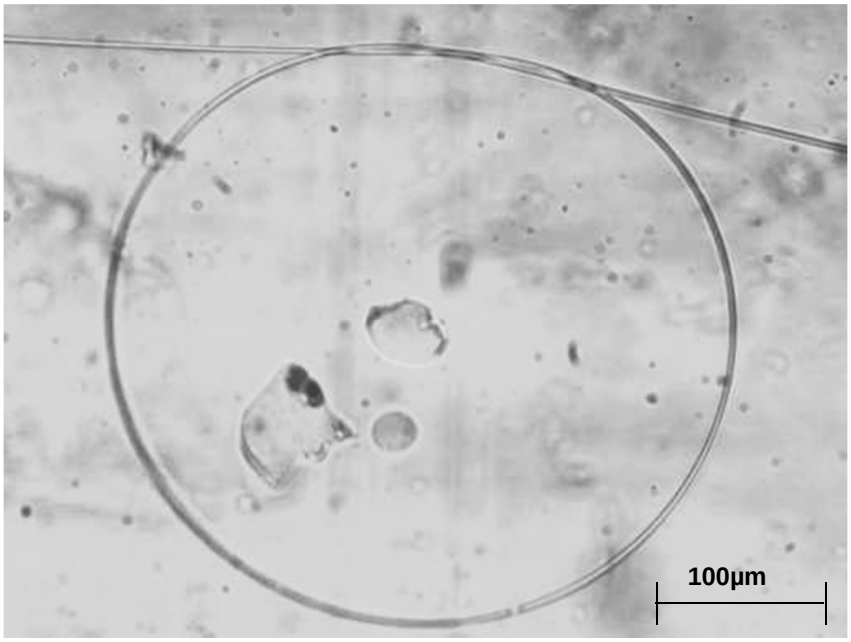

Figure 3.23: Optical microscope image of an MKR embedded in UV-curable resin.

3.8 Packaging tapered fiber in an Acrylic Case

Tapered fibers are susceptible to the air turbulence and the pollution of dust and moisture when exposed to air. It is very fragile when removed from the fiber tapering rig and maintaining the cleanliness of the tapered fiber in an unprotected condition is difficult. However, another simple packaging method had been devised to address all the difficulties mentioned.

For the purpose of long term usage and ease of portability of the tapered fiber, a proper packaging process is essential. Some literatures suggest embedding microfiber devices in the low-index Teflon [25] or UV-curable resin [26] to maintain the physical structure and resonance condition of the devices. Although, the refractive indices of the materials are in the range of 1.3~1.4 which is slightly lower than the RI of silica tapered fiber and the mode can be still be confined within the tapered fiber but some optical properties such as numerical aperture (NA) and mode field diameter (MFD) will be altered due to the change in index contrast between silica microfiber and ambient medium when embedded in the low-index material. In the context of maintaining small

confinement mode area and high optical nonlinearity, this method may not be a good idea.

A packaging method has been devised to keep tapered fiber in an Acrylic case. The taper waist is kept straight and surrounded by the air without having any physical contact with any substance or object thus maintaining its optical properties in the air. The following part of this section provides detail descriptions of this packaging method.

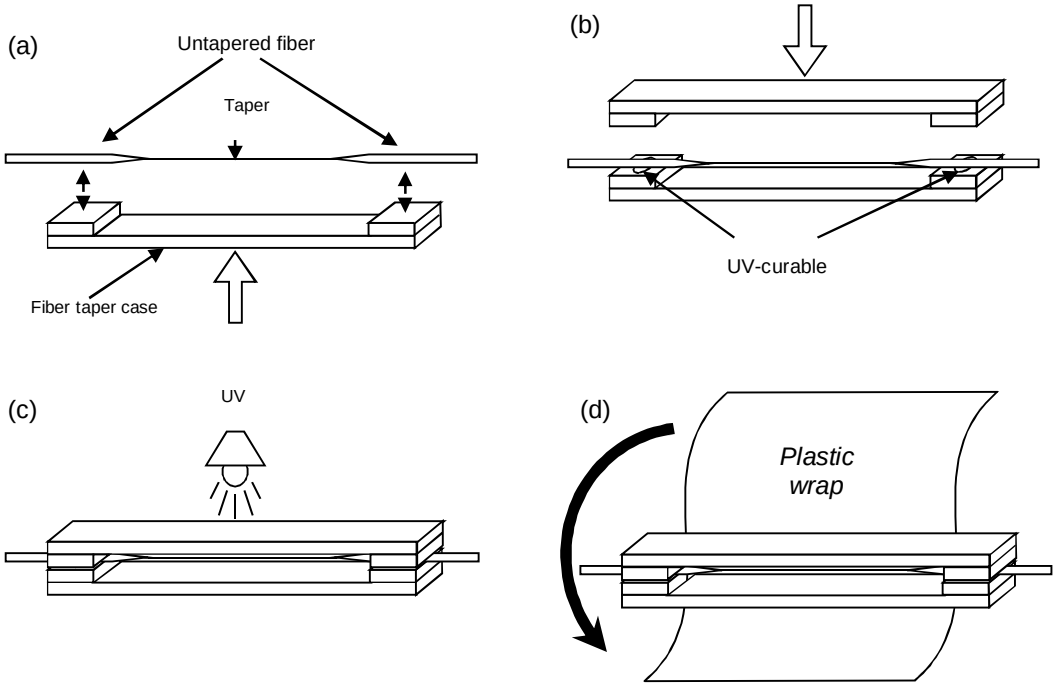

Figure 3.24: Schematic illustration for tapered fiber packaging process

First, an earlier prepared acrylic tapered fiber case which is made of several small acrylic pieces with a thickness of 2.5 mm is used in housing the tapered fiber. The acrylic case mainly comprises of a lower part and upper part. Both parts of the acrylic case are specially prepared in such a way that the benches at both ends of the acrylic case are positioned exactly at the untapered parts of the tapered fiber. After a fresh tapered fiber is drawn, the lower part of the acrylic case is carefully placed at the bottom and in parallel with the tapered fiber. That can done with the assistance of an additional translation stage. The acrylic case is slowly elevated upward until both

benches touch both untapered parts of the tapered fiber as shown in Figure 3.24(a). After that, some UV-curable optical adhesive (Norland Product, Inc) is applied to the untapered fibers that lay on the benches before the upper part of the tapered fiber case covers the tapered fiber from the top as shown in Figure 3.24(b). The UV-curable adhesive is used to adhere both the upper part and the lower part of fiber taper case. Although the RI of the optical adhesive (~1.54) is higher than silica glass (1.44) but the adhesive is only applied to untapered fiber and the light confined within the core of the fiber remains unaffected. To cure the UV-curable adhesive, 9W mercury-vapour lamp that emits light at ~254 nm is used. Depending on the adhesive volume and its distance from the mercury-vapour lamp, the curing time takes for 2-8 minutes. After the adhesive is solidified and both case parts are adhered to each other as shown in Figure 3.24(c). During the packaging process illustrated in Figure 3.24(a)-(c), the fiber taper is held by the two fiber holders in fiber taper rig and this helps to keep the fiber taper straight until the UV-curing process is completed. After that the fiber taper and its case can safely removed from the fiber holders. The fiber taper packaged inside the acrylic case may remain straight permenantly. In the contrary, the fiber taper may suffer higher insertion loss if the taper fiber is bend during the packaging process. On the other hand, it is essential to prevent any physical contact between the taper waist with human hands or other objects. The dust or moisture on the fiber taper may introduce loss to the transmission. In the final step, the acrylic case is sealed by wrapping it with a piece of plastic wrap. This can minimize the pollution of dust or air moisture in the acrylic case for a very long period of time. This fiber taper can be kept in storage for a week and possibly a fortnight without having an increment of loss more than 1.5 dB however it is subject to taper dimension and its usage in the experiment.

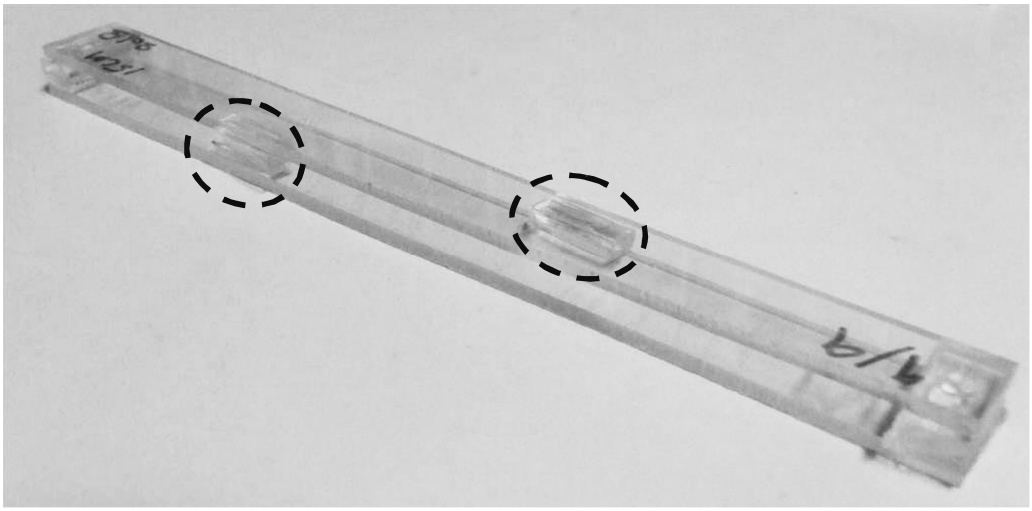

Figure 3.25: A reinforced 20 cm long fiber taper case by additional acrylic pieces (in dashed circles).

In packaging long fiber taper (> 100 mm), long acrylic case is susceptible to bending and the fiber taper packaged could be damaged. However, the case structure can be reinforced by placing additional small acrylic pieces between upper and lower parts of the acrylic case and joint them with some adhesive. Figure 3.25 shows the end product of a reinforced fiber taper case.

Throughput power of a fiber taper in Acrylic case

(a)

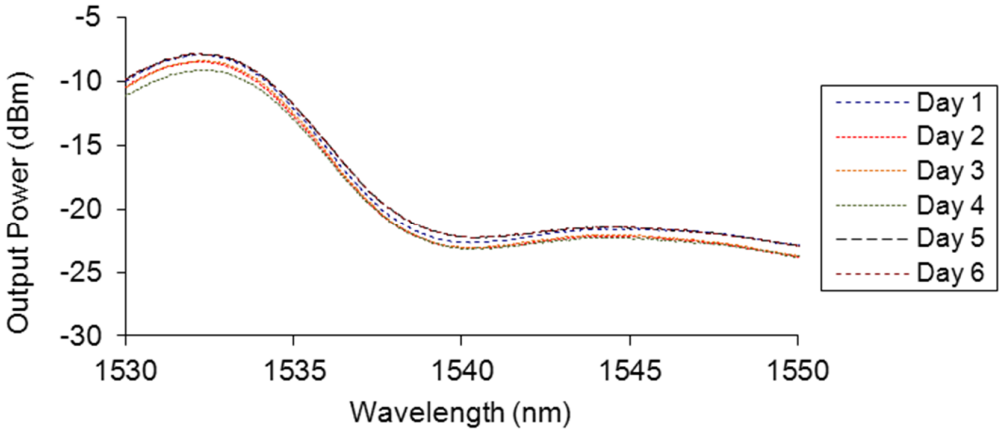

(b)

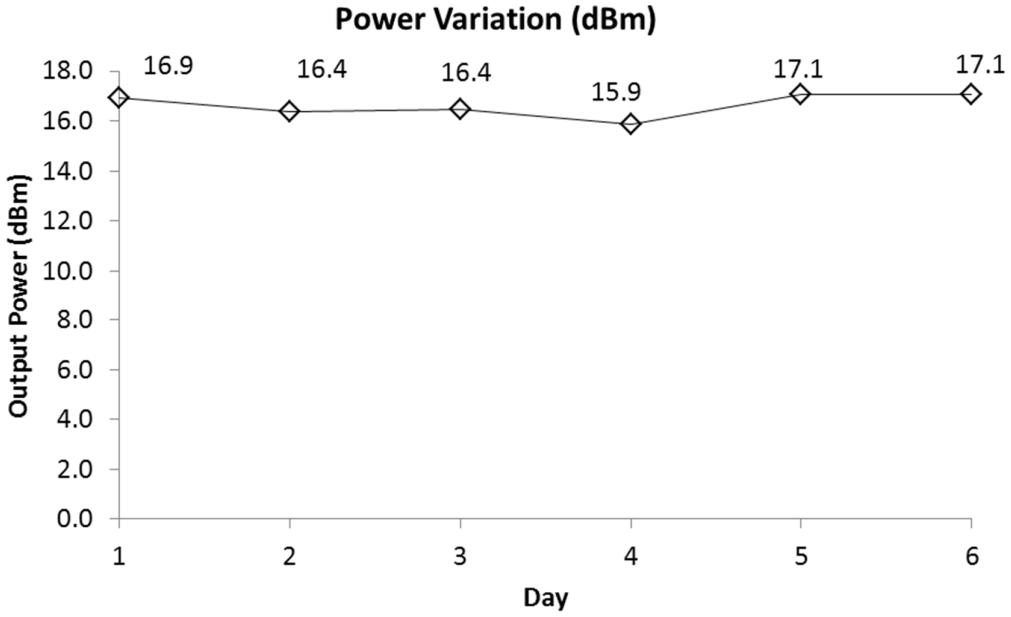

Figure 3.26: The 6 days comparison of (a) output spectrum and (b) total output power of the 10 cm long and ~3 µm diameter tapered fiber packaged in acrylic case.

To observe the characteristic of the tapered fiber as well as the reliability of the tapered fiber case over time, an observation on the transmission spectrum is conducted on the packaged tapered fiber for 6 days. Figures 3.26(a) and 3.26(b) show the 6 days output spectra observation of a packaged tapered fiber. Unlike the monotonic decrease in throughput power observed in Figure 3.19(a), the curve of every transmission spectrum is closely overlaid to each other with a small power variation < 1.2 dB in the graph. Refer to Figure 3.26(b), the variation of the total output power is spontaneous which can be attributed to the fluctuation of power at the ASE source and change of ambient temperature. In comparison with the taper fiber without packaging, obviously Acrylic case plays its role well in preserving the tapered fiber to a longer lifespan; it enables portability and allows integration with more complex optical fiber configurations away from the fiber tapering rig.

3.9 Dispersion Analysis and Measurement

Tapered fibers provide additional degrees of freedom in the manipulation of dispersion. By manipulating air-silica index contrast and taper waist diameter, the zero-dispersion wavelength of the tapered fiber can be tailored to any wavelength in a wide range from visible light to near infrared range [27]. Besides its small effective area and high nonlinearity, the zero dispersion wavelength is one of the important criteria in achieving some optical nonlinear effects such as ultrabroad supercontinuum generations [28] and four wave mixing effect [29]. Tapered fiber provides a large dispersion slope, high value of normal dispersion and anomalous dispersion. These properties can be exploited in dispersion management for many applications. For instance, tapered fiber can be used as a dispersion compensator to help minimizing the pulse broadening effect and bit error rate in optical communication system. In mode-locking applications, tapered fiber is integrated in the system to help achieving zero dispersion in the cavity of system and stabilizing the generation of short pulsed laser [30]. In addition, dispersion micro-management (DMM) in short tapered holey fiber is suggested for the generation of ultrashort pulse laser [31]. However predetermination of the dispersion is required before the deployment of tapered fiber in the systems. Over the years, several techniques for chromatic dispersion measurement have been suggested such as time-of-flight [32], phase-shift [33], degenerate-four-wave-mixing-based techniques [34], interferometric techniques based on Mach-Zehnder interferometer [35] or Michelson interferometer [36].

Experiment

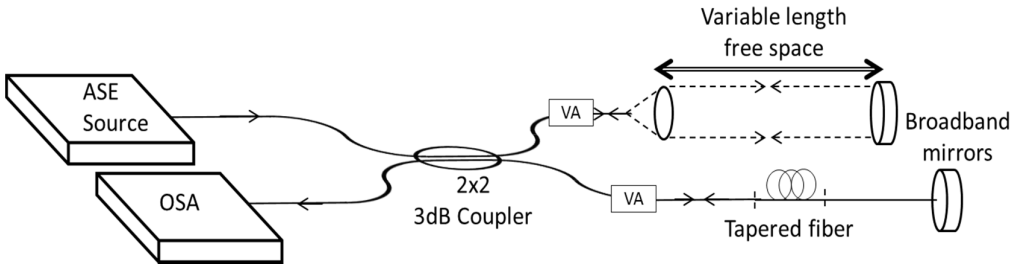

Figure 3.27: Schematic diagram of the dispersion measurement setup based on michelson interferometer.

In this section, a simple and effective dispersion measurement technique based on Michelson interferometry is demonstrated. The advantage of using this technique is its capability of measurement for fiber length shorter than a meter and it is suitable in the dispersion measurement for tapered fibers length < 40cm. As shown in Figure 3.27, the experimental setup of the Michelson interferometer mainly comprises of a 2x2 3 dB coupler, an ASE source that is connected to the input while OSA is connected to the output of the interferometer. The test arm of the interferometer contains a tapered fiber which is the fiber under test (FUT) in this measurement, a variable attenuator and a broadband mirror. The reference arm contains a variable attenuator, a fiber collimator and a broadband mirror.

When the input beam from the ASE source is injected to the interferometer, it is split into two beams at the 3 dB coupler and each of them enters reference arm and test arm respectively. After traversing through their respective arms, both beams are reflected back by the broadband mirrors and traverse through their respective arms for the second time. At the 3 dB couplers, the reflected beams recombine and interfere with each other before the output is fed to the OSA. Due to the cavity loss difference between test arm and reference arm, the output powers from both arms can be different. Thus it is very difficult to observe the fringes in the output spectrum of an imbalanced interferometry. To balance the output power from the two arms, the reflected powers

from both arms should equalized by manipulating the two variable attenuators. Fiber length in the reference arm (free space length excluded) should be the same as the fiber length in the test arm excluding the tapered fiber length so that the dispersion effect difference between two arms is limited to the free space and FUT only because fiber length mismatch can lead to measurement error. To measure the second order dispersion, the free space length in the reference arm should be equivalent to the optical path length of the tapered fiber so that the first order dispersion of the FUT can be omitted from the total dispersion effect. That can be achieved by placing the broadband mirror on the translation stage and vary the free space length using the translation stage.

Theory

Let E_R and E_T be the electric field amplitude of the beam from the reference arm and test arm respectively. (For the simplicity of representation and explanation, notations for reference arm and test arm are distinguished by their subscript symbol where *R* represents reference arm and *T* represents test arm.) Each beam propagates through their respective arm twice therefore their respectively optical path lengths are 2*d* and 2*L*.

$$E_R = e^{-j\beta_R 2d} \tag{3.17}$$

$$E_T = e^{-j\beta_T 2L} \tag{3.18}$$

where β_T and $\beta_R = \omega / c$ are the respective propagation constant.

Both beams recombine at the 3 dB coupler and the output spectrum is

$$I(\omega) = \left| E_T(\omega) + E_R(\omega) \right|^2 \approx 1 + \cos[\phi(\omega)] \tag{3.19}$$

where

$$\phi(\omega) = \beta_T(\omega)2L - \beta_R(\omega)2d \tag{3.20}$$

Expanding the propagation constant $\beta_T(\omega)$ into a Taylor series around frequency ω_0, Eqn (3.20) becomes

$$\phi(\omega) = \phi_0 + \left[\beta_1(\omega_0)2L - \frac{2d}{c} \right](\omega - \omega_0) + \frac{1}{2}\beta_2(\omega_0)2L(\omega - \omega_0)^2$$

$$+\frac{1}{6}\beta_3(\omega_0)2L(\omega - \omega_0)^3 + ... \quad (3.21)$$

where $\beta_1(\omega) = \frac{\partial \beta_T}{\partial \omega}$, $\beta_2(\omega) = \frac{\partial^2 \beta_T}{\partial \omega^2}$ and $\beta_3(\omega) = \frac{\partial^3 \beta_T}{\partial \omega^3}$

The free space length can adjusted such that

$$\beta_1(\omega_0)L = \frac{d}{c} \quad (3.22)$$

Thus nullifying the first order dispersion term in Eqn (3.21) and the expression becomes

$$\phi(\omega) = \phi_0 + \frac{1}{2}\beta_2(\omega_0)2L(\omega - \omega_0)^2 + \frac{1}{6}\beta_3(\omega_0)2L(\omega - \omega_0)^3 + ... \quad (3.23)$$

or it can be reexpressed as a function of wavelength λ

$$\phi(\lambda) \approx \phi_0 + \beta_2(\omega_0)L\left(\frac{2\pi c}{\lambda} - \frac{2\pi c}{\lambda_0} \right)^2 + \frac{1}{3}\beta_3(\omega_0)L\left(\frac{2\pi c}{\lambda} - \frac{2\pi c}{\lambda_0} \right)^3 \quad (3.24)$$

where the higher order terms are neglected. The relationship between dispersion coefficient and group velocity dispersion can then be expressed as;

$$D = -\frac{2\pi c}{\lambda^2}\beta_2(\omega) \quad (3.25)$$

Result and Discussion

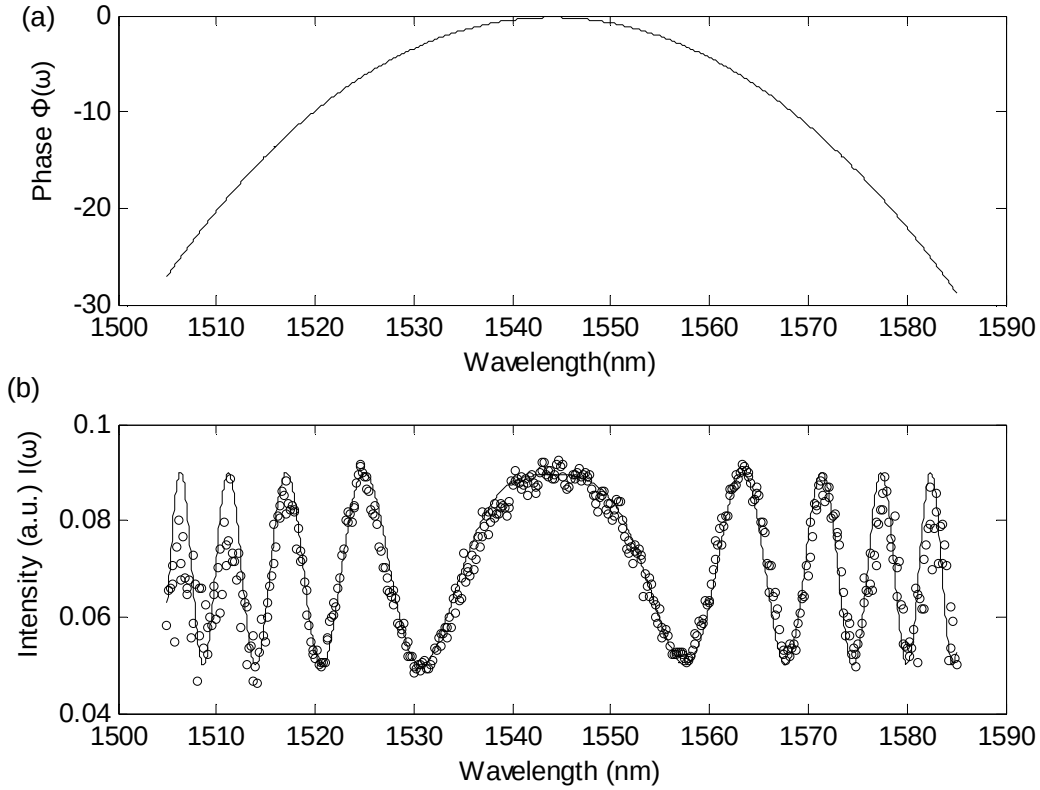

Figure 3.28: The (a) phase function and the (b) output spectrum of the interferometer. The circles represent the experimental result and the fitting curve is the analytical result.

Figure 3.28(b) shows the output spectrum of the interferometer based on a ~2μm diameter tapered fiber where the curve in Figure 3.28(a) is the corresponding phase function $\phi(\omega)$ of the output spectrum. Table 3.1 tabulates the parameters and values for the best-fit curve in Figure 3.28.

Table 3.1: Fitting parameters and values

Parameter	Value
L	8.5×10^{-5} km
λ_0	1544.1 nm
ϕ_0	- 0.2
$\beta_2(\omega_0)$	-307 ps^2/ km
$\beta_3(\omega_0)$	1 ps^3/ km
D(measured)	242 ps/(nm.km)
D(calculated)	260 ps/(nm.km)

The measured dispersion coefficient D = 242 ps/nm·km is very close to the calculated value 260 ps/nm·km for a ~2 μm diameter tapered silica fiber [27]. The key in fitting the curve to the experimental data is to ensure the center of the oscillating spectrum is aligned to the center wavelength of the ASE source which is also the wavelength of interest λ_0 in the measurement. Each fringe in the oscillating spectrum is precisely fitted according their peak wavelength and dip wavelength however the amplitude fitting is less important because the group velocity dispersion (GVD) $\beta_2(\omega_0)$ is independent from the oscillating amplitude. In the case of low dispersion slope, the oscillating spectrum is near-symmetry and the small value of the third order dispersion $\beta_3(\omega_0)$ can be assumed to be zero. However in the case of high dispersion slope, the oscillating spectrum may not be symmetry and the third order dispersion $\beta_3(\omega_0)$ and possibly the forth order dispersion $\beta_4(\omega_0)$ can be significant in the curve fitting.

In the dispersion measurement for FUT with low GVD, the distance between fringes is larger. The measurement accuracy can be compromised if the fringe spacing is in the same order or larger than the ASE source bandwidth. This shortcoming can be alleviated by increasing the lengths of the FUT and free space. However this may give rise to the increase of cavity loss in the interferometer and lead to noisy output spectrum. Therefore, careful selection of FUT length is important in the dispersion measurement.

3.10 Summary

In the past, several fabrication techniques for tapered fibers/microfibers have been suggested. In this chapter, two fabrication techniques used in this research are reviewed, namely chemical etching and flame brushing. In the investigation of chemical etching technique, the famous Turner's method is used in the fabrication. However, this method is susceptible to some environmental perturbations and thus affecting the

quality of end product. The tapered fiber suffers several setbacks in terms of asymmetrical shape of taper, large cone aperture and high surface roughness which are the major factors in affecting the throughput power of tapered fiber. These problems can be overcome by using tube etching method. The tube provides a protection to the etching process from the perturbations and produces tapered fibers with better quality. Since this technique has a limitation in the control of shape and length of tapered fibers, flame brushing technique that higher flexibility is proposed in this work.

Flame brushing technique is commonly used for the fabrication of fiber couplers and tapered fibers. This technique enables fabrication of biconical tapered fibers which are important components for the manufacture of microfiber based devices. In order to achieve that, a fiber tapering rig is assembled. The heat source comes from an oxy-butane torch with a flame width of 1mm. Two stepper motors are incorporated in the rig to control the movement of the torch and translation stage. A biconical tapered fiber with a waist diameter as small as 400nm can be achieved with the rig. To achieve low loss tapered fibers, the shape of the taper should be fabricated according to adiabaticity criteria. In the laboratory, tapered fibers with linear and decaying-exponential profiles have been demonstrated. To provide protection to the tapered fibers, they are embedded in a low-index material or packaged into an Acrylic casing. These protection measures can prolong the life span and stabilize the temporal performance of these tapered fibers and microfiber based devices. Lastly, the chromatic dispersion measurement on tapered fiber is carried out based on Michelson Interferometry. The measured dispersion coefficient D is very close to the calculated value acquired from Zhang et. al.'s data [27].

In the next chapter, the fabrication of various optical devices from tapered fiber will be introduced and experimentally demonstrated. Theoretical model of each device will be presented to describe the transmission characteristics. The term microfiber will be known as tapered fiber.

References

[1] A. M. Morales and C. M. Lieber, "A Laser Ablation Method for the Synthesis of Crystalline Semiconductor Nanowires," *Science,* vol. 279, no. 5348, pp. 208-211, January 9, 1998 1998.

[2] J. Chen, M. A. Reed, A. M. Rawlett, and J. M. Tour, "Large On-Off Ratios and Negative Differential Resistance in a Molecular Electronic Device," *Science,* vol. 286, no. 5444, pp. 1550-1552, November 19, 1999 1999.

[3] J. Westwater, D. P. Gosain, S. Tomiya, S. Usui, and H. Ruda, "Growth of silicon nanowires via gold/silane vapor--liquid--solid reaction," *Journal of Vacuum Science & Technology B: Microelectronics and Nanometer Structures,* vol. 15, no. 3, pp. 554-557, 1997.

[4] G. Brambilla, V. Finazzi, and D. Richardson, "Ultra-low-loss optical fiber nanotapers," *Opt. Express,* vol. 12, no. 10, pp. 2258-2263, 2004.

[5] A. M. Clohessy, N. Healy, D. F. Murphy, and C. D. Hussey, "Short low-loss nanowire tapers on singlemode fibres," *Electronics Letters,* vol. 41, no. 17, pp. 954-955, 2005.

[6] X. Xing, Y. Wang, and B. Li, "Nanofibers drawing and nanodevices assembly in poly(trimethylene terephthalate)," *Opt. Express,* vol. 16, no. 14, pp. 10815-10822, 2008.

[7] S. Harun, K. Lim, A. Jasim, and H. Ahmad, "Fabrication of tapered fiber based ring resonator," *Laser Physics,* vol. 20, no. 7, pp. 1629-1631, 2010.

[8] F. Bilodeau, K. O. Hill, S. Faucher, and D. C. Johnson, "Low-loss highly overcoupled fused couplers: fabrication and sensitivity to external pressure," *Lightwave Technology, Journal of,* vol. 6, no. 10, pp. 1476-1482, 1988.

[9] P. Hoffmann, B. Dutoit, and R.-P. Salathé, "Comparison of mechanically drawn and protection layer chemically etched optical fiber tips," *Ultramicroscopy,* vol. 61, no. 1-4, pp. 165-170, 1995.

[10] D. R. C. T. Turner, Morris County, NJ), "Etch procedure for optical fibers," United States Patent, 1984.

[11] P. K. Wong, Wang, T., Ho, C.,, "Optical fiber tip fabricated by surface tension controlled etching," in *Proceedings of Solid. State Sensor* Actuator and Microsystems Workshop Transducers Research Foundation, Cleveland, Ohio, 2002, pp. 94-97.

[12] R. Stockle, C. Fokas, V. Deckert, R. Zenobi, B. Sick, B. Hecht, and U. P. Wild, "High-quality near-field optical probes by tube etching," *Applied Physics Letters,* vol. 75, no. 2, pp. 160-162, 1999.

[13] J. C. Graf, S. A. Teston, P. V. de Barba, J. Dallmann, J. A. S. Lima, H. J. Kalinowski, and A. S. Paterno, "Fiber taper rig using a simplified heat source and the flame-brush technique," in *Microwave and Optoelectronics Conference (IMOC), 2009 SBMO/IEEE MTT-S International*, 2009, pp. 621-624.

[14] T. A. Birks and Y. W. Li, "The shape of fiber tapers," *Lightwave Technology, Journal of,* vol. 10, no. 4, pp. 432-438, 1992.

[15] L. Ding, C. Belacel, S. Ducci, G. Leo, and I. Favero, "Ultralow loss single-mode silica tapers manufactured by a microheater," *Appl. Opt.,* vol. 49, no. 13, pp. 2441-2445, 2010.

[16] F. Orucevic, V. Lefèvre-Seguin, and J. Hare, "Transmittance and near-field characterization of sub-wavelength tapered optical fibers," *Opt. Express,* vol. 15, no. 21, pp. 13624-13629, 2007.

[17] J. D. Love, W. M. Henry, W. J. Stewart, R. J. Black, S. Lacroix, and F. Gonthier, "Tapered single-mode fibres and devices. I. Adiabaticity criteria," *Optoelectronics, IEE Proceedings J*, vol. 138, no. 5, pp. 343-354, 1991.

[18] O. Frazão and et al., "Chirped Bragg grating fabricated in fused fibre taper for strain–temperature discrimination," *Measurement Science and Technology*, vol. 16, no. 4, p. 984, 2005.

[19] J. Mora, A. Diez, M. V. Andres, P. Y. Fonjallaz, and M. Popov, "Tunable dispersion compensator based on a fiber Bragg grating written in a tapered fiber," *Photonics Technology Letters, IEEE*, vol. 16, no. 12, pp. 2631-2633, 2004.

[20] N. Q. Ngo, S. Y. Li, R. T. Zheng, S. C. Tjin, and P. Shum, "Electrically tunable dispersion compensator with fixed center wavelength using fiber Bragg grating," *Lightwave Technology, Journal of*, vol. 21, no. 6, pp. 1568-1575, 2003.

[21] J. Zhang, P. Shum, X. P. Cheng, N. Q. Ngo, and S. Y. Li, "Analysis of linearly tapered fiber Bragg grating for dispersion slope compensation," *Photonics Technology Letters, IEEE*, vol. 15, no. 10, pp. 1389-1391, 2003.

[22] Z. Liu, C. Guo, J. Yang, and L. Yuan, "Tapered fiber optical tweezers for microscopic particle trapping: fabrication and application," *Opt. Express*, vol. 14, no. 25, pp. 12510-12516, 2006.

[23] F. Xu, G. Brambilla, and D. J. Richardson, "Adiabatic SNOM tips for optical tweezers," ed, 2006.

[24] G. Brambilla, F. Xu, and X. Feng, "Fabrication of optical fibre nanowires and their optical and mechanical characterisation," *Electronics Letters*, vol. 42, no. 9, pp. 517-519, 2006.

[25] F. Xu and G. Brambilla, "Embedding optical microfiber coil resonators in Teflon," *Opt. Lett.*, vol. 32, no. 15, pp. 2164-2166, 2007.

[26] Y. Jung, G. S. Murugan, G. Brambilla, and D. J. Richardson, "Embedded Optical Microfiber Coil Resonator With Enhanced High-Q," *Photonics Technology Letters, IEEE,* vol. 22, no. 22, pp. 1638-1640, 2010.

[27] R. Zhang, J. Teipel, X. Zhang, D. Nau, and H. Giessen, "Group velocity dispersion of tapered fibers immersed in different liquids," *Opt. Express,* vol. 12, no. 8, pp. 1700-1707, 2004.

[28] T. A. Birks, W. J. Wadsworth, and P. S. J. Russell, "Supercontinuum generation in tapered fibers," *Opt. Lett.,* vol. 25, no. 19, pp. 1415-1417, 2000.

[29] M. D. Pelusi, F. Luan, E. Magi, M. R. Lamont, D. J. Moss, B. J. Eggleton, J. S. Sanghera, L. B. Shaw, and I. D. Aggarwal, "High bit rate all-optical signal processing in a fiber photonic wire," *Opt. Express,* vol. 16, no. 15, pp. 11506-11512, 2008.

[30] M. Rusu, R. Herda, S. Kivistö, and O. G. Okhotnikov, "Fiber taper for dispersion management in a mode-locked ytterbium fiber laser," *Opt. Lett.,* vol. 31, no. 15, pp. 2257-2259, 2006.

[31] Fei Lu, Yujun Deng, and Wayne H. Knox, "Generation of broadband femtosecond visible pulses in dispersion-micromanaged holey fibers," Opt. Lett. vol. 30, no. 12, pp.1566-1568, 2005.

[32] J. Hult, R. S. Watt, and C. F. Kaminski, "Dispersion Measurement in Optical Fibers Using Supercontinuum Pulses," *Lightwave Technology, Journal of,* vol. 25, no. 3, pp. 820-824, 2007.

[33] B. Costa, M. Puleo, and E. Vezzoni, "Phase-shift technique for the measurement of chromatic dispersion in single-mode optical fibres using LEDs," *Electronics Letters,* vol. 19, no. 25, pp. 1074-1076, 1983.

[34] L. F. Mollenauer, P. V. Mamyshev, and M. J. Neubelt, "Method for facile and accurate measurement of optical fiber dispersion maps," *Opt. Lett.,* vol. 21, no. 21, pp. 1724-1726, 1996.

[35] H.-T. Shang, "Chromatic dispersion measurement by white-light interferometry on metre-length single-mode optical fibres," *Electronics Letters,* vol. 17, no. 17, pp. 603-605, 1981.

[36] Q. Ye, C. Xu, X. Liu, W. H. Knox, M. F. Yan, R. S. Windeler, and B. Eggleton, "Dispersion Measurement of Tapered Air-Silica Microstructure Fiber by White-Light Interferometry," *Appl. Opt.,* vol. 41, no. 22, pp. 4467-4470, 2002.

Chapter 4

OPTICAL MICROFIBER DEVICES

4.1 Introduction

Optical microfiber devices have attracted growing interest recently especially in their simple fabrication methods. This is due to a number of interesting optical properties in this device, which can be used to develop low-cost, miniaturized and all-fiber based optical devices for various applications [1]. For instance, many research efforts have been focused on the development of microfiber/nanofibers based optical resonators that can serve as optical filters, which has many potential applications in optical communication, laser systems [2], and sensors [3, 4]. Many photonic devices that are conventionally fabricated into lithographic planar waveguides can also be assembled from microfibers. Recently, there are many microfiber devices have been reported such as microfiber loop resonator (MLR) [5, 6], microfiber coil resonator (MCR) [7-10], microfiber knot resonator (MKR) [11-13], reef knot microfiber resonator as an add/drop filter [14], microfiber Mach-Zehnder interferometer (MMZI) [15, 16] and etc. These microfiber based devices have the similar functionalities, characteristics and possibly the same miniaturizability with the lithographic planar waveguides. In future, these microfiber based devices may be used as building blocks for the larger and more complex photonic circuits.

In this chapter, the construction of the transmission spectrum and the corresponding theoretical model of these devices are presented. Three microfiber based devices, namely MLR, MKR and MMZI are demonstrated. In addition, some of the important optical properties of these devices will be reviewed and discussed.

4.2 Microfiber Loop Resonator (MLR)

MLRs are assembled from a single mode microfiber, which is obtained by heating and stretching a single mode fiber. In the past, many MLRs have been demonstrated. For instance, Caspar et. al. assembled a 2 mm diameter MLR from a 8.5 µm tapered fiber [17], which the coupling is compromised by the large thickness of the microfiber. However the deficiency was compensated by embedding the MLR in a silicone rubber which has lower and near to the refractive index of silica microfiber. Sumetsky et. al. had demonstrated fabrication of MLR from a ~1 µm diameter waist microfiber which has the highest loaded Q-factor of 120,000 [4]. Guo et. al. demonstrated wrapping a ~2 µm diameter microfiber loop around copper wire which is a high-loss optical medium. By manipulating the input-output fiber cross angle, the loss induced and the coupling parameter in the resonator can be varied. In the condition when the coupling ratio is equivalent to the round-trip attenuation, the MLR has achieved critical coupling and the transmission of resonance wavelength is minimum. Critical coupling condition has been achieved with resonance extinction ratio (RER) as high as 30 dB [1, 18]. In this section, the fabrication of a MLR is demonstrated using flame brushing technique. Theoretical analysis on the transmission characteristic of the MLR is also presented.

4.2.1 Fabrication of MLR

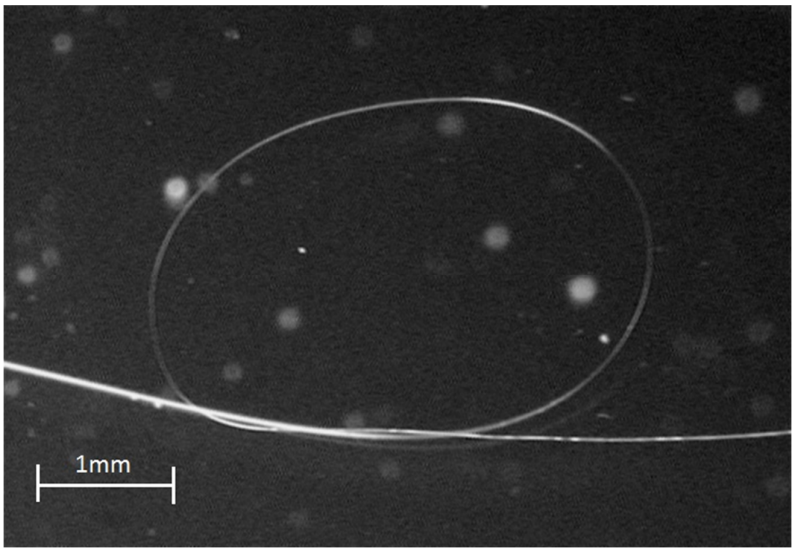

Figure 4.1: Optical microscope image of an MLR

Figure 4.1 shows an example of ~3 mm loop diameter MLR assembled from a ~2.0 µm waist diameter microfiber. Similar to other optical ring resonators, MLR has a 'ring' but manufactured from a single mode microfiber This fabrication can be carried out with the assistance of two 3D translation stages as illustrated in Figure 4.2. By aligning the three–axial position of each translation stage and twisting one of the pigtails, the microfiber is coiled into a loop. If the microfiber is sufficiently thin, the van der Waals attraction force between two adjacent microfibers is strong enough to withstand the elastic force from the bending microfiber and maintain the microfiber loop structure. The diameter of the loop can then be reduced by slowly pulling the two single mode fibers (SMFs) apart using the translation stages. Due the large evanescent field of the microfiber, a coupling region is established at the close contact between the two microfibers and a closed optical path is formed within the microfiber loop. Since the MLR is manufactured from an adiabatically stretched tapered fiber, it has a smaller connection loss. It does not have the input-output coupling issue encountered in many lithographic planar waveguides. Despite the difference in the physical structure and

fabrication technique between MLR and the conventional optical waveguide ring resonator, they share the same optical characteristics.

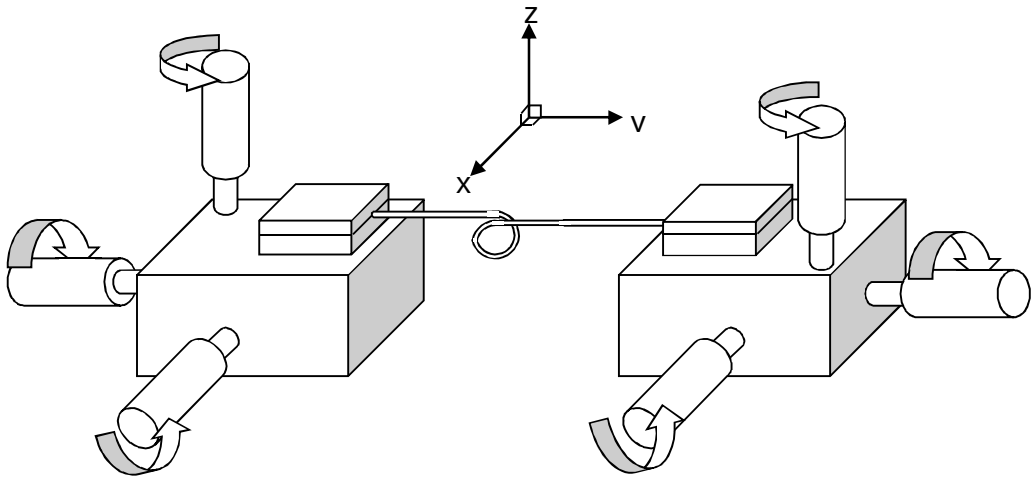

Figure 4.2: Manufacture of MLR by using two three-dimensional stages.

4.2.2 Theoretical Analysis

The microfiber guides light as a single mode waveguide, with the evanescent field propagating outside the microfiber. If the microfiber is coiled and two sections of microfiber are coupled, the strong evanescent field enables the modes in the two sections in proximity to overlap and create a close optical path (loop). There are several factors influencing the evanescent field such as the microfiber diameter, operating wavelength and the surrounding medium. The characteristic of the coupling is greatly affected by those factors too.

On every round-trip of light in the loop, there are fractions of light energy exchange between the two adjacent microfibers at the coupling region, the input light is allowed to oscillate in the closed loop and the resonance is strongest when a positive interference condition is fulfilled which can be related to this equation.

$$n\lambda_R = L \qquad (4.1)$$

where L is the round-trip length, λ_R is the resonance wavelength of the resonator and n is an integer. Positive interference occurs between the circulating waves to build up the wave intensity within the microfiber loop. The relationship in Eqn. (4.1) indicates that each wavelength is uniformly spaced and periodic in frequency, a well-known characteristic of an optical multichannel filter.

Characteristic Equations

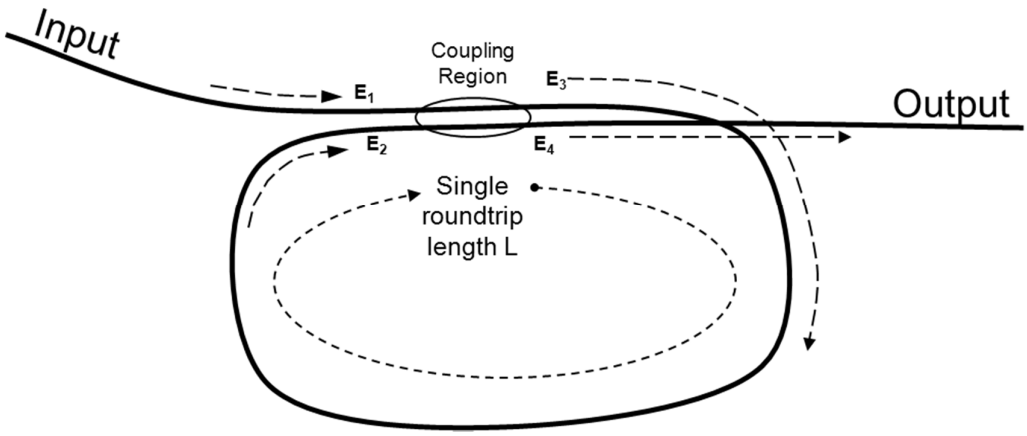

Figure 4.3: Schematic illustration of a self-touching loop resonator. The dashed arrows indicate the direction of waves in the resonator.

Figure 4.3 shows a schematic illustration of a self-touching loop resonator [19, 20]. The coupling region in the figure indicates the region where the mode interaction between the two fields of the coupled microfibers. The complex expressions in Eqn. (4.2) and (4.3) describe the mode-coupling interaction between the microfibers.

$$E_3 = (1-\gamma)^{1/2}\left[(1-\rho)^{1/2}E_1 + j\sqrt{\rho}E_2\right] \qquad (4.2)$$

$$E_4 = (1-\gamma)^{1/2}\left[j\sqrt{\rho}E_1 + (1-\rho)^{1/2}E_2\right] \qquad (4.3)$$

where notation E_1 and E_2 represent the two input wave field amplitudes while E_3 and E_4 represent the two output wave field amplitudes. The arrows in the figure show propagation direction of the waves in the resonator. ρ and γ represent the intensity coupling ratio and insertion loss.

Assume that the resonator is assembled from a microfiber of uniform diameter. E_2 and E_3 in the closed loop can be related by

$$E_2 = E_3 e^{-\alpha L/2} e^{\beta L} \tag{4.4}$$

where α is the intensity attenuation constant, β the propagation constant and L is the round-trip length.

Substitute Eqn. (4.4) into Eqn. (4.2),

$$E_2 e^{\alpha L/2} e^{-j\beta L} = (1-\gamma)^{1/2}\left[(1-\rho)^{1/2} E_1 + j\sqrt{\rho} E_2\right] \tag{4.5}$$

$$\rightarrow E_2 = \frac{(1-\gamma)^{1/2}(1-\rho)^{1/2} E_1}{e^{\alpha L/2} e^{-j\beta L} - j\sqrt{\rho}(1-\gamma)^{1/2}} \tag{4.6}$$

Substitute Eqn. (4.6) into Eqn. (4.3), we get

$$E_4 = j\sqrt{\rho}(1-\gamma)^{1/2} E_1 + \frac{(1-\gamma)(1-\rho)E_1}{e^{\alpha L/2} e^{-j\beta L} - j\sqrt{\rho}(1-\gamma)^{1/2}} \tag{4.7}$$

The transfer function of the MLR, T is given by the ratio of output field amplitude E_4 to the input field amplitude E_1

$$T = \frac{E_4}{E_1} = \frac{(1-\gamma) + j\sqrt{\rho}(1-\gamma)^{1/2} e^{\alpha L/2} e^{-j\beta L}}{e^{\alpha L/2} e^{-j\beta L} - j\sqrt{\rho}(1-\gamma)^{1/2}} \tag{4.8}$$

$$\rightarrow T = (1-\gamma)^{1/2} \frac{(1-\gamma)^{1/2} e^{-\alpha L/2} e^{j\beta L} + j\sqrt{\rho}}{1 - j\sqrt{\rho}(1-\gamma)^{1/2} e^{-\alpha L/2} e^{j\beta L}} \tag{4.9}$$

In the coupling condition where $\rho = 0$, there is no mode interaction between the microfibers in the coupling region. The transmitted light only experiences a single trip phase shift and same attenuation for all wavelengths along the L-length microfiber. Whereas at ρ = 1, the wave energy is completely transferred from one microfiber into the adjacent microfiber. In either case, MLR acts as an all-pass filter. In resonant condition, the numerator of the fraction in Eqn. (4.9) is minimum when

$$\beta L = (2m - \frac{1}{2})\pi \,, \tag{4.10}$$

where m is any integer.

$$\min\left|(1-\gamma)^{1/2}e^{-\alpha L/2}e^{j\beta L}+j\sqrt{\rho}\right|=\left|(1-\gamma)^{1/2}e^{-\alpha L/2}-\sqrt{\rho}\right| \qquad (4.11)$$

At critical coupling, the numerator is zero if the coupling ratio is equivalent to the round-trip attenuation factor.

$$\rho_R=(1-\gamma)e^{-\alpha L} \qquad (4.12)$$

Sumetsky et. al. presents a simpler amplitude transfer function for MLR [4].

$$T=\frac{e^{-\alpha L/2}e^{j\beta L}-\sin K}{1-e^{-\alpha L/2}e^{j\beta L}\sin K} \qquad (4.13)$$

Analogous to Eqn. (4.9), the terms $e^{-\alpha L/2}$ and $e^{j\beta L}$ are remained in the new characteristic equation of Eqn. (4.13). The imaginary term $j\sqrt{\rho}$ is replaced with a new coupling parameter $\sin K$ where

$$K=\kappa l \qquad (4.14)$$

κ is the coupling coefficient and l is the coupling length. For every oscillation in the MLR, the circulating wave experiences some attenuation in intensity due to various factors such as non-uniformity in microfiber diameter, material loss, impurity in the ambient of microfiber and bending loss along the microfiber loop. However, these losses can be combined and represented by a round-trip attenuation factor of $e^{-\alpha L/2}$ in Eqn. (4.13) and thus omitting the term $(1-\gamma)^{1/2}$.

The intensity transfer function is obtained by taking the magnitude squared of the amplitude transfer function Eqn. (4.13).

$$|T|^2=\frac{e^{-\alpha L}+\sin^2(K)-2e^{-\alpha L/2}\sin(K)\cos(\beta L)}{1+e^{-\alpha L}\sin^2(K)-2e^{-\alpha L/2}\sin(K)\cos(\beta L)} \qquad (4.15)$$

Both transfer function in Eqn. (4.10) and Eqn. (4.13) are different in terms of parameter values used when curve-fitting the same transmission spectrum. The missing imaginary

terms j in Eqn. (4.13) only contribute to different phase angles in the two transfer functions. Slightly different from the previous transfer function, the resonant condition of Eqn. (4.13) occurs when

$$\beta L = 2m\pi \tag{4.16}$$

where m is any integer. The condition for critical coupling in Eqn. (4.12) can be rewritten as

$$\sin K_C = e^{-\alpha L/2} \tag{4.17}$$

Nonetheless, both transfer functions are capable of providing good representation for any notch filter transmission spectra with high accuracy.

The free spectral range (FSR) is defined as the spacing between two adjacent resonance wavelengths in the transmission spectrum. The expression in Eqn. (4.16) indicates that the phase difference between two resonance wavelengths is a discrete unit of 2π

$$\beta_m L - \beta_n L = 2m\pi - 2n\pi \tag{4.18}$$

where m and n are any distinct integers.

Between two adjacent resonance wavelengths (n = m-1), the phase difference is

$$\beta_m L - \beta_{m-1} L = 2\pi \tag{4.19}$$

Let

$$\beta_m = \frac{2\pi n_{eff}}{\lambda_m} \tag{4.20}$$

where λ_m is the corresponding wavelength and n_{eff} is the effective index.

$$\rightarrow 2\pi = \frac{2\pi n_{eff} L}{\lambda_m} - \frac{2\pi n_{eff} L}{\lambda_{m-1}} \tag{4.21}$$

$$\rightarrow 2\pi = 2\pi n_{eff} L \left(\frac{\lambda_{m-1} - \lambda_m}{\lambda_m \lambda_{m-1}} \right) \tag{4.22}$$

Let $\Delta\lambda = \lambda_{m-1} - \lambda_m$ and $\lambda^2 = \lambda_m \lambda_{m-1}$

$$\rightarrow 2\pi \approx 2\pi n_{eff} L\left(\frac{\Delta\lambda}{\lambda^2}\right) \tag{4.23}$$

$$\rightarrow \text{FSR},\ \Delta\lambda \approx \frac{\lambda^2}{n_{eff} L} \tag{4.24}$$

or

$$\Delta\lambda \approx \frac{\lambda^2}{n_{eff} \pi D} \tag{4.25}$$

where *D* is the diameter of the circular loop.

In addition to the characteristic parameters mentioned earlier, Q-factor and finesse *F* are two important parameters that define the performance of the MLR. The Q-factor is defined as the ratio of resonance wavelength to the bandwidth of the resonance, the full wave at half maximum (FWHM) (Refer Figure 4.4).

$$\text{Q-factor} = \frac{\lambda}{\Delta\lambda} \tag{4.26}$$

The finesse is defined as the FSR of the resonator divided by the $\Delta\lambda$.

$$F = \frac{FSR}{\Delta\lambda} \tag{4.27}$$

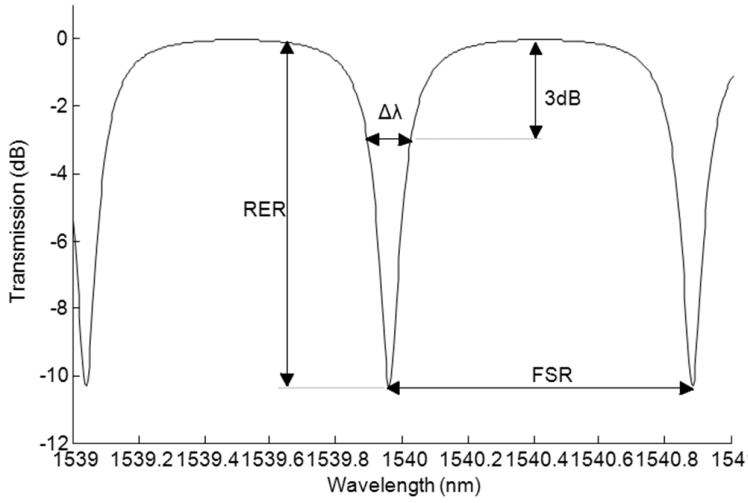

Figure 4.4: Typical transmission spectrum of an MLR. The labels in the graph indicates the terminology used in the thesis.

Due to the narrow bandwidth at the resonance wavelengths, MLR is known as a notch filter [19]. The attenuation at the resonance wavelength can be used to filter out or drop the signal from specific channels in the wavelength division multiplexing (WDM) network by suppressing the signal power. In dense wavelength division multiplexing (DWDM) network, the spacing between two adjacent channels in the network is small therefore notch filter with narrow resonant bandwidth is preferable so that the signals from adjacent channels are unaffected by the attenuation in the drop channel. Based on the relationship in Eqn. (4.27), narrow resonant bandwidth $\Delta\lambda$ can be found in high finesse filter.

4.2.3 Transmission Spectra of MLRs

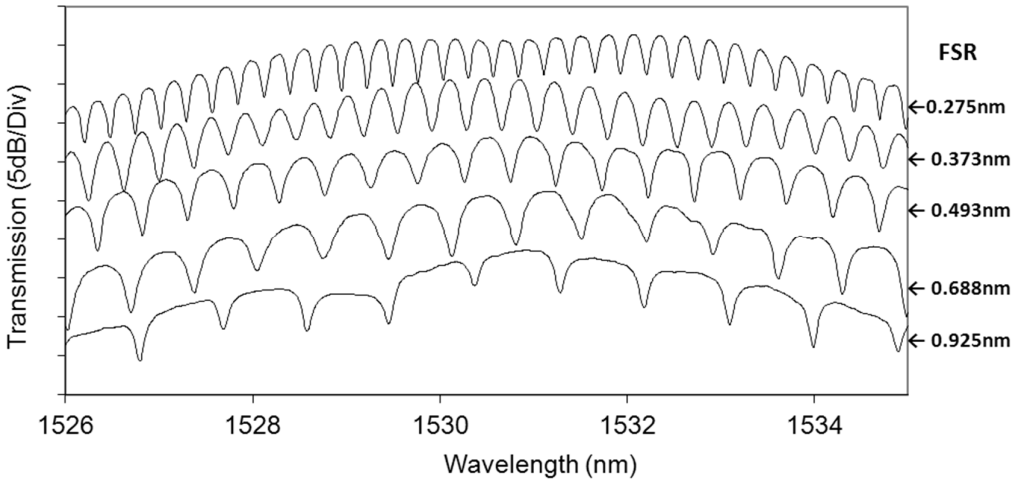

Figure 4.5: Transmission Spectra of an MLR with increasing FSR (from top to bottom).

Figure 4.5 shows the typical transmission spectra of a MLR with different FSRs at 1530 nm region. For better clarity of viewing, the transmission spectra with different FSRs are presented in an increasing order from the top to the the bottom of the figure. The FSR values are varied from 0.275 nm to 0.925 nm. These transmission spectra were recorded from a freestanding MLR in the air, started from a large loop diameter and the diameter is decreasing in step when the two microfiber arms of the MLR are stretched.

Exploiting the van der Waals attraction force between the two microfibers in the coupling region, the resonance condition of the MLR can still be maintained during the stretching of microfiber. In the measurement, the loop diameters are approximately 1.9 mm, 1.4 mm, 1.1 mm, 0.8 mm and 0.6 mm for the FSRs of 0.275 nm, 0.373 nm, 0.493 nm, 0.688 nm and 0.925 nm respectively. These variations of FSR and loop diameter are very consistent with the reciprocal relationship expressed in Eqn. (4.25). The loop diameter of an MLR is restricted by the microfiber elastic force, the smaller is the loop diameter the greater is the elastic force. Thus, it is difficult to keep the microfiber loop in shape when the loop diameter is very small and the MLR loses its resonance condition when the loop opens.

(a)

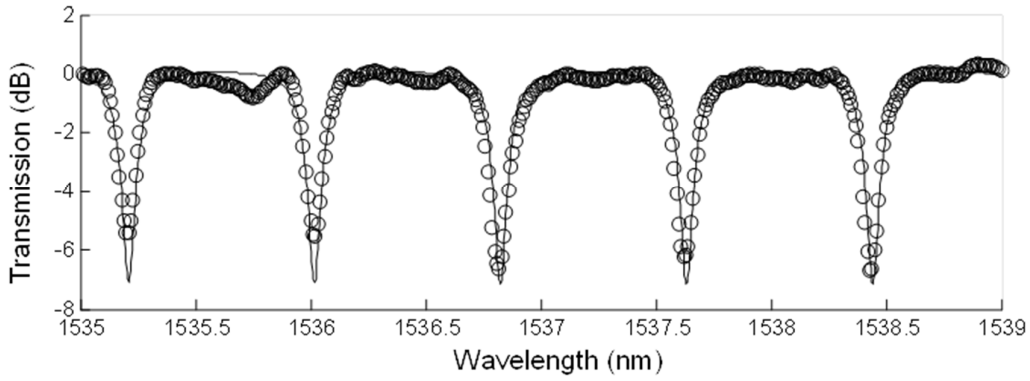

(b)

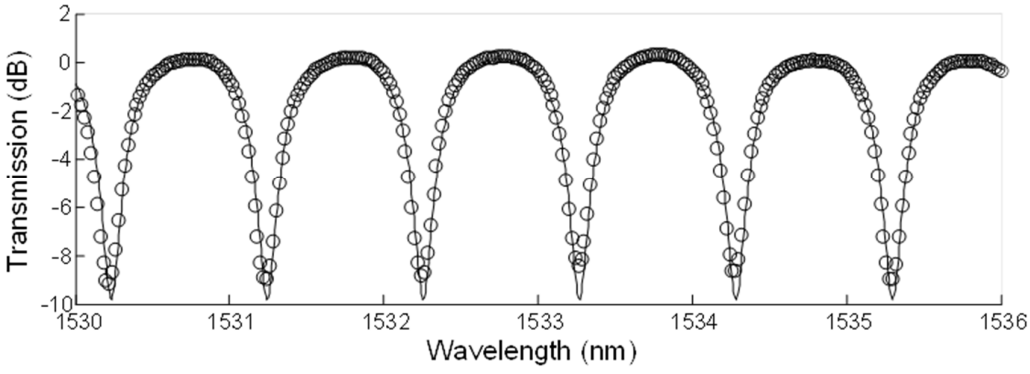

Figure 4.6: The fitting of experimental data (circles) with the characteristic equation (solid line). (a) Q-factor ~18,000 and finesse ~9.5 (b) Q-factor ~5700 and finesse ~3.8

Figures 4.5(a) and 4.5(b) show the fitting of experimental data with the (intensity) analytical model based on characteristic equation in Eqn. (4.15). The best-fit parameters for the transmission spectrum in Figure 4.6(a) are L = 2.03 mm, $e^{-\alpha L/2}$ = 0.8853 and sin$K$ = 0.7354. The measured FSR ~0.805 nm from transmission spectrum in Figure 4.6(a) is in agreement with the calculated FSR ~ 0.807 nm. The bandwidth at the resonance wavelength $\Delta\lambda$ is ~0.085 nm indicates that the Q-factor and finesse of the MLR are 18,000 and ~9.5. The best fit parameter for Figure 4.6(b) are L = 1.61 mm, sin$K$ = 0.5133 and $e^{-\alpha L/2}$ = 0.6961. The measured FSR and $\Delta\lambda$ are ~1.02 nm and ~0.27 nm respectively which indicate the values of Q-factor and finesse are ~5700 and ~3.8. Comparing between these two spectra, it is found that the finesse provides a good representation in weighting the bandwidth between passband and stopband. The higher is the finesse the narrower is the stopband compared with passband.

4.2.4 Polarization Dependent Characteristic

Microfiber based resonator exhibits strong dependence on its input polarization state. Similar characteristic was reported by Caspar et. al. [17] where the RER of the resonator varies with the change of input state of polarization.

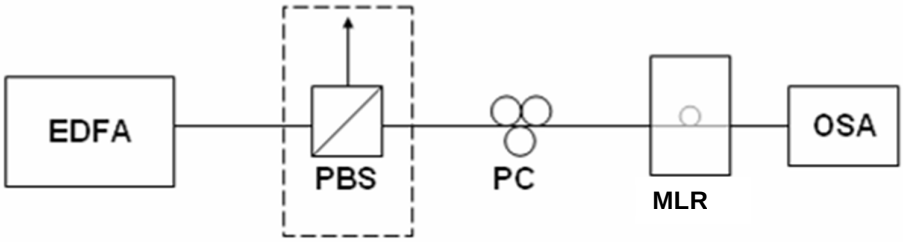

Figure 4.7: Experimental set-up to investigate the polarization dependent characteristic of the MLR [21]. Polarized wideband source from EDFA is acquired with the aid of PBS (Dashed box), an unpolarized wideband source can be obtained by removing PBS from the setup.

In the investigation of polarization state dependent characteristics, a simple experimental setup as shown in the Figure 4.7 is established. Figure 4.7 shows the

experimental setup to investigate the polarization dependent characteristic of the fabricated MLR. An unpolarized amplified spontaneous emission (ASE) source from an Erbium-doped fiber amplifier (EDFA) is linearly polarized by a polarizing beam-splitter (PBS) before it is launched into the fabricated MLR. A polarization controller (PC), which is located in between the source and MLR, is used to control the state of polarization of the light source. The output spectrum from the MLR is characterized by an optical spectrum analyser (OSA). The experiment is also repeated using an unpolarized input wave, which is obtained by removing PBS from the setup for comparison purpose. Figure 4.8 shows the transmission spectra of fabricated MLRs under three different scenarios; (i) without PBS, (ii) with PBS and PC is adjusted to obtain the smallest RER, and (iii) with PBS and PC is adjusted to obtain the highest RER. Figures 4.8(a) and 4.8(b) show the spectra obtained from the MLRs, which were designed to achieve FSR of 0.16 nm and 0.71 nm, respectively. Both transmission spectra of (i) in Figure 4.8 were acquired based on an unpolarized input light and there is a very little change in the resonance condition by the adjustment of PC. In contrast, the resonance condition for the MLR with polarized input light is very sensitive to the PC adjustment as illustrated in spectra (ii) and (iii) of Figure 4.8. The transmission spectra (ii) and (iii) show the smallest and the highest RER respectively, which were achieved by a polarized input light with careful adjustment of PC. As seen in Figure 4.8, it was found that the wavelength of each peak and the FSR remain unchanged regardless of the state of polarization of the input light. The change of the RER as a consequence of polarization state can be explained by the change in coupling condition between microfibers. The coupling condition can be influenced by the material refractive index, microfiber size and distance between the microfibers in the coupling region. The coupling efficiency at the self-touching part of the microfiber can be manipulated by the adjustment of PC which subsequently changes the resonance condition of the MLR.

These results show that the RER of the MLR can be improved by using an optimized polarized input light. This property may be useful in many applications such as multiwavelength laser generation and sensing.

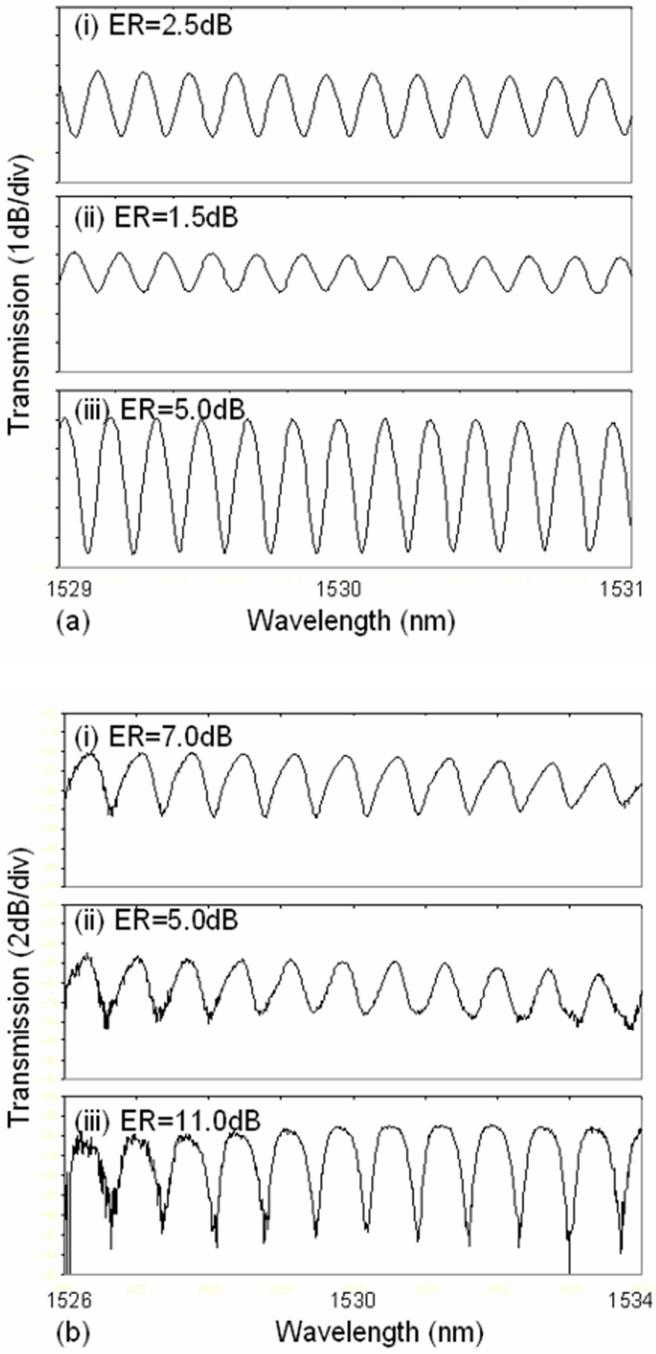

Figure 4.8: The spectra of two MLRs for different input wave SOP. (a) FSR = 0.162 nm at 1530 nm (b) FSR = 0.71 nm at 1530 nm.

4.3 Microfiber Knot Resonator (MKR)

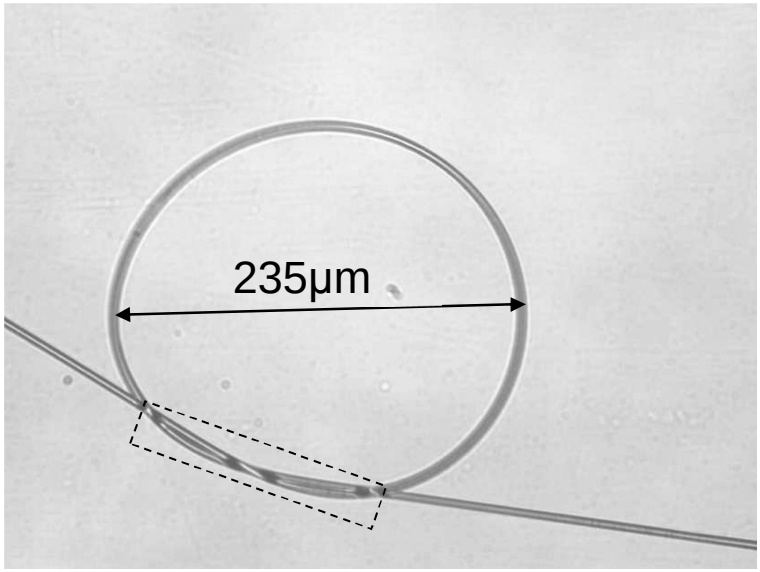

Figure 4.9: Optical microscope image of an MKR

MKR is assembled by cutting a long and uniform tapered fiber into two. One tapered fiber is used for the fabrication of microfiber knot while the other one is used to collect the output power of the MKR by coupling the two tapered fiber ends and guides the output light back to an SMF. The fabrication of microfiber knot can be done by using tweezers. The coupling region of the MKR is enclosed by a dashed box in Figure 4.9 where the two microfibers intertwisted and overlapped in the resonator. In comparison with MLR, MKR does not rely on van der Waals attraction force to maintain the coupling region yet it can achieve stronger coupling due to the rigid intertwisted microfibers structure at the coupling region. The knot structure can withstand strong elastic force of the microfiber and maintain a rigid resonator structure with a more stable resonance condition. Based on the same microfiber diameter, MKR of smaller knot diameter can be easily manufactured than that of MLR. However, MKR suffers a setback in a high insertion loss due to the cut-coil-couple process where the evanescent coupling between output microfiber and collector microfiber contributes a large fraction in the total insertion loss. The microfiber diameter in the range of 1~3 µm

is preferable because thinner microfiber is very fragile and it breaks easily in the fabrication of MKRs. Nonetheless, the operating principle of MKR is identical to MLR as it is based on self-touching configuration thus the same characteristic equation can be used to describe the transmission spectrum.

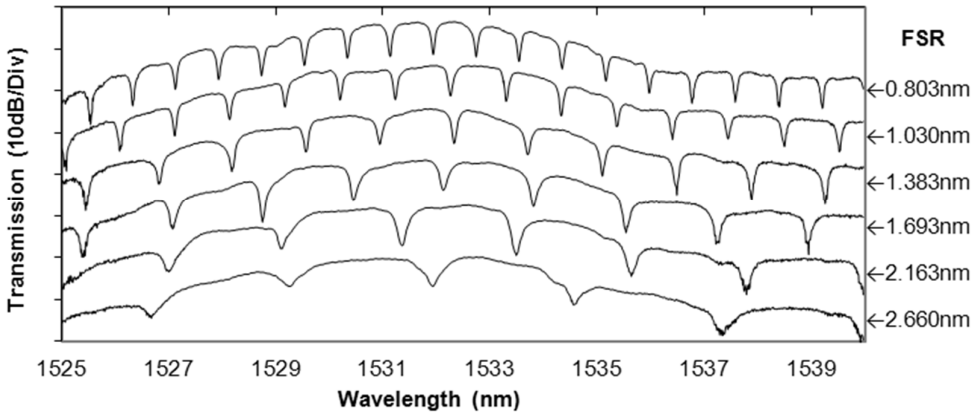

Figure 4.10: Transmission Spectra of an MKR with increasing FSR (from top to bottom)

Figure 4.10 shows transmission spectra of a MKR assembled in the laboratory. At various FSR within the vicinity of 1530 nm, the spectra have a FSR of 0.803 nm, 1.030 nm, 1.383 nm, 1.693 nm, 2.163 nm and 2.660 nm with the corresponding calculated knot diameters of approximately 640 µm, 500 µm, 370 µm, 310 µm, 240 µm and 190 µm respectively.

4.3.1 Resonance Condition of MKR Immersed in Liquids

Recently, microfiber resonators are suggested in numerous applications particularly in the sensing applications [4, 12]. The operating principles of these sensors rely on the characteristics of the resonance, the variation of the position of resonance wavelength and the RER with the sensing parameters, temperature, refractive index and etc. [13, 22]. The resonance condition of a resonator relies on the index contrast between microfiber and its ambient medium, evanescent field strength and distance

between two microfibers in the coupling region. Large evanescent field which can be found in thinner microfibers is one of the solutions to achieving higher coupling in microfiber resonators. The large fraction of light intensity in the evanescent field allows stronger mode interaction between two microfibers and yields high coupling coefficient. Caspar et. al. suggested embedding the microfiber resonator into a medium that has a slightly lower refractive index than that of silica to increase the coupling coefficient. Due to the small index contrast, the microfiber has a larger evanescent field which yields stronger coupling in the resonator [9, 17]. Besides being used as a post-fabrication remedy for improving the resonance condition of the resonator, embedding also offers good protection from the fast aging process and enabling portability for the microfiber devices. Vienne at. el. have reported that when a microfiber resonator is embedded in low-index polymer, the optimal resonance wavelength is down-shifted by ~20% [23]. However, there is very few literatures provide mathematically analysis on the effect of embedding in low index contrast medium to the resonance condition of the resonator. In order to achieve a better understanding, an experiment on an MKR immersed in liquid solutions was carried out. MKR was used in the experiment due to its rigid knot structure and strong interfiber coupling. The knot structure and resonance condition could be easily maintained during the immersing process.

Unlike MLR that exploits van der Waals attractive force to maintain the structure of the loop, MKR has a more rigid knot structure with interfiber twisted coupling. Nonetheless, both MLR and MKR share the same optical properties; the same transfer function can be used to describe both structures. Fabrication of an MKR started with fiber tapering using heat and pull technique. After a single-mode biconical tapered fiber was drawn, it was cut at one third part of the waist which the longer section of tapered fiber was used for the fabrication of knot by using tweezers. Then the second section was used as collector fiber by evanescent coupling [24] with the output port of

the knot resonator. Immediately after that, the transmission spectrum of the freestanding MKR in the air was recorded by an OSA. After that, the MKR was embedded in propan-2-ol solution that has a refractive index (RI) of 1.37. First, the MKR was slowly laid horizontally on an earlier prepared flat platform deposited with a thin layer of propan-2-ol. Using a micropipette, a small volume of propan-2-ol solution was dropped onto the MKR and had it entirely immersed in the solution. The structure of the microfiber knot was intact and the resonance was maintained. This is the crucial part that distinguishes MKR from MLR. It is very difficult to maintain the loop structure and resonance of MLR when immersed in the liquid.

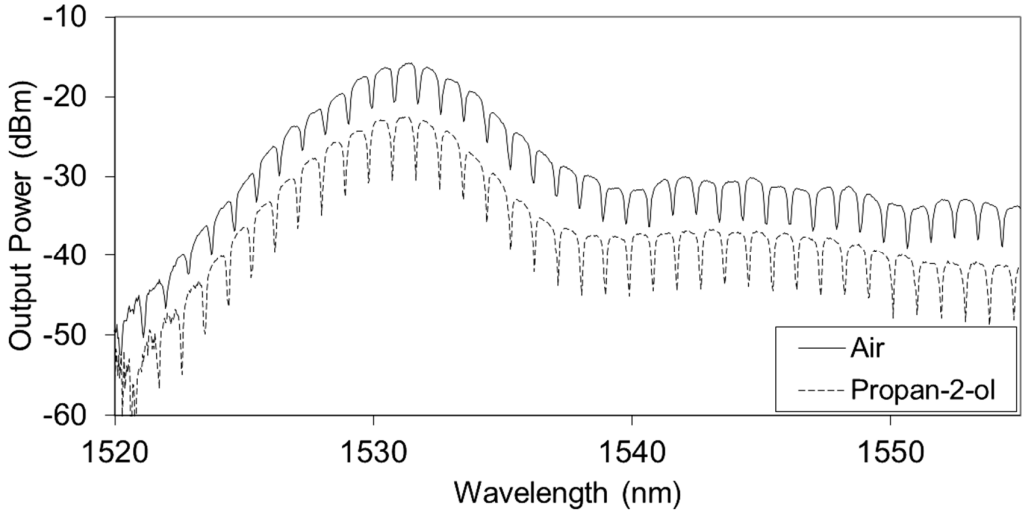

Figure 4.11: The transmission spectra of MKR in the air (solid) and propan-2-ol solution (dashed)

Figure 4.11 shows the overlaid transmission spectra of the MKR in the air (solid line) and solution (dashed line). Refering to the peak powers of both spectra, it is easy to determine that the MKR had suffered an additional ~7 dB excess loss after it was immersed in the solution. The drop in coupling efficiency at the evanescent coupling between MKR output microfiber and collector microfiber constituted a large fraction in this excess loss. On the other hand, the RER of the MKR had improved from ~5 dB to ~8 dB.

(a)

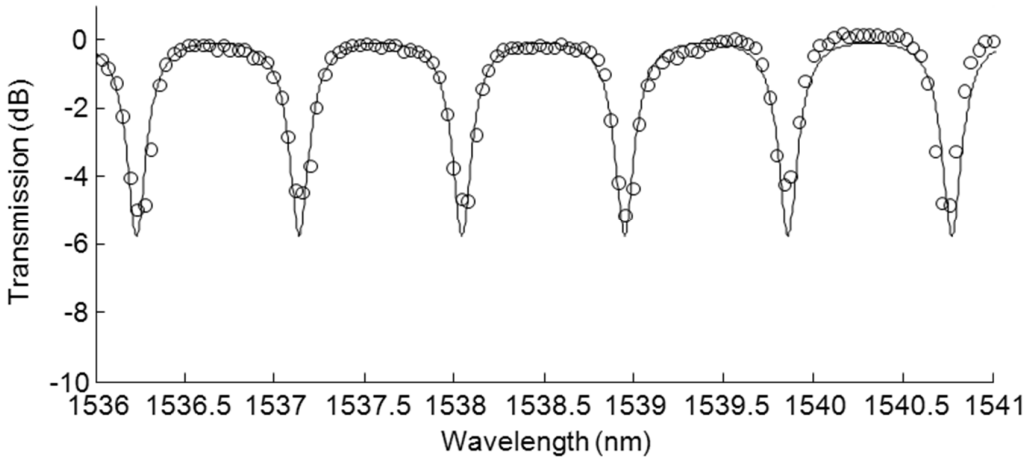

(b)

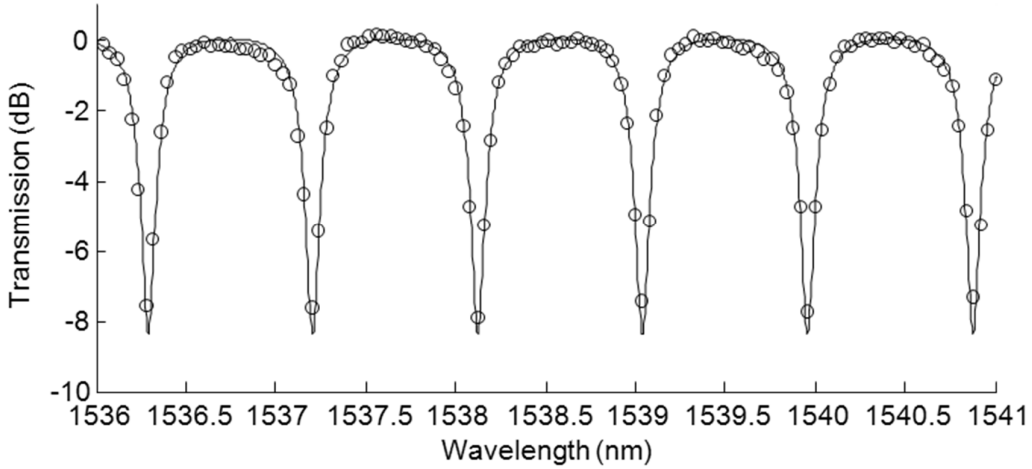

Figure 4.12: The offset experimental data (circles) with its best fit curve (solid line) (a) air, RI ~1.00 (b) propan-2-ol, RI ~1.37.

In the analysis of resonance characteristics, coupling parameters, $\sin\kappa\ell$ and round-trip attenuation factor, $e^{-\alpha L/2}$ of MKR can be extracted from the best-fit curves (solid lines) for the offset experimental data (circles) in Figure 4.12 based on the transfer function in (4.13). Figures 4.11(a) and 4.11(b) show the offset transmission spectra. In the air, the best fit parameters for the transmission spectrum are $\sin\kappa\ell$ = 0.6207 and $e^{-\alpha L/2}$ = 0.8547 as shown in Figure 4.12(a). When the MKR was immersed in

the propan-2-ol solution, the best fit parameters are $\sin\kappa\ell = 0.6762$ and $e^{-\alpha L/2} = 0.8361$ as shown in Figure 4.12(b). The reduction in round-trip attenuation factor can be attributed to the small index contrast between microfiber and ambient medium when immersed in the solution, the bending loss at the microfiber knot is higher. The output - collector coupling loss is excluded from this analysis as it only affects the total output power (position in the vertical axis) and it can be eliminated in the offset spectrum. Based on Eqn. (4.13), the resonance state of the resonator can be determined from the following expression

$$\delta = \left| \frac{e^{-\alpha L/2} - \sin K}{1 - e^{-\alpha L/2} \sin K} \right| \tag{4.28}$$

Smaller value of δ indicates that the state of resonance is closer to the critical coupling condition and it yields larger RER. In fact, RER can be estimated by

$$RER \sim 20\log_{10}\delta \tag{4.29}$$

In the comparison between the two spectra, the spectrum in Figure 4.12(b) has higher coupling and smaller round-trip attenuation factor which give smaller value in $\delta = 0.3679$ if compared with $\delta = 0.5060$ obtained from the spectrum in Figure 4.12(a). This explains the larger RER of the spectrum in Figure 4.12(b). However, it is possible that the large increment in the coupling coefficient κ may have forwarded the phase $\kappa\ell$ to the next quarter cycle of the sinusoidal function of $\sin\kappa\ell$ and resulting the lower coupling value. The next experimental data may provide an example for such self-defeating scenario.

(a)

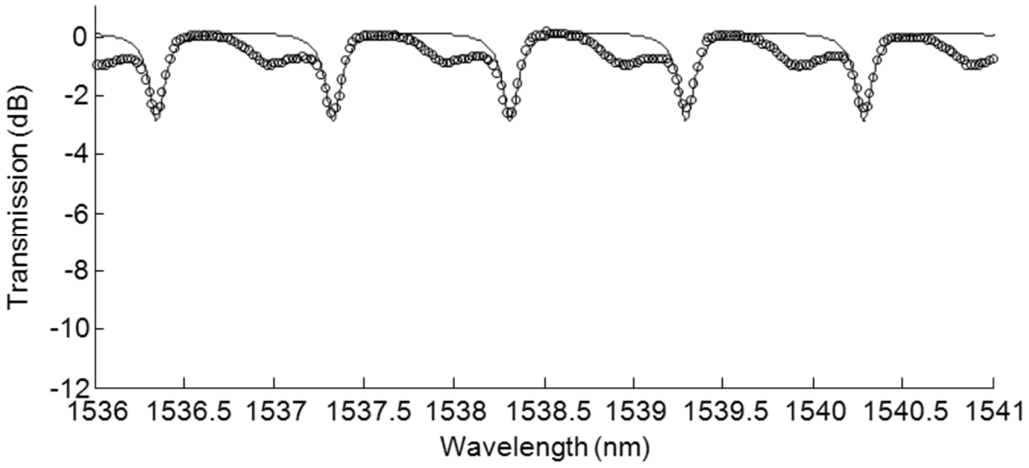

(b)

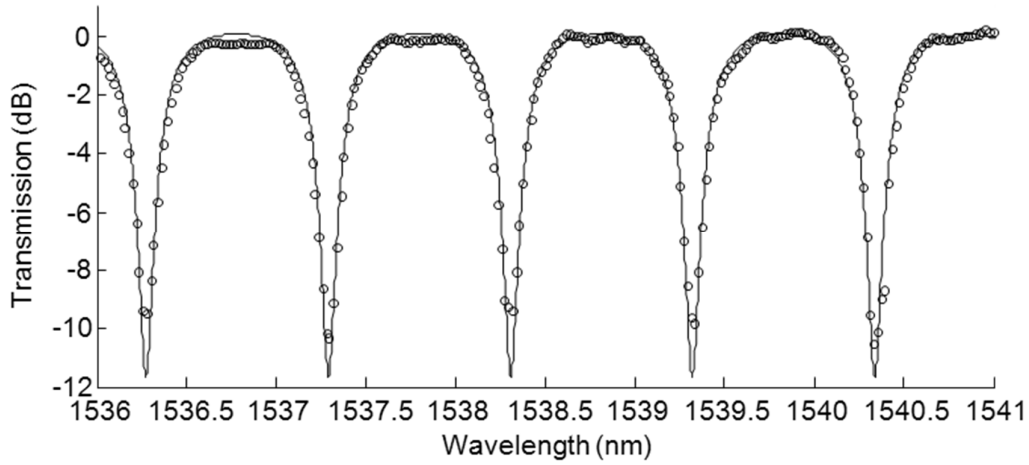

Figure 4.13: The experimental data (circles) with its best fit curves(solid lines) in different medium(a) air, RI ~1.00 (b) low-index resin, RI ~1.36.

The transmission spectra of another MKR in the air and low-index UV-curable resin (UV-Opti-clad 1.36RCM from OPTEM Inc.) with an RI of ~1.36 are also investigated and the results are shown in Figures 4.12(a) and 4.12(b) respectively. The coupling parameter, $\sin\kappa\ell$ had dropped from 0.7132 to 0.6247 when it was immersed in the resin. On the other hand, the round-trip attenuation factor, $e^{-\alpha L/2}$ suffers greater fall from 0.9432 to 0.7538. In spite of that, the RER had increased from ~2 dB to ~10 dB.

This is in agreement with the decreasing value of δ from 0.7027 to 0.2440 and the state of resonance is closer to critical coupling condition.

Immersing MKR in a near-index medium do not always promise an improvement in the resonance condition or RER. There is a possibility that the changes in round-trip attenuation factor and coupling parameter yield larger value of δ and decreases the RER. Figure 4.14 gives an example for this scenario. The best-fit parameter for the experimental data in the air (solid) are $\sin\kappa\ell$ = 0.6235 and $e^{-\alpha L/2}$ = 0.8145 respectively. After the MKR is immersed in the water (dashed), the values have varied to $\sin\kappa\ell$ = 0.7833 and $e^{-\alpha L/2}$ = 0.9339. In the air, the low value of round-trip attenuation factor can be attributed to the large amount of deposited dust on the microfiber surface which was introduced from the tweezers during the fabrication of microfiber knot. After it was immersed in the water, some portion of the dust might have been 'washed' away and that increases the round-trip attenuation factor. The value of δ has decreased from 0.3881 to 0.5609 which is an indication of the resonance state deviates from critical coupling.

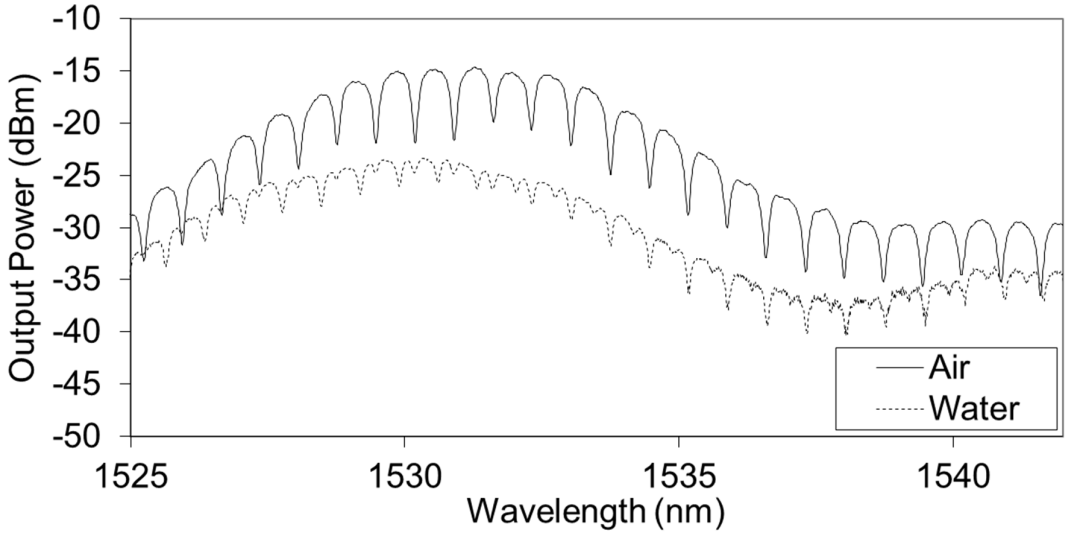

Figure 4.14: Example of an MKR with decreased RER after it is immersed in the water (RI ~1.33).

In conclusion, liquid solutions of different RIs were used to investigate the influence of different index-contrasts to the resonance characteristics of the MKR. It was observed that the change in RER is significant in the moment when the MKRs were immersed in the liquid solutions from air. However, there was no significant trend observed in the experiment that the effect of different RI of solution. It is believed that the index contrasts induced by these three liquids are within a narrow range from 0.07 to 0.11 and the differences among them are too small to make significant impact on the characteristics of the MKR. On the other hand, we believe that that the microfiber waist diameter and orientation of the microfibers in the coupling region have an important relationship with the resonance of MKR. More investigations pertaining to those parameters are needed. FSR is observed to be unchanged with the surrounding RI.

4.3.2 Thermally Induced Characteristic

Microfiber based devices are very sensitive to variation of ambient temperature due to the strong dependence of the microfiber dimension and refractive index on temperature. In a thermally unstable environment, these devices may experience thermal drift in the transmission spectrum and fluctuation in the transmission power. However, this problem can be alleviated by the placing the devices in a temperature controlled housing [25]. Sumetsky et. al. demonstrated an ultrafast sensor using MKR to measure gas temperature. Taking advantage of the close contact between the MKR to air, the change in gas temperature in the ambient of MKR can be determined from the transmission power at the resonance wavelengths within a short response time of several microseconds [4].

Besides, the positions of resonance wavelengths are found to be sensitive to temperature change. The spectral shift of an MKR can be expressed in a linear function of temperature. The property enables temperature measurement based resonance

wavelength shift with higher accuracy [13, 26]. In this section, the effect of ambient temperature on the transmission spectrum of the MKR is theoretically analysed and experimentally demonstrated.

Theory

MKRs exhibit the similar optical properties with MLRs. The free spectral range of MKR takes in the form of Eqn. (4.24). Based on this equation, the variations in effective index n_{eff} and round-trip length L may lead to transmission spectral shift and their relationship can be expressed as

$$\frac{\Delta\lambda_{res}}{\lambda_{res}} = \left(\frac{\Delta n_{eff}}{n_{eff}} + \frac{\Delta L}{L} \right)_{Temp.} \tag{4.30}$$

In relation with temperature, both terms on the right hand side of Eqn. (4.30) can be well expressed as two linear thermal equations with thermal-optic coefficient (TOC) and thermal expansion coefficient (TEC) respectively [13]. With this interpretation, Eqn. (4.30) can be rewritten as

$$\frac{\Delta\lambda_{res}}{\lambda_{res}} = (\alpha_{TOC} + \alpha_{TEC})\Delta T \tag{4.31}$$

Experimental Results

Figure 4.15(a) shows the transmission spectra of MKR at temperatures of 30°C, 35°C and 40°C. The spectral shift is approximately 26 pm for every temperature increment of 5°C and the linearity between wavelength shift and temperature change can be seen from the linear fitting of experimental data in Figure 4.15(b).

(a)

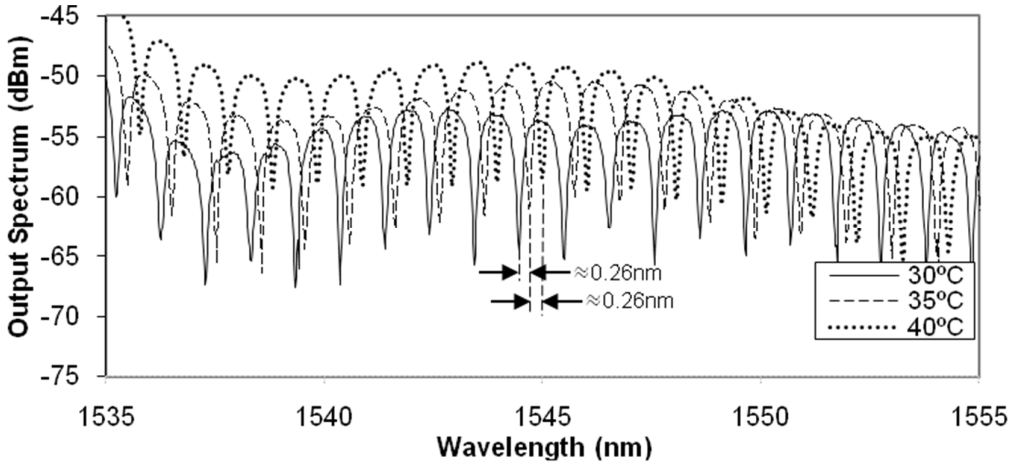

(b)

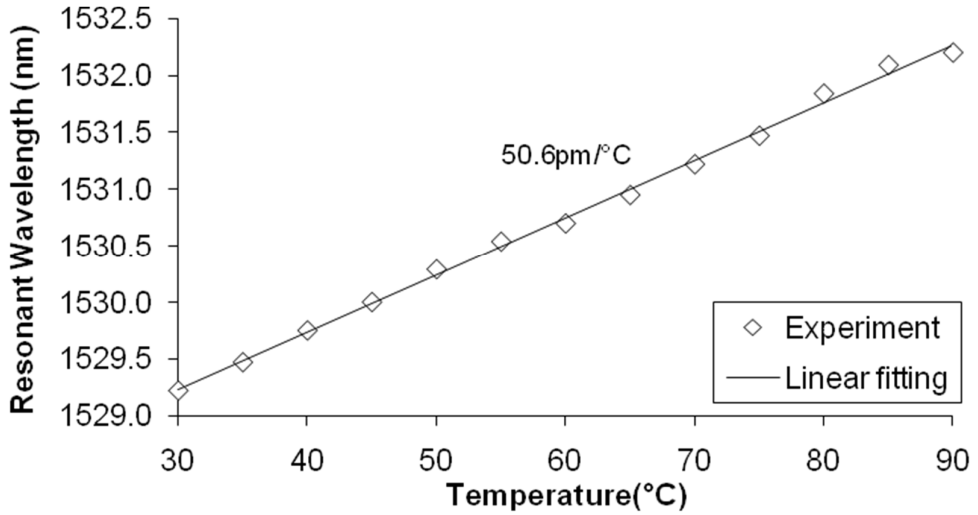

Figure 4.15: (a) The output spectra of an MKR at temperature of 30°C(solid), 35°C(dashed) and 40°C (dotted) (b) The temperature response of the MKR has spectral sensitivity of 50.6 pm/°C.

This characteristic has opened up new possibilities for temperature sensing and spectral control based on temperature manipulation. It provides a solution for stabilizing the spectrum of the device which often affected by the thermal drift. Dynamic spectral shift in optical filter can be realized by exploiting this characteristic. In addition, the

insusceptibility of fiber-optic components to electrical noise has made these devices very attractive for many industrial sensing applications.

4.4 Microfiber Mach-Zehnder Interferometer (MMZI)

Interest in Mach–Zehnder interferometers (MZI) is rising due to their simple structure and many applications in photonics devices. For instance, MZI based sensors that are highly sensitive to the refractive index change in the surrounding medium have been demonstrated [27]. A thermo-optic switch based on MZIs has been proposed aand demonstrated [28]. Add–drop filters constructed from cascaded MZIs have been demonstrated and found useful for optical communications [29]. Most MZIs are developed in planar waveguide but the fabrication cost is high and they often suffer from large connection-losses with fibers. The recent research on low-loss micro- and nanofibers has accelerated the development of a number of microphotonic devices such as resonators, couplers, sensors and loop interferometers to compete with planar waveguide [11, 12, 30]. A theoretical investigation has suggested that with a hybrid MZI and microknot microfiber structure, an ultra-high Q-factor of 1.8×10^5 with a high RER within a very large wavelength span range can be achieved [31].

In an earlier work, Li and Tong [16] first demonstrated the formation of the microfiber-based MZI (MMZI) with two microfibers. Compared with planar waveguide based device, the MMZI exhibits superior features in relation to compact size, simple fabrication and integration with the fiberized components. In this paper, we present the construction of MMZIs from a single microfiber fabricated using a standard single mode fiber (SMF) in conjunction with a flame brushing technique. The spectral responses of the fabricated devices are investigated for various path length differences obtained from in-situ micro-manipulating. The effect of volatility of the MMZI in the air is also investigated.

4.4.1 Fabrication

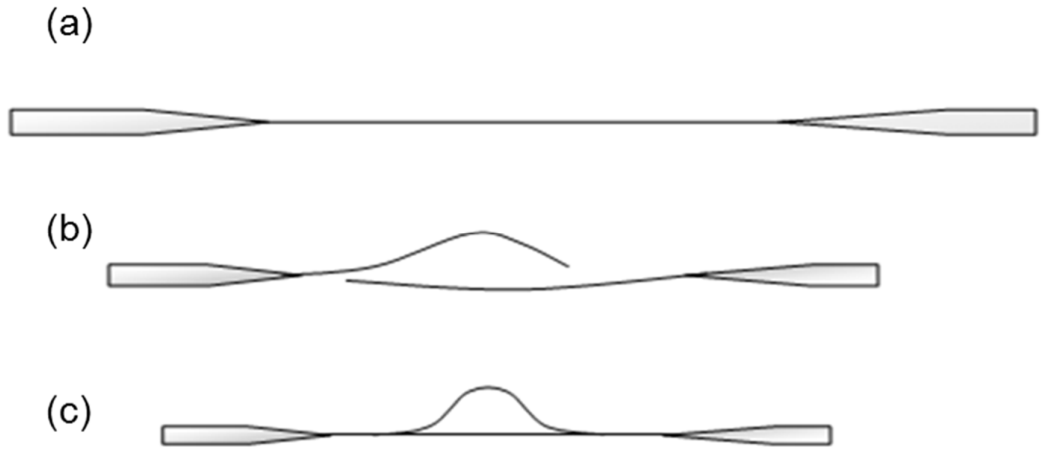

Figure 4.16: Schematics (a)-(c) provide an illustration of the fabrication procedure for an MMZI

In the manufacture of MMZI, a biconical tapered fiber with a uniform waist length of 30-50mm long is first fabricated as illustrated in Figure 4.16(a). Then the taper waist is separated by cutting it into two microfibers. By using tweezers, the microfibers are manipulated in such a way that the end bit of each microfiber touches the beginning bit of the other microfiber as illustrated in Figure 4.16(b). The touching between two microfibers should form two coupling regions in the MMZI. In order to produce interference fringes at the output of the interferometer, the microfiber arms that link between the two coupling regions should be of unequal length. At the end of the fabrication, the end product of MMZI should look like the one in Figure 4.16(c).

4.4.2 Theory

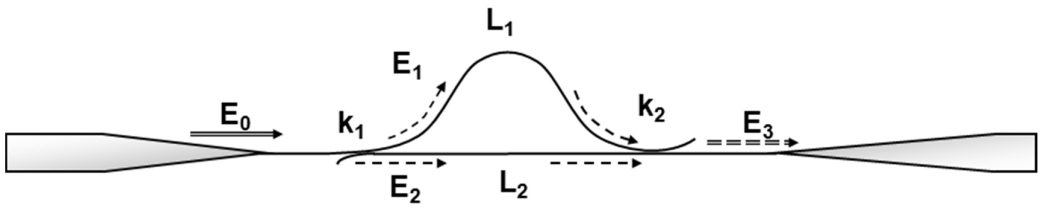

Figure 4.17: Schematic illustration of an MMZI.

Figure 4.17 shows the schematic of an MMZI which comprises of two tapered fibers. The one on the left is the transmitting fiber while the other one being the collecting fiber. First, the wave E_0 comes from the SMF on the left hand-side splits into two waves, E_1 and E_2 at the first coupling region of the interferometer. The complex expressions below describe splitting of energy at the first coupling region. Assuming a lossless model, we have

$$E_1 = (1-k_1)^{1/2} E_0 \tag{4.32}$$

$$E_2 = jk_1^{1/2} E_0 \tag{4.33}$$

where k_1 denotes the intensity coupling ratio in the first coupling region. After propagating through the respective microfiber arm, waves E_1 and E_2 experience phase increments of βL_1 and βL_2 respectively before they recombine at the second coupling region and produce an output wave E_3.

$$E_3 = jk_2^{1/2} E_1 e^{j\beta L_1} + (1-k_2)^{1/2} E_2 e^{j\beta L_2} \tag{4.34}$$

where k_2 is the intensity coupling ratio in the second coupling region.

Substitute Eqns. (4.32) and (4.33) into Eqn. (4.34),

$$T = \frac{E_3}{E_0} = j\left[k_2^{1/2}(1-k_1)^{1/2} e^{j\beta L_1} + k_1^{1/2}(1-k_2)^{1/2} e^{j\beta L_2} \right] \tag{4.35}$$

Let $\Delta L = L_1 - L_2$ (4.36)

$$T = j\left[k_2^{1/2}(1-k_1)^{1/2} e^{j\beta \Delta L} + k_1^{1/2}(1-k_2)^{1/2} \right] e^{j\beta L_2} \tag{4.37}$$

The intensity transfer function can written as

$$|T|^2 = k_2(1-k_1) + k_2(1-k_2) + 2k_1^{1/2} k_2^{1/2} (1-k_1)^{1/2} (1-k_2)^{1/2} \cos \beta \Delta L \tag{4.38}$$

or in a simpler form

$$|T|^2 = a + b \cos \beta \Delta L \tag{4.39}$$

where a and b are arbitrary constants and $a, b > 0$. The wavelength spacing is defined as the spacing between two adjacent minima or maxima in the transmission spectrum which is given by the expression below

$$\Delta\lambda = \frac{\lambda^2}{n_{eff}\Delta L} \tag{4.40}$$

where λ is the central wavelength and n_{eff} is the effective index of the microfiber.

4.4.3 Transmission Spectra of an MMZI

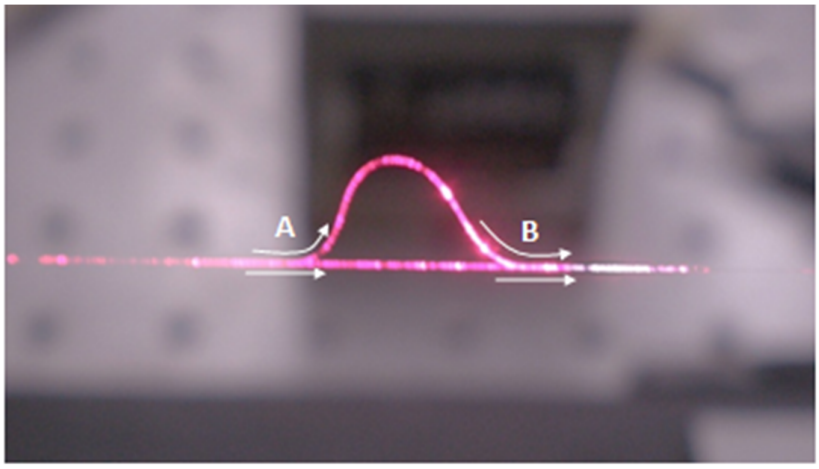

Figure 4.18: Image of an MMZI injected with visible red laser. The arrows indicate the propagation directions of the waves.

Figure 4.18 shows the optical microscope image of the constructed MMZI using a microfiber with diameter of 2.2 μm. For clearer visibility, it is illuminated with visible red laser from the transmitting fiber, as shown on the left side of Figure 4.18. The notations A and B in the image indicate the locations of the coupling regions of the MMZI. At the coupling region A, the incoming wave is split into two waves when a broadband light is launched into the MMZI through an un-tapered input SMF. One of them enters the straight arm while the other enters the bent arm which has a longer optical path length. After propagating through the respective microfiber arms, both waves recombine in the coupling region B before it is guided to an OSA through the output fiber. The spectral response of the MMZI is shown in Figure 4.19, in which a

clear interference with an RER and FSR of about 7 dB and 0.2 nm, respectively is observed within a wavelength region of 1541 nm.

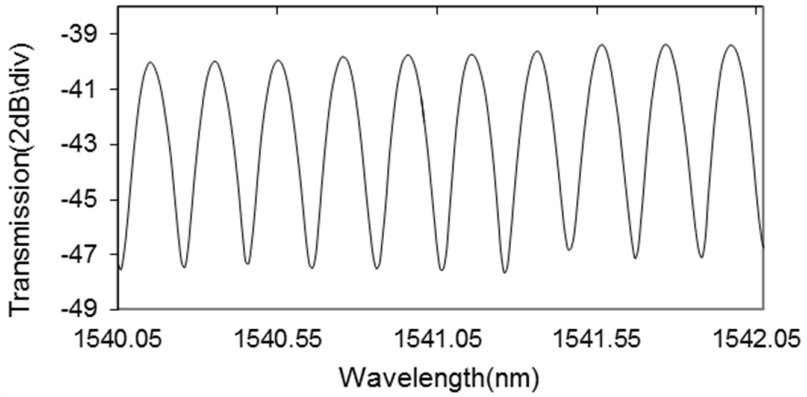

Figure 4.19: Transmission spectrum of an MMZI with RER 7 dB and 0.2 nm FSR

Since the couplers in the MMZI are formed by evanescent coupling and maintained by van der Waals attraction force, the path length difference can be easily changed by applying a pressure to move the contact points using micromanipulation. The small change in physical parameters changes the coupling coefficient, which in turn changes the path length. Figure 4.20 shows the spectral response of the MMZI at various path length difference, which provides tuning of wavelength spacing (WLS) from 0.14 nm to 0.75 nm within the vinicity of 1530 nm. This demonstrates the flexibility of path length tuning (or equivalently, the free spectral range) of this type of MMZI. The path length difference between the straight arm and the longer bend arm generates an optical phase shift due to the delay from the light propagating in the bend arm and thus producing an interference fringes. Different from the transmission spectrum of microfiber loop and knot resonators, the interference fringes in the transmission spectrum of MMZI have the characteristic of a sinusoidal function. This can be observed from the equal bandwidth of the stopband and passband if displayed in a linear scale graph. Figure 4.21 gives an example for case of WLS 0.66 nm of experimental data fit with the theoretical model given by Eqn. (4.39) . The parameters

for the best-fit curve are obtained as ΔL = 2.23 mm, a = 0.518 and b = 0.482. The highest RER measured from the transmission spectrum is as high as ~14 dB. In relation to the interference fringes, high RER is given by the strong destructive and constructive interferences in the interferometer when the wave intensities in both arms are equal. Refering to Eqn. (4.38), this balanced interferometry can be achieved when both the coupling ratios k_1 and k_2 are equal to 0.5.

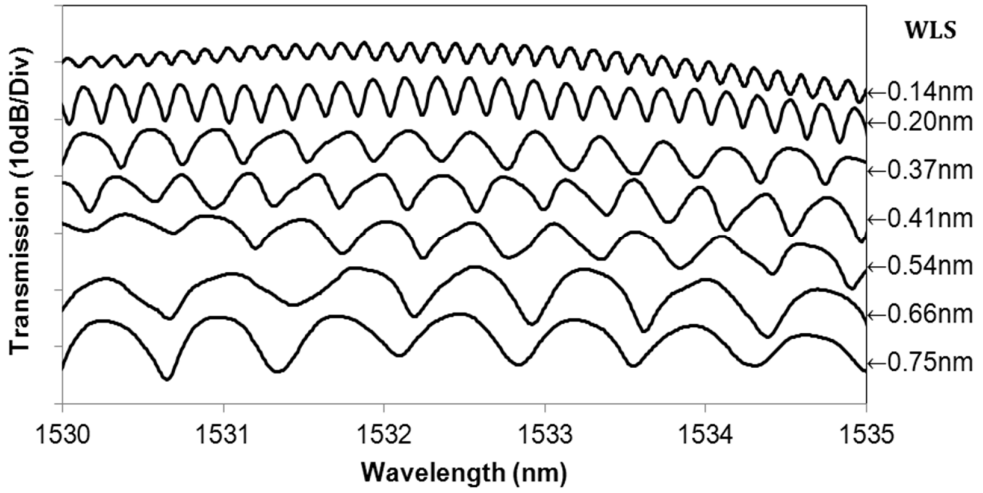

Figure 4.20: Transmission Spectra of an MMZI with increasing wavelength spacing

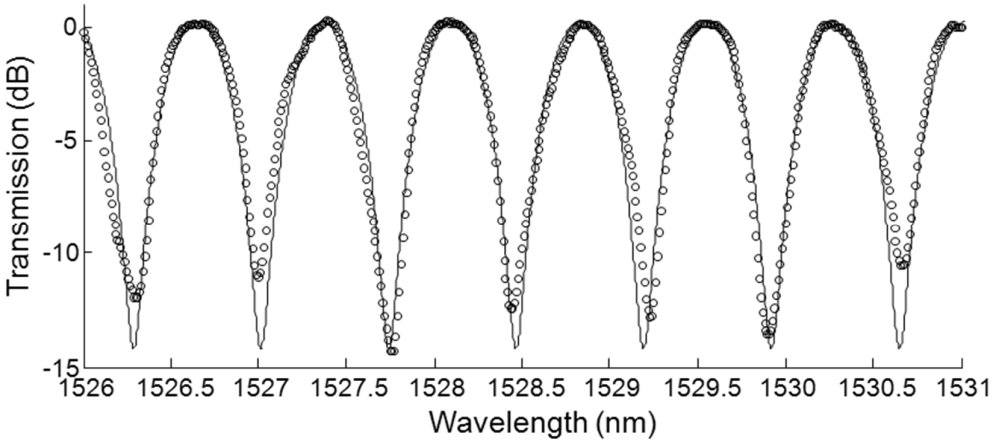

Figure 4.21: The experimental data and its best-fit curve based on the values of ΔL = 2.23 mm, a = 0.518 and b = 0.482.

In the air, the performance of the MMZI is greatly affected by the air-turbulence. Due to the movement of air, the bent arm of the interferometer tends to sway furiously

in the air and the couplings between microfibers in the MMZI are affected. Figure 4.22 illustrates how air-turbulence affects the orientation of the bent arm in the MMZI. The air-turbulence varies the stress and changes the coupling coefficient and path length difference. As a consequence, the interferometer produces volatile or unperdictable output transmission as shown in Figure 4.23. The six spectra in Figure 4.23 are the output spectra from three distinct MMZIs. For the purpose of comparison, the spectra are arranged in the following manner. The spectra in each row are acquired from the same MMZI. The three spectra in the left column that are labeled with (i) are output spectra with highest recorded RER in the experiment while the other three spectra in the right that are labeled with (ii) are the output spectra with lowest recorded RER. Nonetheless, the wavelength spacing is unaffected by the unrest. Embedding the MMZI in low-index resin may address this problem however it is a challenge to maintain the interferometrical condition of the structure during the process.

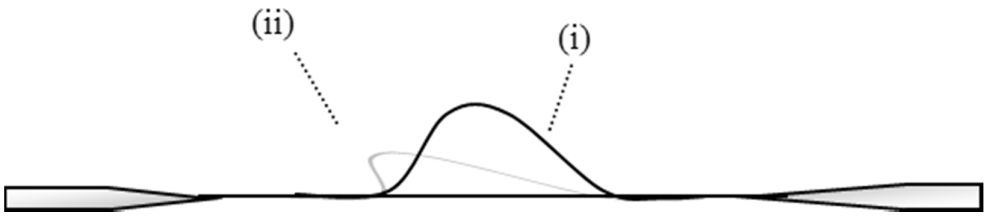

Figure 4.22: Schematic illustration of an MMZI sways the air due to air-turbulence. (i) Bent arm stands vertically on top of the straight arm (ii) Bent arm lays in a horizontal plane with the straight arm.

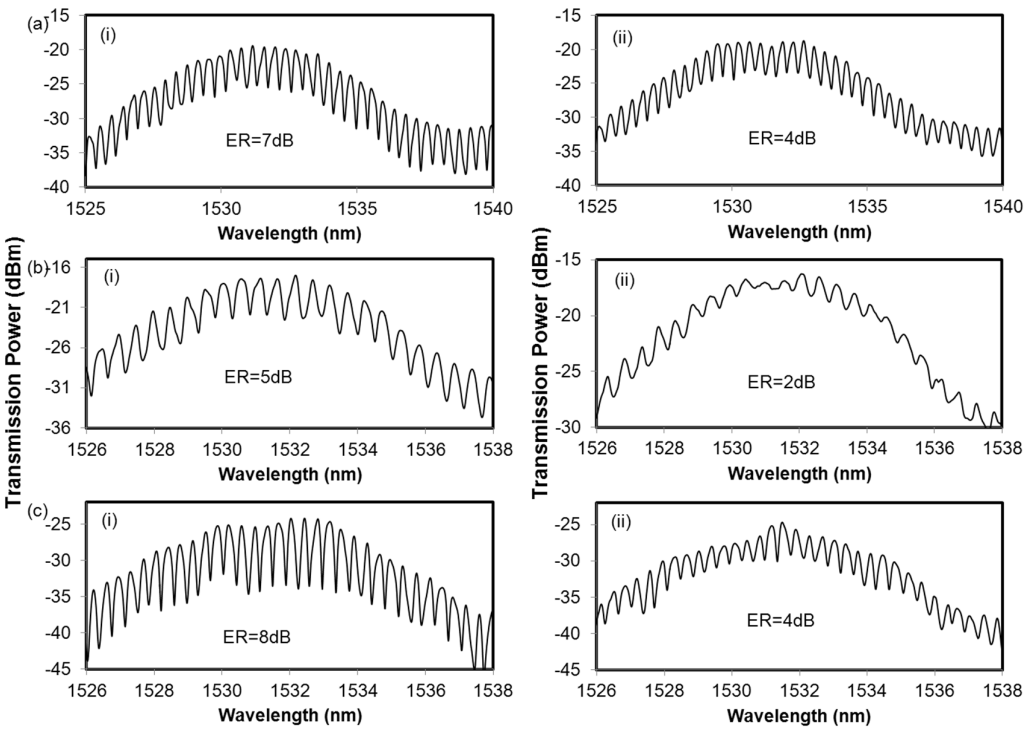

Figure 4.23: Spectra (a)–(c) show three sets of transmission spectra based on three different MMZIs. Spectra (i) and (ii) from each set show the transmissions with the highest and the lowest recorded RERs respectively.

4.5 Summary

Three microfiber based devices have been reviewed in this chapter namely MLR, MKR and MMZI. In the first section, the fabrication of MLR is introduced. MLR is assembled from a single mode microfiber by coiling it into a loop. A closed optical path within the loop is established when the two microfibers are put in close contact with each other and form an evanescent coupling. Then, the theoretical model of the self-touching microfiber loop resonator is presented. In the second part of the chapter, the fabrication and characteristics of MKR are presented. Similar to MLR, MKR shares the similar transmission characteristics and the same theoretical model for the MLR can be applied to MKR. However, MKR outperforms MLR in several aspects for instance MKR has more stable and stronger coupling due to its small spacing between the two coupling microfibers in the coupling region. In addition, the structure of MKR is more rigid and robust with the interfiber twisted coupling in the resonator. Nonetheless,

MKRs suffer a setback in higher insertion loss if compared with MLRs because of the cut-coil-couple process in the fabrication. The evanescent coupling between output microfiber and collector microfiber contributes a large fraction in the total insertion loss. When MKR is embedded into a medium of different refractive index, the coupling in the MKR varies and it alters the resonance state of the resonator. By curving the experimental data for transmission spectra with the theoretical model, the coupling coefficient and round-trip attenuation factor of the MKR can be extracted from the best-fit curve. The results indicate that the state of resonance of an embedded MKR has been altered and it is closer to critical coupling condition. Besides, microfiber based resonators exhibit an interesting polarization dependent characteristic in the investigation. The coupling coefficient in the resonator is dependent on input state of polarization and it can be manipulated by using a PBS and a PC. In relation with the coupling, the RER of transmission spectrum can be varied by tuning the PC. In the experiment, the variation of RER between 5 dB and 11 dB was observed. As discussed in many literatures, the refractive index and dimension of silica microfiber have a strong dependence on temperature. The RER and resonance wavelength can be expressed in functions of temperature. In order to gain insight into this characteristic, an investigation was conducted to study temperature response of an MKR. Both theoretical analysis and experimental result indicate that the spectral shift in the transmission of MKR is linearly proportional to the increment of temperature. This characteristic can be exploited in many applications particular in sector of industrial sensors. More exploration on the applications for this characteristic will be reviewed in the next chapter. In the third part of the chapter, the fabrication of MMZI based on microfiber is demonstrated. Besides, the theoretical model and experimental result are also presented and discussed. In the air, the performance of a freestanding MMZI is affected by the air-turbulence. The transmission spectrum is thus volatile in an unprotected environment.

References

[1] X. Guo, Y. Li, X. Jiang, and L. Tong, "Demonstration of critical coupling in microfiber loops wrapped around a copper rod," *Applied Physics Letters,* vol. 91, no. 7, pp. 073512-3, 2007.

[2] S. W. Harun, K. S. Lim, A. A. Jasim, and H. Ahmad, "Dual wavelength erbium-doped fiber laser using a tapered fiber," *Journal of Modern Optics,* vol. 57, no. 21, pp. 2111 - 2113, 2010.

[3] C. Hou, Y. Wu, X. Zeng, S. Zhao, Q. Zhou, and G. Yang, "Novel high sensitivity accelerometer based on a microfiber loop resonator," *Optical Engineering,* vol. 49, no. 1, pp. 014402-6, 2010.

[4] M. Sumetsky, Y. Dulashko, J. M. Fini, A. Hale, and D. J. DiGiovanni, "The microfiber loop resonator: theory, experiment, and application," *Lightwave Technology, Journal of,* vol. 24, no. 1, pp. 242-250, 2006.

[5] S. Harun, K. Lim, A. Jasim, and H. Ahmad, "Fabrication of tapered fiber based ring resonator," *Laser Physics,* vol. 20, no. 7, pp. 1629-1631, 2010.

[6] M. Sumetsky, Y. Dulashko, J. M. Fini, and A. Hale, "Optical microfiber loop resonator," *Applied Physics Letters,* vol. 86, no. 16, pp. 161108-161108-3, 2005.

[7] M. Sumetsky, "Basic Elements for Microfiber Photonics: Micro/Nanofibers and Microfiber Coil Resonators," *J. Lightwave Technol.,* vol. 26, no. 1, pp. 21-27, 2008.

[8] M. Sumetsky, Y. Dulashko, and S. Ghalmi, "Fabrication of miniature optical fiber and microfiber coils," *Optics and Lasers in Engineering,* vol. 48, no. 3, pp. 272-275, 2010.

[9] F. Xu and G. Brambilla, "Embedding optical microfiber coil resonators in Teflon," *Opt. Lett.,* vol. 32, no. 15, pp. 2164-2166, 2007.

[10] F. Xu, P. Horak, and G. Brambilla, "Optical microfiber coil resonator refractometric sensor," *Opt. Express,* vol. 15, no. 12, pp. 7888-7893, 2007.

[11] X. Jiang, L. Tong, G. Vienne, X. Guo, A. Tsao, Q. Yang, and D. Yang, "Demonstration of optical microfiber knot resonators," *Applied Physics Letters,* vol. 88, no. 22, pp. 223501-223501-3, 2006.

[12] K. S. Lim, S. W. Harun, S. S. A. Damanhuri, A. A. Jasim, C. K. Tio, and H. Ahmad, "Current sensor based on microfiber knot resonator," *Sensors and Actuators A: Physical,* vol. 167, no. 1, pp. 377–381, 2011.

[13] Y. Wu, Y.-J. Rao, Y.-h. Chen, and Y. Gong, "Miniature fiber-optic temperature sensors based on silica/polymer microfiber knot resonators," *Opt. Express,* vol. 17, no. 20, pp. 18142-18147, 2009.

[14] G. Vienne, A. Coillet, P. Grelu, M. El Amraoui, J.-C. Jules, F. Smektala, and L. Tong, "Demonstration of a reef knot microfiber resonator," *Opt. Express,* vol. 17, no. 8, pp. 6224-6229, 2009.

[15] Y.-H. W. Chen, Yu; Rao, Yun-Jiang; Deng, Qiang; Gong, Yuan, "Hybrid Mach-Zehnder interferometer and knot resonator based on silica microfibers," *Optics Communications,* vol. 283, no. 14, p. 4, 2010.

[16] Y. Li and L. Tong, "Mach-Zehnder interferometers assembled with optical microfibers or nanofibers," *Opt. Lett.,* vol. 33, no. 4, pp. 303-305, 2008.

[17] C. Caspar and E. J. Bachus, "Fibre-optic micro-ring-resonator with 2 mm diameter," *Electronics Letters,* vol. 25, no. 22, pp. 1506-1508, 1989.

[18] X. Guo and L. Tong, "Supported microfiber loops for optical sensing," *Opt. Express,* vol. 16, no. 19, pp. 14429-14434, 2008.

[19] O. Schwelb, "Transmission, group delay, and dispersion in single-ring optical resonators and add/drop filters-a tutorial overview," *Lightwave Technology, Journal of,* vol. 22, no. 5, pp. 1380-1394, 2004.

[20] L. F. Stokes, M. Chodorow, and H. J. Shaw, "All-single-mode fiber resonator," *Opt. Lett.*, vol. 7, no. 6, pp. 288-290, 1982.

[21] K. S. Lim, S. W. Harun, A. A. Jasim, and H. Ahmad, "Fabrication of microfiber loop resonator-based comb filter," *Microwave and Optical Technology Letters*, vol. 53, no. 5, pp. 1119-1121, 2011.

[22] F. Xu, V. Pruneri, V. Finazzi, and G. Brambilla, "An embedded optical nanowire loop resonator refractometric sensor," *Opt. Express*, vol. 16, no. 2, pp. 1062-1067, 2008.

[23] G. Vienne, L. Yuhang, and T. Limin, "Effect of Host Polymer on Microfiber Resonator," *Photonics Technology Letters, IEEE*, vol. 19, no. 18, pp. 1386-1388, 2007.

[24] L. Tong, R. R. Gattass, J. B. Ashcom, S. He, J. Lou, M. Shen, I. Maxwell, and E. Mazur, "Subwavelength-diameter silica wires for low-loss optical wave guiding," *Nature*, vol. 426, no. 6968, pp. 816-819, 2003.

[25] H. Dong, G. Zhu, Q. Wang, H. Sun, N. K. Dutta, J. Jaques, and A. B. Piccirilli, "Multiwavelength fiber ring laser source based on a delayed interferometer," *Photonics Technology Letters, IEEE*, vol. 17, no. 2, pp. 303-305, 2005.

[26] X. Zeng, Y. Wu, C. Hou, J. Bai, and G. Yang, "A temperature sensor based on optical microfiber knot resonator," *Optics Communications*, vol. 282, no. 18, pp. 3817-3819, 2009.

[27] S.-H. Hsu and Y.-T. Huang, "Design and analysis of Mach-Zehnder interferometer sensors based on dual strip antiresonant reflecting optical waveguide structures," *Opt. Lett.*, vol. 30, no. 21, pp. 2897-2899, 2005.

[28] C.-Y. Wu, P. Lin, R.-S. Huang, W.-C. Chao, and M. M. H. Lee, "Design optimization for micromachined low power Mach-Zehnder thermo-optic switch," *Applied Physics Letters*, vol. 89, no. 12, pp. 121121-3, 2006.

[29] L. Zhou and A. W. Poon, "Fano resonance-based electrically reconfigurable add-drop filters in silicon microring resonator-coupled Mach-Zehnder interferometers," *Opt. Lett.*, vol. 32, no. 7, pp. 781-783, 2007.

[30] L. Tong, L. Hu, J. Zhang, J. Qiu, Q. Yang, J. Lou, Y. Shen, J. He, and Z. Ye, "Photonic nanowires directly drawn from bulk glasses," *Opt. Express*, vol. 14, no. 1, pp. 82-87, 2006.

[31] D. Dai and S. He, "Highly sensitive sensor based on an ultra-high-Q Mach-Zehnder interferometer-coupled microring," *J. Opt. Soc. Am. B*, vol. 26, no. 3, pp. 511-516, 2009.

Chapter 5

APPLICATIONS OF MICROFIBER BASED RESONATORS

5.1 Introduction

Microfiber based resonators offer a number advantages in high compactness, small wavelength spacing, simplicity in fabrication and low cost. With these advantages, microfiber based resonator makes a good candidate as optical multichannel fiber for the multiwavelength lasers system. Due to the large evanescent field of the microfibers, microfiber devices are sensitive to the ambient condition. Thus microfiber based resonators are also suggested in many sensing applications particularly in the chemical, refractive index and temperature sensing [1-4]. In the case of temperature sensing, the transmission spectrum of microfiber knot resonator (MKR) shifts as the ambient temperature varies. Such effect is attributed to the thermal dependency of the microfiber length and refractive index. Beside temperature sensors, this characteristic can be exploited in other applications such as electric current sensing and for tuning the transmission spectrum of optical filter.

In the earlier chapters, several interesting characteristics of microfiber based resonators have been discussed such as the periodic multichannel spectrum, polarization dependent resonance and thermal–induced spectral shift. In this chapter, several new optical devices are proposed and demonstrated using the fabricated microfiber resonator. Two multiwavelength lasers are demonstrated using a microfiber loop resonator (MLR) as a wavelength selection filter. The MLR is also used for temperature sensing. Finally, current sensor based on an MKR is demonstrated.

5.2 MLR as a Multichannel Filter for Multiwavelength Laser

Multi-wavelength fiber lasers have gained great interests recently for such applications as in wavelength division multiplexing (WDM) networks, radio frequency (RF) photonics and fiber-optic sensors [5, 6]. These lasers provides efficient and cost effective simultaneous multichannel source for WDM network. There are several ways of generating multiwavelength lasers for instance semiconductor optical amplifier (SOA) [5], Erbium-doped fiber amplifier (EDFA) [7], Raman [8], Brillouin [9] and etc. In this section, two multiwavelength lasers based on SOA and EDFA respectively are presented. MLR is used as multichannel filter to create multiple wavelength generation in the laser output.

5.2.1 SOA based Multiwavelength Laser

One of the important criteria in achieving high quality multiwavelength laser is to incorporate suitable gain medium that possesses high stability in multi-wavelength lasing. Among many gain mediums, SOA is one of the promising candidates due to its inhomogeneous gain characteristics and can support many simultaneous lasing wavelengths [5, 10]. Nevertheless, SOA suffers strong mode competition if the wavelength spacing is within homogenous broadening linewidth. To overcome this problem, some literatures have suggested exploiting nonlinear polarization rotation effect in the fiber ring cavity to induce intensity dependent loss and suppress the mode competition in the gain medium. Stable and power-equalized multi-wavelength lasers with small wavelength spacing have been demonstrated by using that method [11, 12]. On the other hand, optical multichannel filter is also an important component in realizing multi-wavelength fiber lasers and therefore, many comb-filters have been proposed, for instance Fabry-Perot interferometer [12], fiber Bragg gratings (FBGs) [13], Mach-Zehnder interferometers [14] and fiber loop mirrors [15]. MLR is another

type of multichannel filter which is fabricated from microfibers [1, 16]. Similar to other optical filter, MLR possesses a comb-like transmission spectrum which makes it a comparable candidate for the use in multi-wavelength laser cavity.

In this experiment, a new stable narrow wavelength spacing multi-wavelength fiber laser is constructed using a SOA as a gain medium and MLR as a comb filter. To meet the requirement of narrow spacing, a MLR with a long loop length is used, which was fabricated by coiling the tapered fiber onto itself and embedded in a low index material for robustness. The polarization dependent coupling of the MLR is investigated and exploited in optimizing the extinction ratio of the multi-wavelength lasers.

Experimental Setup

The experimental setup of the proposed multi-wavelength fiber laser is depicted in Figure 5.1. The ring laser cavity consists of an SOA as the gain medium, an MLR as a multichannel filter, an optical isolator, a polarizing beam-splitter (PBS), polarization controllers (PCs) and a 10 dB output coupler. The isolator is used to ensure unidirectional operation in the ring cavity while the PBS is used to polarize the wave from the SOA. PC1 and PC2 are used to optimize the resonance condition of the MLR. In the operation, SOA is biased at 220 mA and output spectrum of the laser is measured by an optical spectrum analyser (OSA) from 10% port of the output coupler. For the ease of integrating the MLR in the experimental setup, the MLR used in the setup was embedded in low-index material based on the technique discussed earlier in Section 3.6. Initially, the fabricated microfiber had an insertion loss of approximately 1 dB. The loss increased to ~7 dB after it was manufactured into microfiber loop resonator and embedded in the low-index material.

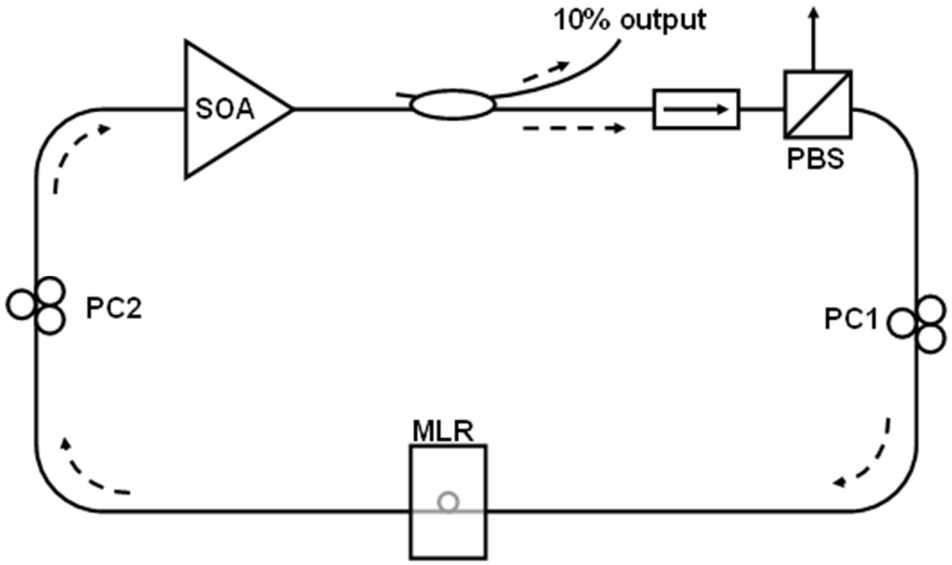

Figure 5.1: Schematic diagram of the experimental setup

Extinction Ratio Enhancement Using PBS

The transmission spectrum of the fabricated MLR is measured using an amplified spontaneous emission (ASE) source in conjunction with the OSA. Figure 5.1 shows the transmission spectrum of fabricated MLRs under three different scenarios; (i) without PBS (ii) with PBS and PC is adjusted to obtain the smallest extinction ratio and (iii) with PBS and PC is adjusted to obtain the highest extinction ratio. In the experiment, an unpolarized ASE source is linearly polarized by a PBS before it is launched into the fabricated MLR. A PC incorporated in between the source and MLR is used to control the state of polarization (SOP) of the light source. As shown in Figure 5.2, the free spectral range (FSR) of the MLR is about 0.16 nm, which was obtained by precise adjustment of loop length during fabrication process. Since transmission spectrum of (i) in Figure 5.2 was acquired based on an unpolarized input light and the resonance condition is found to be unaffected by the adjustment of the PC.

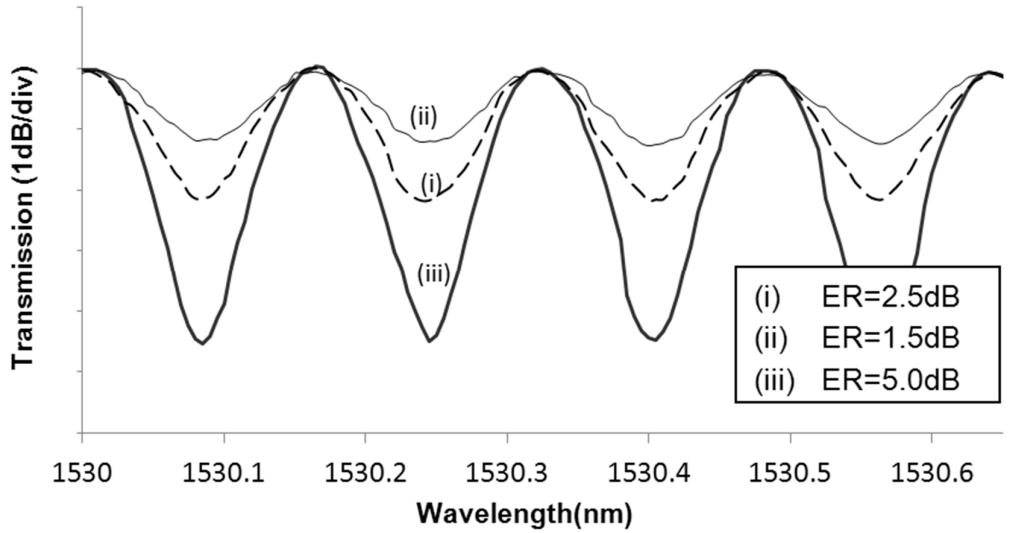

Figure 5.2: The transmission spectra of the fabricated MLR for different input SOP (i) unpolarized input light (ii) polarized input light with smallest resonance (iii) polarized input light with the highest resonance.

In contrast, the resonance condition for the MLR with a polarized input light is very sensitive to the PC adjustment as illustrated in spectra (ii) and (iii) of Figure 5.2. The transmission spectra (ii) and (iii) show the respective lowest and the highest resonance extinction ratio achieved by a polarized input light with a careful adjustment of the PC. However, it was found that the wavelength of each peak in the same figure is unaffected by the changing of input SOP. It is appropriate to attribute this phenomenon to the polarization dependent coupling in the MLR where the interfiber coupling, twisting and alignment of microfiber in the coupling region are accounted for the coupling coefficient difference between two orthogonal polarization states [17-19]. Associated with the coupling ratio, the resonance condition of the MLR can be manipulated by the adjustment of PC.

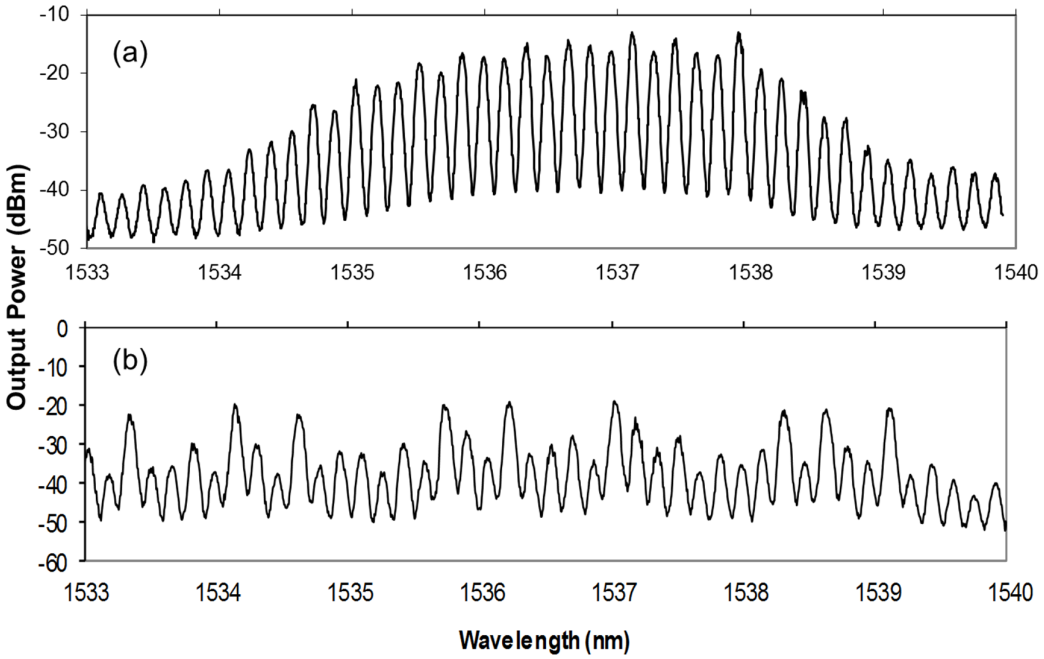

Figure 5.3: Output spectrum of the multiwavelength laser (a) with PBS (b) without PBS

Figure 5.3 shows the output spectrum of the proposed SOA-based multi-wavelength laser. In the experiment, SOA is biased at 220 mA and a stable and power-equalized multi-wavelength oscillation with similar wavelength spacing of 0.16 nm is obtained as shown in Figure 5.3(a). The wavelength spacing of the laser is observed to be coincided with the FSR of the MLR used. As a comparative study, the experiment is repeated without the PBS in the ring cavity and the output spectrum is as shown in Figure 5.3(b). In contrast, the power distribution among the wavelengths is not uniform and the power of each wavelength fluctuates over time. The main cause of the lasing instability is that the wavelength spacing is in the same order of magnitude with the SOA homogeneous broadening linewidth and there is a strong mode competition among the lasing wavelengths. Besides, the poor extinction ratio of the MRL is accounted for this instability. Multichannel filter with high extinction ratio is effective in slicing the ASE of the gain medium and producing lasers with narrow linewidth. Fewer longitudinal modes can oscillate in the ring cavity and the mode competition can be

alleviated. Thus, PBS is used to enhance the resonance extinction ratio of MLR and improve the lasing stability.

On the other hand, the PC-PBS-PC combination induces intensity dependent loss in the ring cavity by exploiting the nonlinear polarization rotation (NPR) in the SOA which helps to suppress the mode competition within the homogeneous broadening linewidth and stabilize multi-wavelength oscillation. Figure 5.4 shows the repeated scanning of the proposed laser output spectrum at interval time of 5 minutes for over 10 times. The signal to noise ratio is 25 dB and the power fluctuation of each wavelength is below 0.4 dB which indicates an excellent stability in the multi-wavelength oscillation.

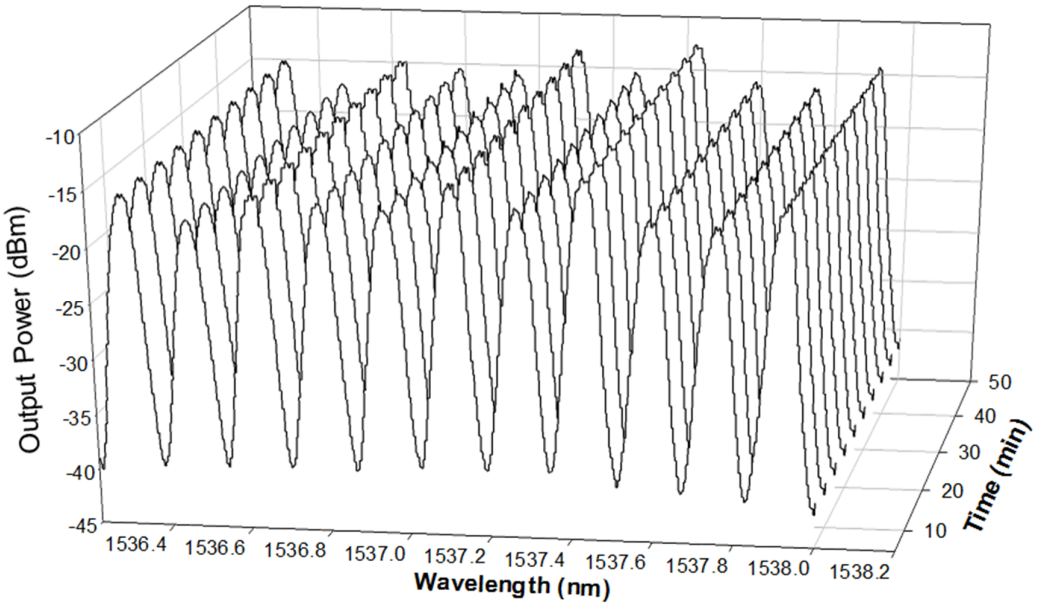

Figure 5.4: Output spectrum of the proposed laser against time. The output spectrum is scanned for every 5 minutes.

5.2.2 EDF-based Multiwavelength Laser

There has been some intense study in EDF-based multiwavelength lasers due to their potential in many applications such as DWDM network, optical fiber sensor and spectroscopy. The capability of generating a large number of wavelength lasings from a compact single laser source has significantly reduced the cost and enhanced the flexibility in the deployment of the laser source. At room temperature, EDF is a homogenous gain medium. Thus, there is a strong mode competition among the wavelengths in the medium, particularly if the spacing between two adjacent wavelengths is within the homogenous linewidth, simultaneous wavelength lasing is highly unstable. Fortunately, there are several solutions has been suggested to solve this problem such as employing NPR to induce intensity dependent lost [11], including SOA in the laser cavity to generate phase modulation eliminating mode competition in EDFA [20] and homogenous linewidth reduction by cooling EDF with liquid-nitrogen temperature [21] and mode competition suppression by exploiting degenerate and nondegenerate four-wave mixing (FWM) effect in the multiwavelength laser [22-27].

By employing highly nonlinear fiber (HNLF) in the fiber laser, the nonlinearity of the lasing cavity is increased by γPL where γ is the nonlinear coefficient of the HNLF, L is the length of the nonlinear medium and P the wave power inside the cavity. With larger pump power (P) or longer highly nonlinear fiber length (L), a better quality multiwavelength laser can be achieved in terms of wavelength stability, spectrum power flatness and lasing spectrum width [27]. In a HNLF, both nondegenerate and degenerate FWM occurs at very low power among all the wavelengths and the power of every wavelength is transferred and distributed among other wavelengths. The wavelength energy tends to be transferred from the higher power wavelengths to those with lower power and the lasing power is distributed equally among the wavelengths. Thus, the mode competition is suppressed and stable multiwavelength laser is achieved. With

additional perpetual energy supply from the amplifier, more wavelengths are generated and widen the lasing region. Depending on the product, γPL, the energy transfer efficiency among the wavelengths is linearly proportional to nonlinear medium length L.

In this section, an EDF-based multiwavelength laser is demonstrated using a HNLF with double-pass approach in conjunction with an MLR. With the assistance of circulator and fiber mirror, the lasing wave that propagates unidirectionally in the ring cavity is circulated and double propagates through a 100 m long HNLF. By double propagating through the HNLF, the wave experiences twice the nonlinearity and FWM efficiency compared to the ordinary configuration. Thus, multiwavelength lasing can be further enhanced based on this approach. To create mode competition condition among the wavelengths in the ring cavity, a MLR with a wavelength spacing as small as 0.162 nm at 1530 nm is used as a comb filter in the proposed laser. To facilitate the comparative study, several experiments based on different configurations have been implemented. The experimental results indicate that the proposed bidirectional configuration outperforms other with distinctive performance in terms of multiwavelength laser stability, broader and flatter lasing spectrum.

Experimental Setup and Operating Principle

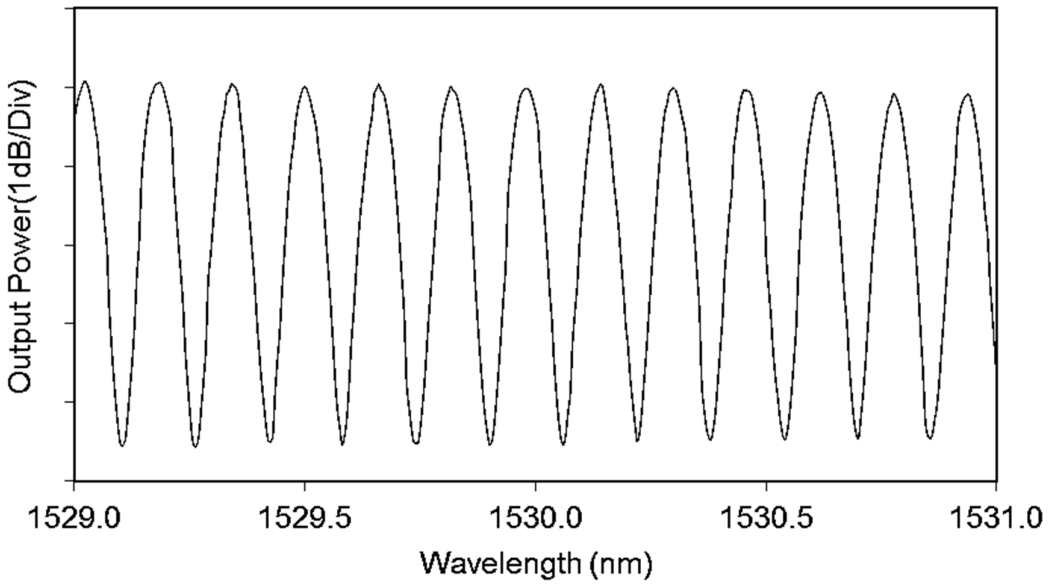

Figure 5.5: The output spectrum of the proposed MLR

In this experiment an MLR is used as a comb filter. To fabricate the MLR, a fiber is tapered until the waist diameter down to 1 μm. Then, the tapered fiber is coiled to make a ring. The small waist diameter ensures a strong coupling in the MLR. MLR acts as a comb filter to slice the ASE spectrum, which oscillates in the ring cavity to generate comb-like laser with assistance from the FWM effect. MLR used in this experiment has the spectrum wavelength spacing as small as 0.162 nm proving it to be better than other comb filter available. As the wavelength spacing is small, efficient FWM may occur in the ring cavity because of small phase mismatch. The MLR spectrum is as shown in Figure 5.5. Extinction ratio of this spectrum is 4.5 dB.

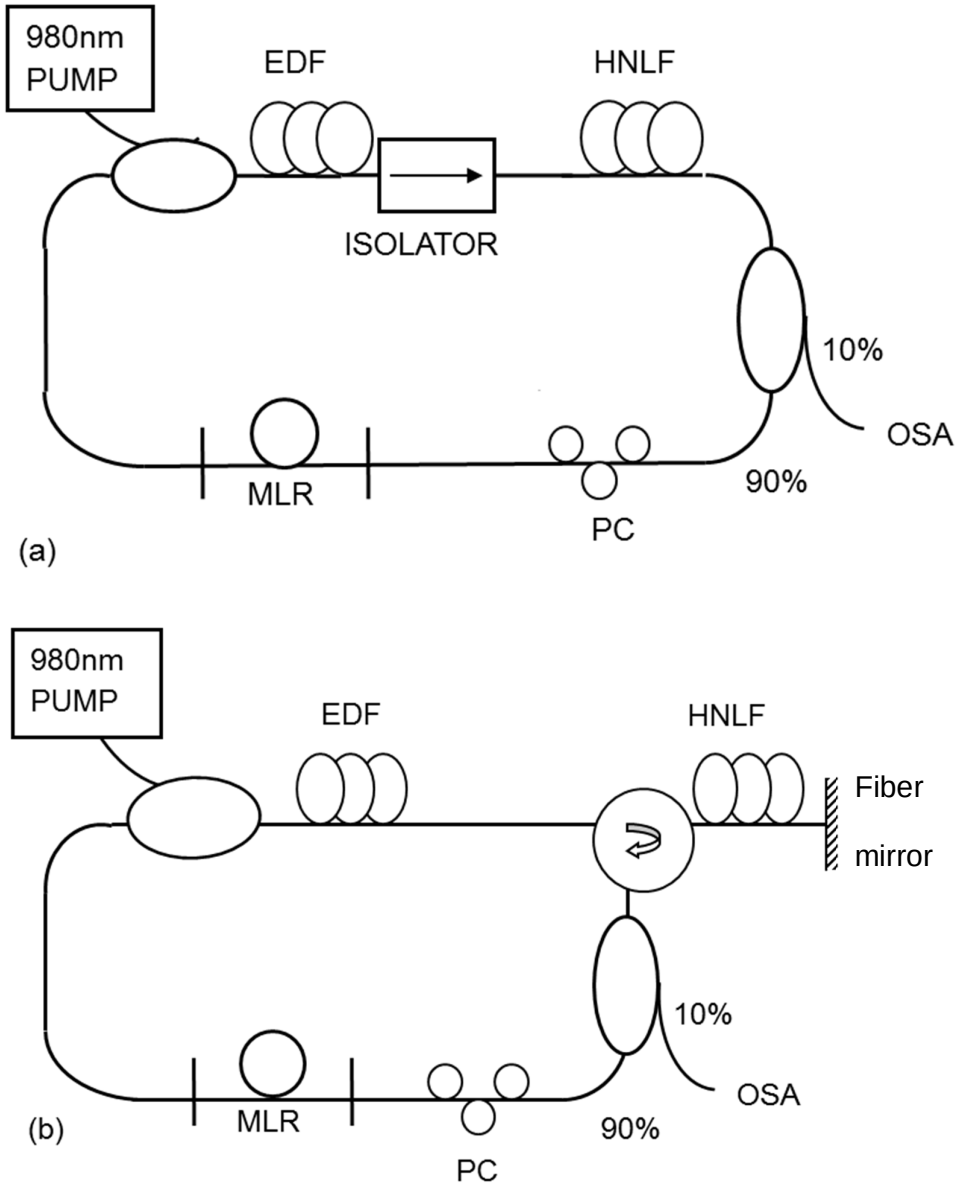

Figure 5.6: Schematic illustrations of the experimental setups of different configurations (a) conventional single pass HNLF (b) double pass HNLF

Figure 5.6 shows the configurations of EDF-based multiwavelength laser using an MLR as a multichannel filter. Both configurations consist of 980 nm pump diode, WDM coupler and EDF as the gain medium. In the conventional configuration of Figure 5.6(a), an isolator is used to ensure unidirectional propagation of light in the cavity. A 100 m HNLF with the nonlinear coefficient of 10.8 /W·km, loss of 0.73 dB/km and 0.0095 ps/ (nm^2·km) dispersion slope (almost flat) at 1530 nm is employed in both configurations to suppress the mode competition among the wavelengths by

means of inducing degenerate and nondegenerate FWM among the wavelengths in the ring cavity. In addition, gain peak wavelength of the 980 nm pumped EDF is at 1530 nm which coincides with the zero dispersion wavelength of the HNLF, 1531 nm. Under this condition, a strong FWM effect among the wavelengths is triggered in the multiwavelength laser generation. In both setups, MLR and EDF are polarization sensitive and therefore a polarization controller (PC) is used to adjust the polarization state of the wave inside cavity and optimize the multiwavelength lasing performance. To further enhance the nonlinearity in the ring cavity, the double pass approach is used as shown in Figure 5.6(b). A 95% broadband fiber mirror reflector is placed at the end of HNLF to reflect the wave back to the HNLF. From the HNLF, the reflected wave is circulated back to the ring cavity by the circulator. The oscillating wave in the cavity experiences twice as much as the nonlinearity compared to the previous configuration of Figure 5.6(a) and thus the FWM efficiency and energy transfer among the wavelengths are doubled in the proposed multiwavelength laser.

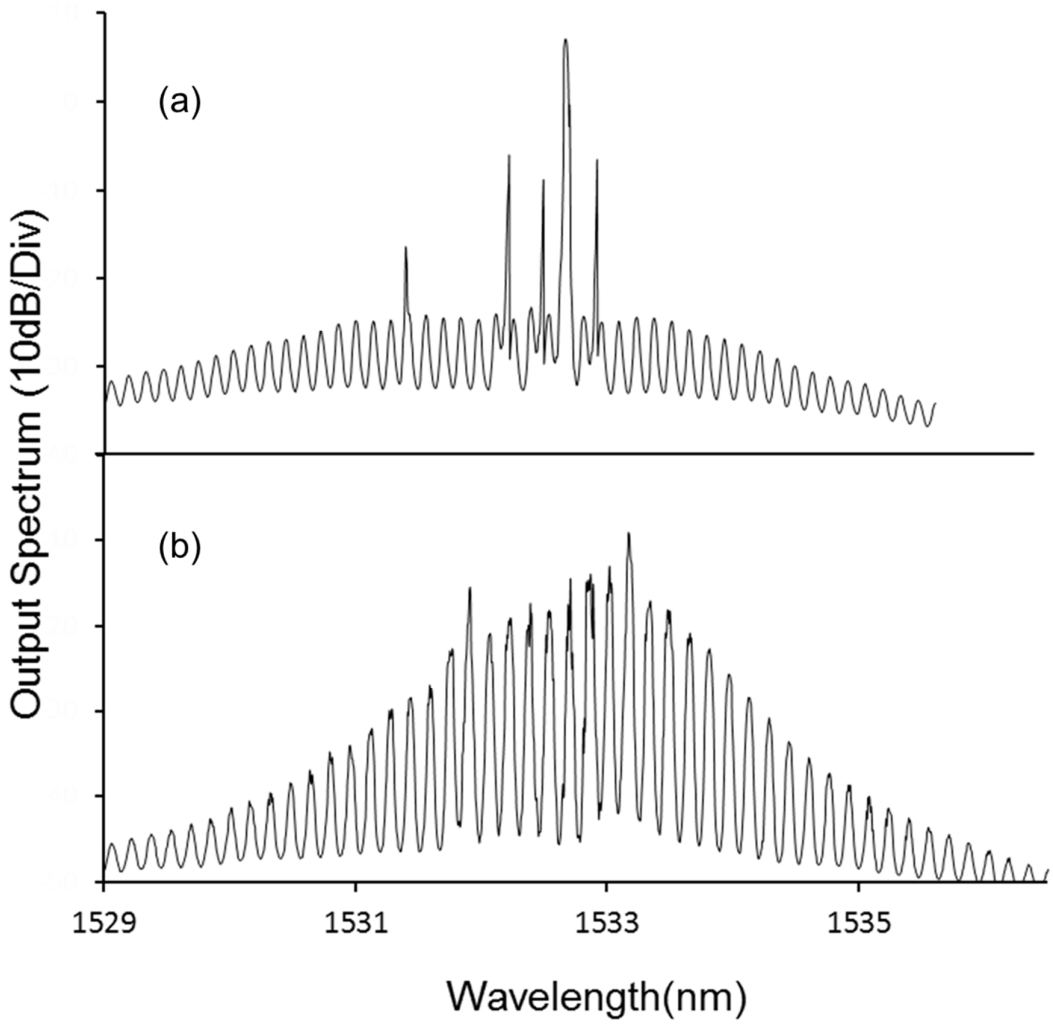

Figure 5.7: Output spectra of the laser based on single pass configuration (a) without HNLF and (b) with HNLF

Figure 5.7(a) shows the output spectrum of the conventional EDF-based multiwavelength laser, which was configured without HNLF. Small wavelength spacing by the MLR causes a strong mode competition among different wavelength in the ring cavity. There are only a few wavelengths dominating the lasing spectrum and the power of each lasing wavelength is fluctuating over time. By employing HNLF as the proposed configuration of Figure 5.7(a), under the same pump condition with the previous experiment, the wavelength oscillation is observed to be relatively stable. As shown in Figure 5.7(b), more number of excited wavelengths is obtained in the

spectrum and the power distribution among the wavelengths is also improved. This result clearly shows that the HNLF is playing a major part stabilizing the laser by suppressing the mode competition among the wavelengths in the laser and distributing the lasing power from the high power wavelengths to the low power wavelengths. However, the flatness of the spectrum power is not satisfactory and it can be further improved by increasing the nonlinearity (γPL) in the ring cavity.

In the proposed configuration of Figure 5.7(b), the oscillating wave in the cavity passes through the HNLF twice. Along the HNLF, the FWM interaction length between two co-propagating frequency components is approximately 2L whereas the FWM interaction between the counter-propagating frequency components can be neglected. On the other hand, the dispersion of the HNLF is an important factor in influencing the FWM effect. The FWM efficient is governed by the phase mismatch among three adjacent frequency components in the spectrum which can be well expressed by [28]

$$\Delta\beta_{ijk} = \beta_2(\omega_0)\Omega^2 + \beta_3(\omega_0)(\omega_0 - \omega_k)\Omega^2 + \ldots \qquad (5.1)$$

where $\beta_2(\omega_0)$ and $\beta_3(\omega_0)$ are second order and third order propagation coefficients at frequency ω_0 and Ω is the frequency shift.

In this analysis, degenerate FWM is likely the dominant nonlinear effect in the HNLF and thus non-degenerate FWM is neglected. Since the dispersion is almost flat within the vicinity of zero dispersion wavelength, the phase mismatch can be simplified as

$$\Delta\beta_{ijk} \cong \beta_3(\omega_0)(\omega_0 - \omega_k)\Omega^2 \qquad (5.2)$$

and the higher order terms in the phase mismatch can be neglected. The frequency shift can be well approximated by

$$\Omega \approx 2\pi c\frac{\Delta\lambda}{\lambda^2} \qquad (5.3)$$

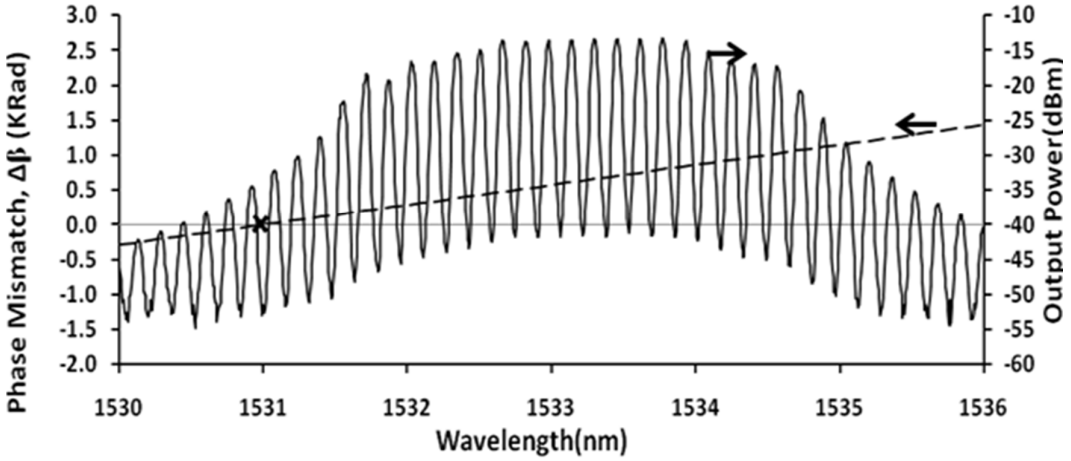

Figure 5.8: The output spectrum of the proposed configuration and the phase mismatch. ($\beta_3(\omega_0)$ = 0.01469 ps^3/km, $\Delta\lambda$ = 0.162 nm at 1530 nm).

Figure 5.8 shows overlaid graph of output spectrum of the proposed configuration and phase mismatch in the HNLF. Four waves mixing is a phase sensitive effect and it is very strong within the vicinity of region zero phase mismatch. In the range from 1531.7 nm to 1534.6 nm, the lasing wavelengths are close to zero dispersion wavelength (1531 nm) of the HNLF to induce strong FWM effect. For dispersion slope of HNLF is $\frac{dD}{d\lambda}$ = 0.0095 ps/nm^2.km, a total number of 19 lasing wavelengths with an average output power of -15.2 dBm and peak power difference of less than 5 dBm are produced. The number of lasing wavelengths is relatively higher considering the same pump power used in this experiment and OSNR achieved in this spectrum is 26.79 dB.

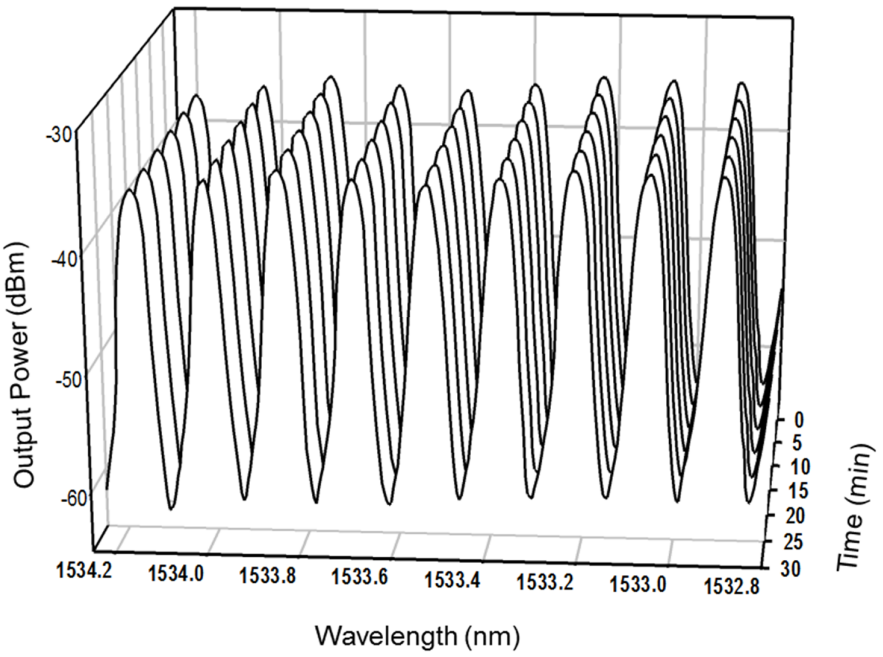

Figure 5.9: Successive spectra of the multiwavelength laser at interval time of 5 minutes.

Figure 5.9 shows successive scan of the multiwavelength laser every 5 minutes for 25 minutes. The power for each wavelength is stable over the time without fluctuation. This shows that the mode competition in laser cavity is suppressed within the wavelength range. HNLF has successfully stabilized the proposed EDF–based multiwavelength laser with FWM process.

5.3 Microfiber Resonator Based Sensor

Fiber-optic sensors have found increasing applications in many fields and various types of sensors have been proposed and demonstrated [29-31, 40]. However, there are pros and cons for every type of sensor. For instance, FBG based sensors are widely used and their fabrication require expensive phase-masks. Tapered micro-structured fibers are expensive and difficult to work with due to some difficulty in achieving low loss splicing with standard optical fiber. In contrast, microfiber-based sensors do not have the similar problems and they are well known as the simplest

devices due to their simple and economic fabrication process [32-34]. In this section, microfiber resonator based sensors are experimentally demonstrated and theoretically analysed for two different physical parameters – temperature and electric current.

5.3.1 Microfiber Loop Resonator Based Temperature Sensor

In this section, a MLR-based temperature sensor is demonstrated. The microfiber is first produced by heating a conventional fiber to its softening temperature, and then the ends are pulled apart to reduce the diameter of fiber down to around 1-3 μm. The detail of this fabrication technique can be found in Chapter 3. The MLR used is fabricated by coiling the microfiber onto itself; van der Waal attraction is exploited to maintain the loop structure by overcoming the elastic force that makes the fiber straight. The fabricated MLR is laid on an earlier prepared glass plate with a thin and flat layer of low refractive index material to address the temporal stability of the device as shown in Figure 5.10. A bare MLR may be exposed to dust and moisture that can cause temporal loss of instability to the device. The thickness of the low refractive index material is approximately 0.5 mm which is thick enough to prevent leakage of optical power from the microfiber to the glass plate.

Some uncured resin is applied in the surrounding of the MLR before it is sandwiched by another glass plate with the same low refractive index resin layer from the top. It is essentially important to ensure that minimum air bubbles and impurity are trapped around the fiber area between the two plates. This is to prevent refractive index non-uniformity in the surrounding of the microfiber that may introduce loss to the system. The uncured resin is solidified by UV light exposure for 3 ~7 minutes and the optical properties of the MLR are stabilized. The packaged MLR is placed in an oven with temperature control to investigate how the comb spectrum changes with the temperature.

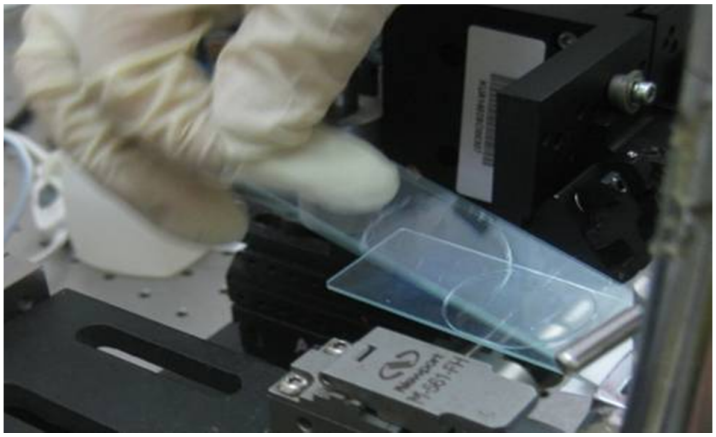

Figure 5.10: Packaging of the MLR.

Performance of the MLR-based temperature sensor

An MLR has a comb transmission spectrum similar to that of a Fabry–Perot filter. Refer to Eqn. (4.26) of the previous chapter, the smaller full wave at half maximum (FWHM) is required to achieve a higher *Q*-factor. The coupling coefficient depends on the overlapping area, effective index and the diameter of the microfiber. The measured comb transmission spectrum of the MLR is shown in Figure 5.17, which was obtained by using the ASE source in conjunction with an OSA. The resonant response of the MLR is obvious. The extinction ratio is about 4.0 dB, and the FSR is 0.08 nm. The actual radius of the MLR is around 3 mm.

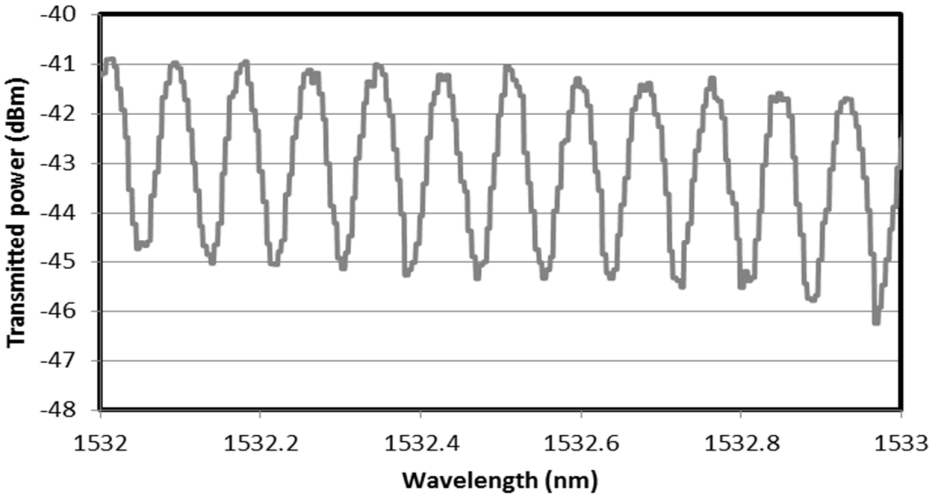

Figure 5.11: Transmission spectrum of the fabricated MLR.

Once fabricated, the temperature response of the packaged MLR is then investigated. Figures 5.12(a)-(c) show the transmission spectrum of another packaged MLR at various temperatures. As shown in this figure, the spacing of the transmission comb spectrum is unchanged with the temperature. However, a linear dependence of the extinction ratio of the MLR on temperature can be observed; at higher temperature MLRs have a smaller extinction ratio. Figure 5.13 shows the relationship between the extinction ratio and the temperature. As seen, the slope of the extinction ratio reduction against temperature is ~0.043 dB/°C. The dependence of the extinction ratio on temperature is due to thermo-optic and thermal-expansion characteristics of the silica microfibers and the host polymer. This affects the resonance condition of the resonator, which in turn reduces the extinction ratio. In the proposed sensor, the optical path length does not change much with the temperature and therefore, the comb spacing is unchanged as indicated in Figure 5.12.

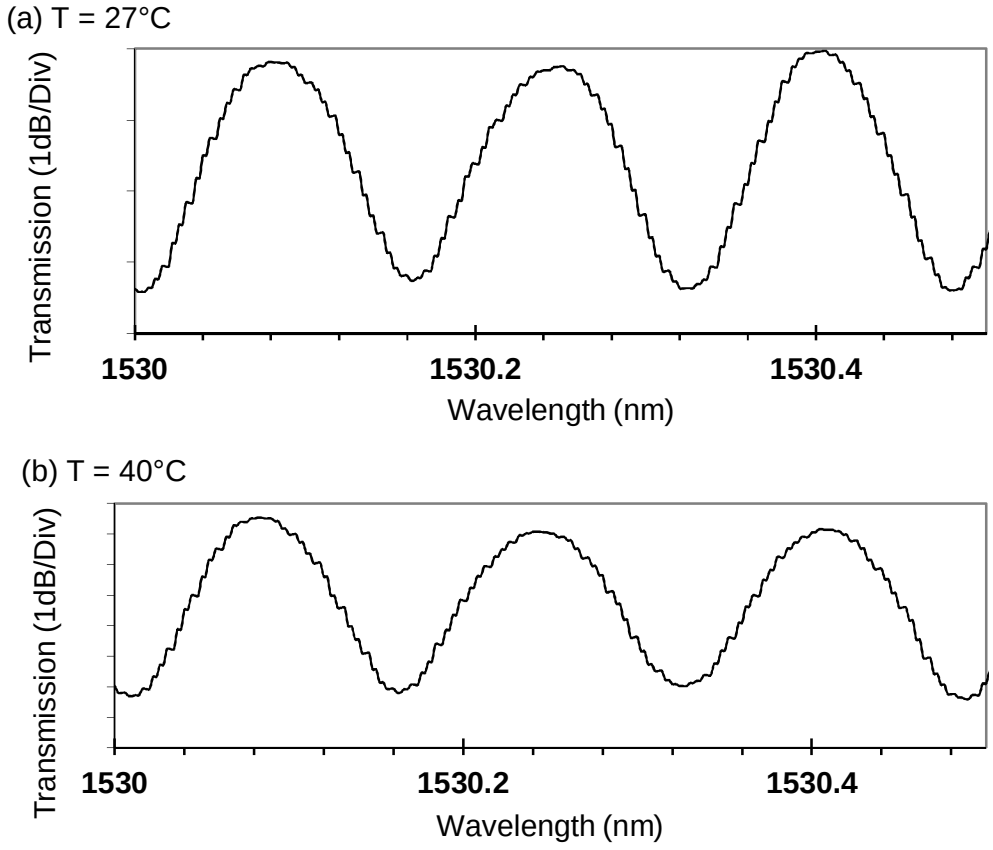

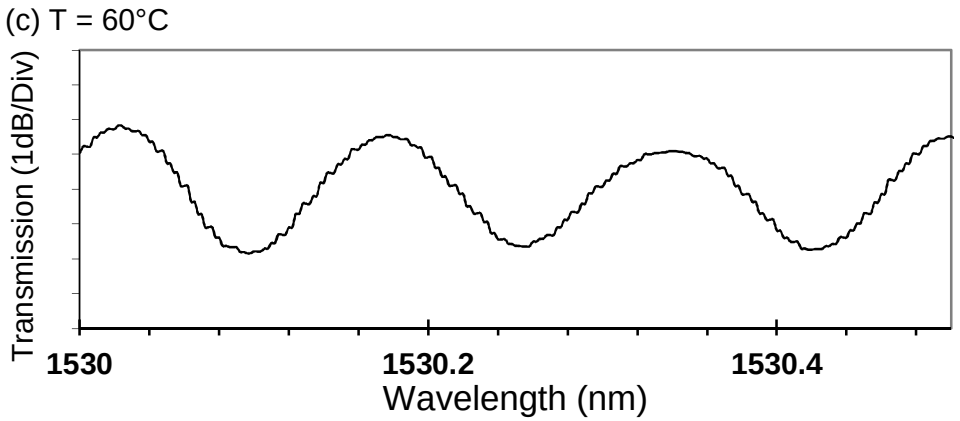

Figure 5.12: Transmission spectra of the fabricated MLR obtained at temperatures (a) 27°C (b) 40°C (c) 60°C.

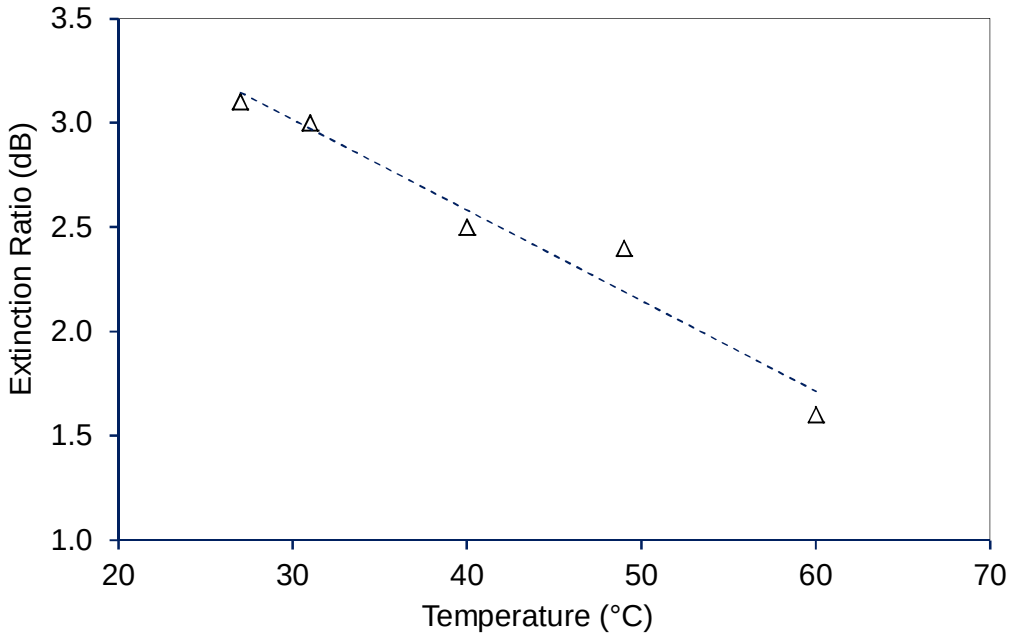

Figure 5.13: Variation of resonance extinction ratio with the increasing temperature.

As compared with the model of temperature sensors that based on spectral shift in microfiber resonators [4, 35], this model is based on the variation of resonance extinction ratio in response to the temperature change. The measurement of extinction ratio is obviously easier and less complicated than that of resonance wavelengths. The operating cost for this sensor can be made lower because of the simpler operating mechanism.

5.3.2 Microfiber Knot Resonator Based Current Sensor

A variety of fiber optic based current sensors have been investigated in recent years using mainly a silica based single mode fiber (SMF). They are typically divided into two categories, where one is based on Faraday Effect [36] and the other is based on thermal effect. The former is capable to remotely measure electrical currents, but the device requires a long fiber due to the extremely small Verdet constant of silica. The latter needs a short length of fiber but requires complex manufacturing techniques to coat fibers with the metals. Recently, a resonance wavelength of the MLR has been experimentally reported to shift with electric current applied to the loop through a copper wire. An acceptable transmission loss is achieved despite the fact that copper is not a good low-index material to support the operation of such structure [37]. This finding has opened up a way to enable dynamic and efficient spectrum control for optical filters by manipulating an electric current dependence spectral shift characteristic of the microfiber based resonator. Microfiber based devices have a strong dependence on temperature due to the thermal expansion characteristic and thermo-optic effect of silica glass. As discussed earlier in Section 4.3.2, the transmission spectrum of a microfiber based device shifts as the ambient temperature varies and the relationship between these two variables is well described by the linear equation in Eqn. (4.31).

In this section, MKR-based current sensor is demonstrated based on the idea of thermally induced resonance wavelength shift. By manipulating the applying electric current through the microfiber knot wrapped copper wire, the copper wire acts as a heating element and induces temperature change in the MKR. The transmission spectrum of the MKR shifts corresponds to the temperature change. These modified MKRs can be used as low-cost and fast response tunable optical filters which are useful in the applications of optical signal processing, WDM communication and etc. On the

other hand, this MKR-based device may operate as a dynamic current sensor with strong immunity to electric noise. In addition, it has a dynamic operational range extending to the regime of extreme high temperature or pressure.

Experiment

First, a ~2 μm diameter silica microfiber is fabricated from a SMF using flame brushing technique [38]. Then the microfiber is cut and separated into two unequal parts in which the longer one is used in the knot fabrication and the other one is used as a collector fiber to collect the transmitted light from the MKR [39]. During the fabrication of the knot, the copper wire is inserted into the knot which diameter is bigger than the diameter of the copper wire (Refer Figure 5.14(a)). The light path from the knot resonator is completed by coupling the two microfiber ends. At least ~3 mm of coupling length between two microfibers is required to achieve strong van der Waal attraction force to keep them attached together. The microfiber knot diameter is then reduced and fastened on the copper wire by pulling microfibers from both arms of the microfiber knot as illustrated in Figure 5.14(b).

(a) (b)

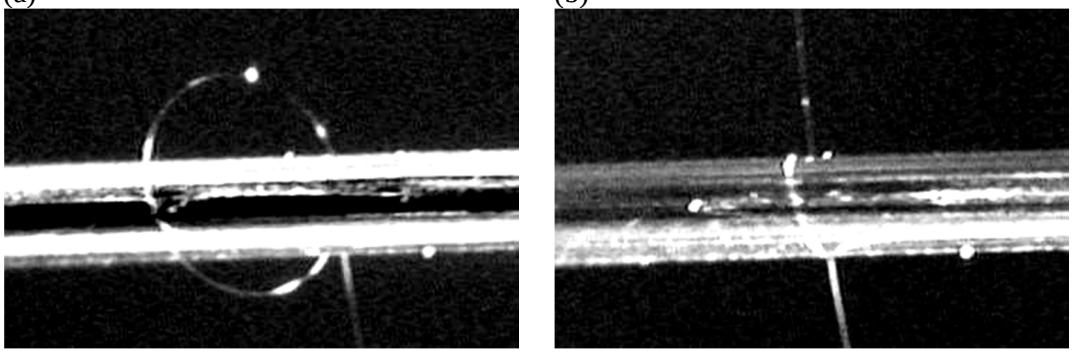

Figure 5.14: Optical microscope image of MKR tied on a copper wire.

The optical characteristics of the resonator are strongly affected by the tensile strain on the microfiber arms of the MKR induced by the pulling on the microfibers arms. It is essential to reduce the tension on the both arms of the MKR by moving the

fiber holders a bit closer to the microfiber knot after the knot is fastened. In spite of that, there is a very little change at the knot diameter and the resonance condition of the MKR remains good and stable after the tension is released.

Theoretical Analysis

MKRs share most of the optical properties with MLRs such as the free spectral range, which can be expressed as;

$$\mathrm{FSR} \approx \frac{\lambda^2}{n_{eff} L} \tag{5.4}$$

where λ is the operating wavelength, n_{eff} is the effective index of the microfiber and L denotes the single round-trip length in the resonator. The temperature variation affects both effective refractive index, n_{eff} and the loop length L, of the MKR. The variation in both parameters may lead to spectral shift and the relationship can be expressed as;

$$\frac{\Delta\lambda_{res}}{\lambda_{res}} = \left(\frac{\Delta n_{eff}}{n_{eff}} + \frac{\Delta L}{L} \right)_{Temp.} \tag{5.5}$$

Each term on the right hand side of the Eqn. (5.5) can be expressed in linear forms with temperature change ΔT as shown below:

$$\frac{\Delta n}{n} = \alpha \Delta T \tag{5.6}$$

$$\frac{\Delta L}{L} = \beta \Delta T \tag{5.7}$$

where α and β are the thermal expansion coefficient (TEC) and thermal-optic coefficient (TOC) of the microfibers respectively [35]. From the dimensionless fractional term $\frac{\Delta L}{L}$ in Eqn. (5.7), it is easily understood that at a given same temperature changes, the same resonance wavelength shift of the MKR can be achieved for any loop length value, L. By applying current, the copper wire act as a heating element and the heat generated

leads to instantaneous temperature rise in the MKR. Consider the linear relationship between the temperature change and heat energy generated by the conducting current, the relationship between wavelength shift and the current, I can be expressed in the form of

$$\frac{\Delta\lambda_{res}}{\lambda_{res}} \propto \frac{\rho I^2}{A} \tag{5.8}$$

where ρ and A represent the conductor resistivity and the cross sectional area of the conductor wire, respectively. The term ρ / A in Eqn. (5.8) is equivalent to the resistance per unit length of the conductor material. The resistivity of the copper wire is 1.68×10^{-8} Ω·m.

Current Response

For optical characterization of the MKR, broadband ASE source from an EDFA is first injected into the SMF and then it enters into the microfiber through the transition region. The light transmitted out from the MKR is collected by the collection fiber and measured by an OSA. The optical resonance is generated when circulating light in the MKR achieves a phase shift of multiples of 2π. When a DC current flows through the copper wire, heat is produced in the wire to change temperature. Because the MKR is in contact with the copper wire, any temperature changes will influence the refractive index and the optical path length of the MKR.

Figure 5.15 shows the resonant spectral of the MKR tied on a copper wire with various current loadings. In the experiment, the applying current is uniformly increased from 0 to 2 A. As shown in the figure, the resonance wavelength shifts to a longer wavelength as the conducting current in the copper wire increases. The response time of the wavelength shift is approximately 3 s and the spectrum comes to steady condition after 8 s. Therefore, each spectrum is recorded at ~10 s after the copper wire is loaded

with an electric current. At loading current I = 1.0 A, the resonance wavelength is shifted by ~30 pm from 1530.56 nm to 1530.59 nm and at I = 2.0 A, the resonance wavelength is further shifted to 1530.77 nm, 210 pm from the original wavelength. Inset of Figure 5.15 shows the free spectral range of the transmitted spectrum against the applying currents. As shown in the inset, FSR of the MKR remains unchanged at 1.5 nm with the increasing current. The calculated Q-factor and finesse of the MKR are ~4400 and 4.3 respectively. It is also observed that the transmission spectrum always shift towards the longer wavelength direction with increasing current regardless of the current flow direction, and the spectrum returns to original state once current supply is terminated.

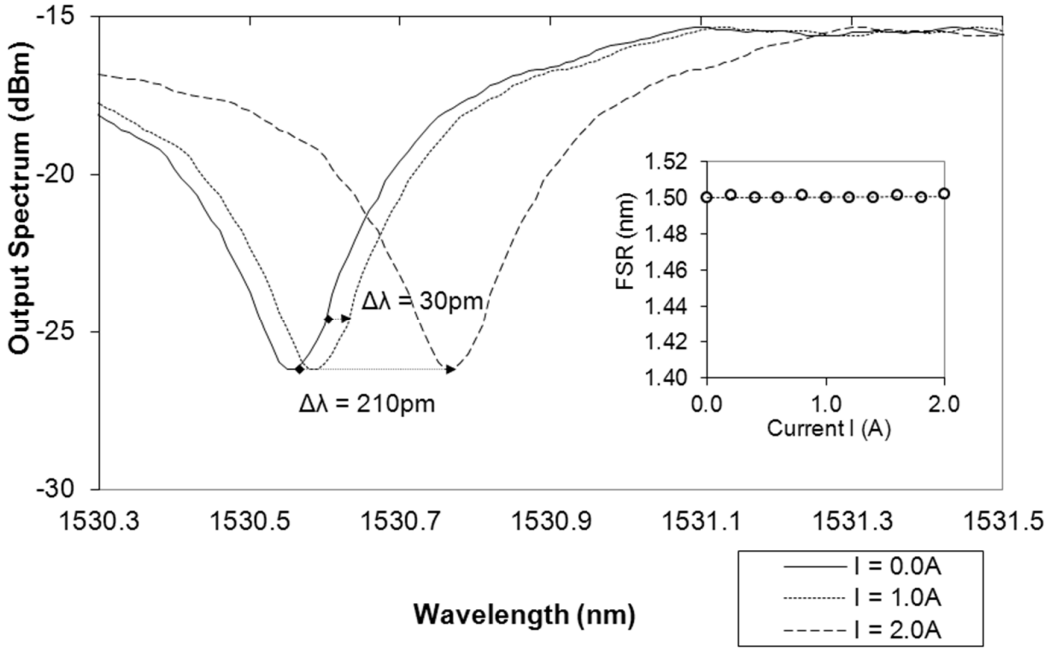

Figure 5.15: Resonance wavelength shift of the MKR tied on a copper wire loaded with different current. Inset shows unchanged FSR with the increasing current.

Figures 5.16(a) and 5.16(b) give schematic illustrations of MKR wrapped on a single copper wire and two copper wires respectively. The measured FSR and estimated knot diameter of the single-wire MKR are 1.7 nm and ~317 μm respectively while for the two-wire MKR, the measured FSR and estimated knot diameter are 1.46 nm and

~370 μm. An alternating current is applied through the copper wire and the resonance wavelength shift is investigated against the applying current. At small current of < 0.5 A, no significant resonance wavelength shift is observed. Beginning at 0.6 A, the resonance wavelength shifts gradually toward the longer wavelength. At applying current of 2.0 A, a wavelength shift of 0.208 nm and 0.09 nm are achieved with single and two copper wires configurations of Figures 5.16(a) and 5.16(b), respectively. Figure 5.17 shows the resonance wavelength shift against a square of current (I^2) for both configurations. The data set of each configuration can be well fit with a linear regression line with a correlation coefficient value r > 0.95. This justifies the linear relationship stated in Eqn. (5.8).

In comparing the conductor wire cross-sectional area between the two configurations, the two-wire configuration is twice larger than the single-wire configuration. Based on the relation in Eqn. (5.8), the tuning slope of the wavelength shift with I^2 of the two-wire configuration should be a half of the single-wire configuration. The slope of each linear line is 51.3 pm/A^2 (single wire) and 19.5 pm/A^2 (two wires) nonetheless it is reasonable to attribute the mismatch between the analysis and experiment to the different orientation and position of the wire(s) in the MKR. The tuning slope of the current sensor can be further increased by using different conductors with higher resistivity such as nichrome, constantan, graphite and etc. which are commonly used as heating elements. However, the suitability in integration with microfiber or other opto-dielectric device requires further investigation.

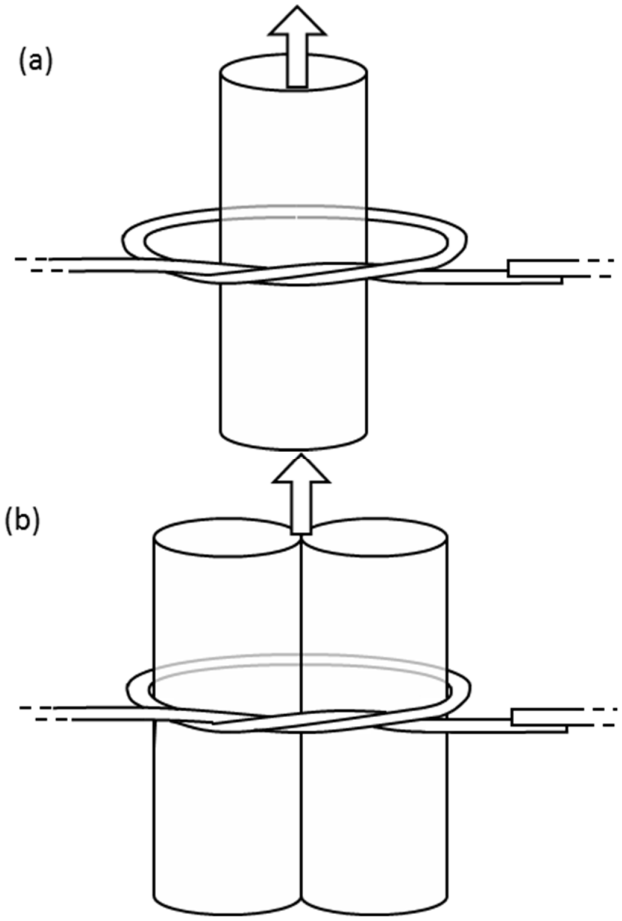

Figure 5.16: Schematic illustrations of microfiber knot tied on (a) single copper wire (b) two copper wires with identical wire diameter of ~200 μm.

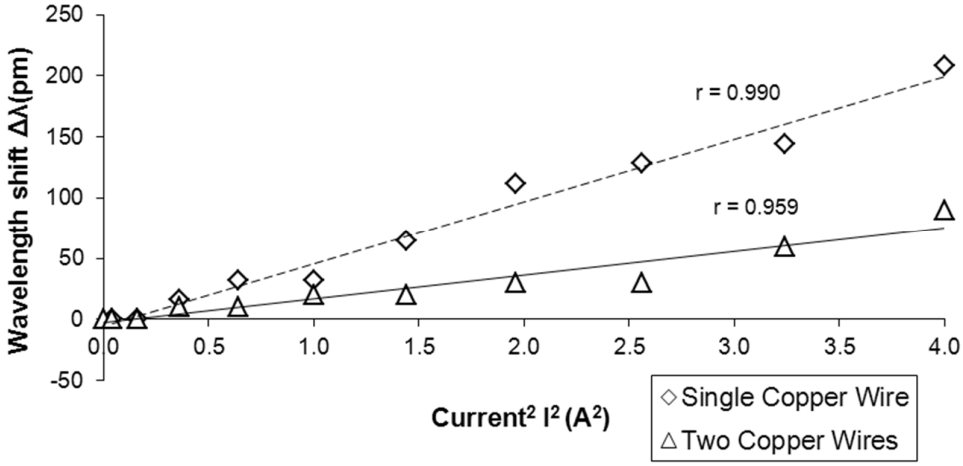

Figure 5.17: Current response of MKRs based on single-wire and two-wire configurations. The calculated resistance of the single copper wire and two copper wire are 0.53 $\Omega \cdot m^{-1}$ and 0.26 $\Omega \cdot m^{-1}$ respectively.

5.4 Summary

The applications of microfiber based devices have been demonstrated and discussed in this chapter. First of all, a stable multi-wavelength fiber ring laser based on MLR is presented. To enhance the robustness of this optical filter, MLR was fabricated and embedded in a low refractive index UV-curable material. In the characterisation, the coupling ratio of the MLR is dependent on the input state of polarization. In relation with the resonance condition, the resonance extinction ratio of the MLR can be enhanced with the aid of PBS and it helps stabilizing the lasing wavelengths of the laser. On the other hand, PBS was used to create NPR induced intensity dependent loss in the laser cavity and to suppress the mode competition in the SOA due to the narrow wavelength spacing. A stable and power equalized multi-wavelength fiber laser spaced at 0.16 nm had been achieved with SNR of 25 dB.

An EDF-based multiwavelength laser is also demonstrated using MLR as a filter. To achieve oscillations for multiple wavelengths generation, MLR is used as a comb filter in both lasers. In comparison, the double pass system which was obtained by incorporating a fiber mirror in the single pass configuration provides a more stable flat top output spectrum with relatively higher number of lasing wavelengths. In this configuration, the wave in the cavity propagates through the HNLF twice and therefore the wave experiences twice as much of nonlinear effect. Strong nonlinear effect in the laser cavity can suppress the mode competition better and help stabilizing the laser oscillation in the cavity. In the analysis, phase mismatch among the oscillating wavelength in the HNLF is an important factor that determines the strength of FWM effect. Strong FWM effect occurs in the zero phase mismatched region. Although a wideband zero phase mismatch for a is highly impossible to obtain but strong FWM effect can still be obtained in near zero phase mismatched region especially in a HNLF of small dispersion slope like the one used in this experiment.

Then, an MLR was fabricated and packaged to investigate the temperature response of the transmission spectrum of the device for sensor application. A flame brushing method has been used to fabricate a microfiber, which is then coiled to form a loop resonator device. The device is embedded into low refractive index polymer for robustness. The spacing of the transmission comb spectrum of the MLR is observed to be unchanged with the temperature. However, the extinction ratio of the spectrum is observed to be linearly decreased with the temperature. The slope of the extinction ratio reduction against temperature was about 0.043 dB/°C. The dependence of the extinction ratio on temperature is due to the thermo-optic and thermal-expansion effects. As an alternative to sensor model that based on spectral shift in microfiber resonators, this model is based on the variation of resonance extinction ratio in response to the temperature change. The measurement of extinction ratio is obviously easier and less complicated than that of resonance wavelengths. The operating cost for this sensor can be made lower because of the simple operating mechanism.

Finally, a compact current sensor is demonstrated using a MKR which is obtained by manipulating freestanding silica microfiber. With the assistance of a copper wire that is wrapped by the microfiber knot, resonance wavelength inside the MKR can be tuned by applying electric current to the copper wire. The wavelength shift is due to thermally induced phase shifts as a result of heat produced by the current flow. The theoretical and experimental analysis suggests that the tuning slope of the MKR can be manipulated by using different cross-sectional area and resistivity of the conductor wire. It is shown experimentally that the wavelength shift is linearly proportional to square of the amount of current. The tuning slope of 51.3 pm/A^2 based on single copper wire configuration has also been demonstrated. Besides being used as current sensors, these modified MKRs can be used as low-cost and fast response tunable optical filters

which are useful in the applications of optical signal processing, WDM communication and etc.

References

[1] M. Sumetsky, Y. Dulashko, J. M. Fini, A. Hale, and D. J. DiGiovanni, "The microfiber loop resonator: theory, experiment, and application," *Lightwave Technology, Journal of*, vol. 24, no. 1, pp. 242-250, 2006.

[2] M. Sumetsky, R. S. Windeler, Y. Dulashko, and X. Fan, "Optical liquid ring resonator sensor," *Opt. Express*, vol. 15, no. 22, pp. 14376-14381, 2007.

[3] F. Xu, P. Horak, and G. Brambilla, "Optical microfiber coil resonator refractometric sensor," *Opt. Express*, vol. 15, no. 12, pp. 7888-7893, 2007.

[4] X. Zeng, Y. Wu, C. Hou, J. Bai, and G. Yang, "A temperature sensor based on optical microfiber knot resonator," *Optics Communications*, vol. 282, no. 18, pp. 3817-3819, 2009.

[5] H. Ahmad, K. Thambiratnam, A. H. Sulaiman, N. Tamchek, and S. W. Harun, "SOA-based quad-wavelength ring laser," *Laser Physics Letters*, vol. 5, no. 10, pp. 726-729, 2008.

[6] S. Shahi, S. W. Harun, and H. Ahmad, "Multi-wavelength Brillouin fiber laser using a holey fiber and a bismuth-oxide based erbium-doped fiber," *Laser Physics Letters*, vol. 6, no. 6, pp. 454-457, 2009.

[7] S. Shahi, S. W. Harun, A. H. Sulaiman, K. Thambiratnam, and H. Ahmad, "Multiwavelength source based on SOA and EDFA in a ring-cavity resonator," *Microwave and Optical Technology Letters*, vol. 51, no. 1, pp. 110-113, 2009.

[8] X. Dong, P. Shum, N. Q. Ngo, and C. C. Chan, "Multiwavelength Raman fiber laser with a continuously-tunable spacing," *Opt. Express*, vol. 14, no. 8, pp. 3288-3293, 2006.

[9] M. H. Al-Mansoori, B. Bouzid, B. M. Ali, M. K. Abdullah, and M. A. Mahdi, "Multi-wavelength Brillouin-Erbium fibre laser in a linear cavity," *Optics Communications*, vol. 242, no. 1-3, pp. 209-214, 2004.

[10] Z. Zhang, J. Wu, K. Xu, X. Hong, and J. Lin, "Tunable multiwavelength SOA fiber laser with ultra-narrow wavelength spacing based on nonlinear polarization rotation," *Opt. Express,* vol. 17, no. 19, pp. 17200-17205, 2009.

[11] X. Feng, H.-y. Tam, and P. K. A. Wai, "Stable and uniform multiwavelength erbium-doped fiber laser using nonlinear polarization rotation," *Opt. Express,* vol. 14, no. 18, pp. 8205-8210, 2006.

[12] C. H. Yeh, C. W. Chow, Y. F. Wu, F. Y. Shih, C. H. Wang, and S. Chi, "Multiwavelength erbium-doped fiber ring laser employing Fabry-Perot etalon inside cavity operating in room temperature," *Optical Fiber Technology,* vol. 15, no. 4, pp. 344-347, 2009.

[13] H. Ahmad, A. Sulaiman, S. Shahi, and S. Harun, "SOA-based multi-wavelength laser using fiber Bragg gratings," *Laser Physics,* vol. 19, no. 5, pp. 1002-1005, 2009.

[14] H.-L. An, Lin, Xiang-Zhi and Liu, Hong-Du "Multi-wavelength Operation of an Er 3+ -doped Fiber Laser at Room Temperature with a Novel Optical Fiber Mach-Zehnder Interferometer," *Chinese Physics Letters,* vol. 17, no. 2, p. 106, 2000.

[15] H. Ahmad, N. S. Shahabuddin, A. A. Rahman, K. Thambiratnam, and S. W. Harun, "SOA-based multi-wavelength source," *Journal of Modern Optics,* vol. 55, no. 14, pp. 2179 - 2185, 2008.

[16] F. Xu and G. Brambilla, "Embedding optical microfiber coil resonators in Teflon," *Opt. Lett.,* vol. 32, no. 15, pp. 2164-2166, 2007.

[17] T. Bricheno and V. Baker, "All-fibre polarisation splitter/combiner," *Electronics Letters,* vol. 21, no. 6, pp. 251-252, 1985.

[18] C.-L. Chen and W. K. Burns, "Polarization Characteristics of Single-Mode Fiber Couplers," *Microwave Theory and Techniques, IEEE Transactions on,* vol. 30, no. 10, pp. 1577-1588, 1982.

[19] S.-W. Yang and H.-C. Chang, "Numerical modeling of weakly fused fiber-optic polarization beamsplitters. I. Accurate calculation of coupling coefficients and form birefringence," *Lightwave Technology, Journal of,* vol. 16, no. 4, pp. 685-690, 1998.

[20] Y. Jian, Y. Jianping, D. Zhichao, and L. Jian, "Multiwavelength erbium-doped fiber ring laser incorporating an SOA-based phase Modulator," *Photonics Technology Letters, IEEE,* vol. 17, no. 4, pp. 756-758, 2005.

[21] S. Yamashita and K. Hotate, "Multiwavelength erbium-doped fibre laser using intracavity etalon and cooled by liquid nitrogen," *Electronics Letters,* vol. 32, no. 14, pp. 1298-1299, 1996.

[22] X.-M. Liu, "Four-wave mixing self-stability based on photonic crystal fiber and its applications on erbium-doped fiber lasers," *Optics Communications,* vol. 260, no. 2, pp. 554-559, 2006.

[23] X. Liu, X. Yang, F. Lu, J. Ng, X. Zhou, and C. Lu, "Stable and uniform dual-wavelength erbium-doped fiber laser based on fiber Bragg gratings and photonic crystal fiber," *Opt. Express,* vol. 13, no. 1, pp. 142-147, 2005.

[24] M. Tang, X. Tian, P. Shum, S. Fu, H. Dong, and Y. Gong, "Four-wave mixing assisted self-stable 4×10 GHz actively mode-locked Erbium fiber ring laser," *Opt. Express,* vol. 14, no. 5, pp. 1726-1730, 2006.

[25] X. Xiaochuan, Y. Yong, Z. Xinhui, and C. Deying, "Multiple Four-Wave-Mixing Processes and Their Application to Multiwavelength Erbium-Doped Fiber Lasers," *Lightwave Technology, Journal of,* vol. 27, no. 14, pp. 2876-2885, 2009.

[26] X. Xu, Y. Yao, and D. Chen, "Numerical analysis of multiwavelength erbium-doped fiber ring laser exploiting four-wave mixing," *Opt. Express,* vol. 16, no. 16, pp. 12397-12402, 2008.

[27] A. Zhang, M. S. Demokan, and H. Y. Tam, "Room temperature multiwavelength erbium-doped fiber ring laser using a highly nonlinear photonic crystal fiber," *Optics Communications,* vol. 260, no. 2, pp. 670-674, 2006.

[28] Y.-G. Han and S. B. Lee, "Flexibly tunable multiwavelength erbium-doped fiber laser based on four-wave mixing effect in dispersion-shifted fibers," *Opt. Express,* vol. 13, no. 25, pp. 10134-10139, 2005.

[29] H. Ahmad, C. Wu Yi, K. Thambiratnam, M. Z. Zulklifi, P. Poopalan, M. M. M. Thant, and S. W. Harun, "High Sensitivity Fiber Bragg Grating Pressure Sensor Using Thin Metal Diaphragm," *Sensors Journal, IEEE,* vol. 9, no. 12, pp. 1654-1659, 2009.

[30] X. Fei, P. Valerio, F. Vittoria, and B. Gilberto, "High Sensitivity Refractometric Sensor Based on Embedded Optical Microfiber Loop Resonator," 2008, p. CMJ7.

[31] J. Lou, L. Tong, and Z. Ye, "Modeling of silica nanowires for optical sensing," *Opt. Express,* vol. 13, no. 6, pp. 2135-2140, 2005.

[32] V. Minkovich, J. Villatoro, D. Monzón-Hernández, S. Calixto, A. Sotsky, and L. Sotskaya, "Holey fiber tapers with resonance transmission for high-resolution refractive index sensing," *Opt. Express,* vol. 13, no. 19, pp. 7609-7614, 2005.

[33] H. C. Nguyen, B. T. Kuhlmey, E. C. Mägi, M. J. Steel, P. Domachuk, C. L. Smith, and B. J. Eggleton, "Tapered photonic crystal fibres: properties, characterisation and applications," *Applied Physics B: Lasers and Optics,* vol. 81, no. 2, pp. 377-387, 2005.

[34] J. Villatoro, V. P. Minkovich, and D. Monzón-Hernández, "Temperature-independent strain sensor made from tapered holey optical fiber," *Opt. Lett.,* vol. 31, no. 3, pp. 305-307, 2006.

[35] Y. Wu, Y.-J. Rao, Y.-h. Chen, and Y. Gong, "Miniature fiber-optic temperature sensors based on silica/polymer microfiber knot resonators," *Opt. Express,* vol. 17, no. 20, pp. 18142-18147, 2009.

[36] K. Su-Ah, J. Seongmin, P. R. Watekar, K. Youngwoong, and H. Won-Taek, "Faraday effect of twisted single mode fiber upon changing the effective length under magnetic field," in *OptoeElectronics and Communications Conference (OECC), 2010 15th*, 2010, pp. 356-357.

[37] X. Guo, Y. Li, X. Jiang, and L. Tong, "Demonstration of critical coupling in microfiber loops wrapped around a copper rod," *Applied Physics Letters,* vol. 91, no. 7, pp. 073512-3, 2007.

[38] F. Bilodeau, K. O. Hill, S. Faucher, and D. C. Johnson, "Low-loss highly overcoupled fused couplers: fabrication and sensitivity to external pressure," *Lightwave Technology, Journal of,* vol. 6, no. 10, pp. 1476-1482, 1988.

[39] X. Jiang, L. Tong, G. Vienne, X. Guo, A. Tsao, Q. Yang, and D. Yang, "Demonstration of optical microfiber knot resonators," *Applied Physics Letters,* vol. 88, no. 22, pp. 223501-223501-3, 2006.

[40] L. Zhang, J. Lou and Limin Tong, "Micro/nanofiber optical sensors," Photonic Sensors,Vol. 1, No. 1, pp. 31-42, 2011

Chapter 6

CONCLUSION AND FUTURE WORK

6.1 Conclusion

Tapered fibers have been intensively studied due to their high nonlinearity, dispersion time-ability, evanescent fields, and three dimensional assemble capability, which can be used for fabricating various fiber-optic devices including an ultra-broad super-continuum light. Tapered silica fiber offers an advantage of the ease of integration with single mode fiber (SMF) for low-loss optical transmission. The access to the evanescent field can be achieved by tapering as the light is guided by the boundary between the taper and the ambient medium. The refractive index of the ambient medium can be chosen to select the number of modes exist within the taper waist. Recent research on optical resonators has shown a great deal of promise for a variety of applications such as laser resonator, photonics biosensor and optical switching. These devices can be constructed in a variety of sizes using a planar waveguide technology or all-fiber approach.

In this thesis, the research started with the fabrication of microfibers using flame brushing technique. To achieve that, a fiber tapering rig was assembled from oxy-butane burner with small flame size, long linear stages, high precision stepper motors and a microcontroller that interface with a computer to realize high precision microfibers fabrication. Low loss tapered fiber should be fabricated according to the adiabaticity criteria. The shape of the tapered fiber should be formed in such a way that the rate of change of any local radius is small enough to prevent the exchange of power between fundamental mode and its closest higher order mode. Adiabatic tapered fibers are

employed as building components for microfiber photonic devices including MLRs, MKRs and MMZIs. The low connection loss between microfibers and SMF has enabled assembly of low-loss microfiber devices.

Packaging

Tapered fibers and microfiber devices are susceptible to the environmental perturbations, dust and water moisture when they are exposed to the air. The throughput power of the tapered fibers and microfiber devices degrades over time as the deposition of dust and water moisture from the air on the glass surface of the tapered fiber increases monotonically. The air turbulence often affects the resonance and coupling condition of the microfiber devices and perpetually disrupts the output performance of these devices. In addition, the mechanical crack may be introduced to the tapered fibers that sway in the air due to the strong air-turbulence and this damage is unrecoverable. An experiment was conducted to investigate the throughput variation of a tapered fiber in the air. It was found that the throughput power decreases monotonically over time and no power was detected after 350 minutes.

Two protective methods were demonstrated in this work to provide long term protection to the tapered fibers and microfiber devices. The first method is to embed the device in low-index resin. First, the newly fabricated microfiber device is embedded in a liquid low-index resin. Then, the resin is solidified when exposure to the UV-light for 3-7 minutes. After that, the structure and optical characteristics of the embedded microfiber device are maintained in the solidified resin. This process involves changing the refractive index of the ambient medium thus changing the characteristic parameters of the embedded microfiber devices. In the case of microfiber resonators, the low-index resin that replaces the air at the surrounding of the microfiber may alter the initial numerical aperture (NA), mode field diameter (MFD), coupling and resonance state of

the embedded resonators. It was demonstrated that this embedding method is very useful for providing protection to the microfiber devices. The other method does not involve any chemical resin but to use a long Acrylic casing in packaging along tapered fiber. The tapered fiber is kept straight and surrounded by air when packaged in the Acrylic casing. The untapered parts of the tapered fiber are the only parts in contact with the Acrylic casing. Thus the transmission of light through the tapered fiber is unaffected. In the last process, a thin plastic wrap is used to enwrap the entire Acrylic casing together with the packaged tapered fiber. This is to keep tapered fiber from the dust and water moisture on the outside. The lifespan of the tapered fiber can be extended from a few hours to a couple of weeks.

One of the unique characteristics of tapered fiber is its chromatic dispersion and the understanding of this characteristic is important for prior to the employment of tapered fiber in other applications including supercontinuum generation, four-wave mixing, dispersion compensation and etc. An experimental setup based on Michelson Interferometry was constructed to measure the dispersion coefficient of a ~2 μm diameter and 8.5 cm long tapered fiber. It is found that the measured dispersion coefficient *D*, 242 ps/(nm.km) is in agreement with the calculated dispersion coefficient, 260 ps/(nm.km).

Microfiber Devices

Three different microfiber devices were experimentally demonstrated in this work, namely MLRs, MKRs and MMZIs. MLRs and MKRs share the same theoretical model as their operating principles are based on self-touching configuration. MLRs and MKRs of different loop / knot diameters have been experimentally demonstrated. Comparing the two resonators, MKRs outperform MLRs in terms of resonance stability and coupling due to its close contact between the two coupling microfibers in the

structure of the device. The structure of MKR is more rigid and robust with the interfiber twisted coupling. Therefore, it is easier to assemble small diameter MKRs if compared with MLRs. However, MKR has higher insertion loss compared to MLR because of the cut-coil-couple process in the fabrication of MKR. To achieve in-depth understanding on characteristics of these microfiber devices, a new analytical method based on curve-fitting technique is suggested. By curve-fitting the transmission spectra acquired from the experiment with the transfer function derived from the theoretical model, the important characteristic parameters can be extracted from the best-fit curve. Consider the case of microfiber resonators, the coupling parameter, $\sin\kappa\ell$ and round-trip attenuation factor, $e^{-\alpha L/2}$ extracted from the experimental data may provide important information about the resonance condition of the resonators. Critical coupling occurs when the coupling parameter matches with round-trip attenuation factor and the resonance extinction ratio is optimum in this condition. In the investigation of the characteristics of an MKR immersed in several liquid solutions of different refractive indices, the experimental data was analysed using curve-fitting technique. The characteristic parameters varied when immersed in the liquids. As the result of lower index contrast between silica and surrounding medium, the coupling parameter was increased while the round-trip attenuation factor is reduced. The difference between coupling parameter and round-trip attenuation factor was reduced and resonance state was brought closer to critical coupling. In the first experiment, the extracted parameters from the transmission spectrum of an MKR were $\sin\kappa\ell = 0.6207$ and $e^{-\alpha L/2} = 0.8547$. The parameters changed to $\sin\kappa\ell = 0.6762$ and $e^{-\alpha L/2} = 0.8361$ when the MKR was immersed in the propan-2-ol solution. The resonance extinction ratio (RER) of the MKR had improved from ~5 dB to ~8 dB. The reduction in round-trip attenuation factor can be attributed to the higher bending loss at the microfiber knot in a smaller index contrast environment. However, there was a scenario where smaller RER was obtained.

In another experiment, an MKR was immersed in the water, $\sin\kappa\ell$ varied from 0.6235 to 0.7833 while $e^{-\alpha L/2}$ varied from 0.8145 to 0.9339. RER has dropped from ~4 dB to ~2.5 dB.

Microfiber resonators exhibit several interesting characteristics related to polarization and temperature. In the investigation of polarization dependent characteristic, the RER of output spectrum can be varied by changing the input state of polarization using a polarization controller (PC) at the input of the microfiber resonator. In the experiment, it was found that the RER of MLRs could vary as much as 6 dB between 5 dB and 11 dB. This property can be used to optimize the resonance extinction ratio. Silica microfibers have a strong dependence on temperature. The resonance wavelength can be expressed in a function of temperature. In the analysis, the result indicates that resonance wavelength shifts linearly with the change of temperature with a slope of 50.6 pm/°C. This characteristic can be well explained with thermal-optic effect and thermal expansion effect in silica glass.

In the work, MMZIs of different path length differences ΔL are also fabricated and theoretically studied. To assist theoretical analysis, the theoretical model of the MMZI is reviewed. Some characteristic equations were derived based on the theoretical model and compared with the transmission spectrum obtained in the experiment. In the analysis, the wavelength spacing was found to be inversely proportional to path length difference which is in agreement with the theoretical model. In the investigation of the MMZI performance in the air, RER was observed to be influenced by the air-turbulence. It varied with the change of the position of the bent arm but the wavelength spacing was unaffected by the unrest.

Applications

Several applications of microfiber resonators have been investigated in this thesis. In a multiwavelength semiconductor optical amplifier (SOA) laser system, an MLR with a free spectral range (FSR) of 0.16 nm was used as a comb filter in the laser cavity to slice the amplified spontaneous emission (ASE) from the gain medium into many channels with equal wavelength spacing. The MLR with such small FSR is firstly fabricated. Polarization beam splitter (PBS) was used to create an NPR induced intensity dependent loss in the laser cavity to suppress the mode competition among the wavelengths with narrow spacing in the SOA. To compensate the inadequacy of extinction ratio of the MLR, PC was incorporated in the ring cavity to optimize the extinction ratio and achieved better lasing stability. In another experiment, an MLR with the similar FSR was used as a comb filter to generate multiwavelength laser in which Erbium-doped fiber (EDF) was used as the gain medium. It is common known that, EDF is a homogenous gain medium, strong mode competition among the wavelengths in the medium. Simultaneous wavelength lasing is highly unstable particularly if the spacing between two adjacent wavelengths is within the homogenous linewidth. Highly nonlinear fiber (HNLF) was incorporated in the system to induce degenerate four-wave mixing (FWM) among the lasing wavelengths. A total number of 19 lasing wavelengths with an average output power of -15.2 dBm and peak power difference of less than 5 dBm are produced. This effect improved the power distribution among the wavelengths and enhanced the lasing stability.

The temperature dependent characteristics of microfiber devices are found useful particularly in the sensor applications. Generally, the temperature response can be determined based on resonance wavelength shift and resonance extinction ratio. The former one has been reviewed in the earlier discussion. In the investigation of resonance extinction ratio with temperature change, it was observed that the resonance extinction

ratio was linearly decreasing with increasing temperature at a rate of 0.043 dB/°C but the FSR was unaffected by the temperature change. Besides temperature sensor, temperature dependent characteristic can be exploited in the current sensor application. A compact current sensor based on a copper wire wrapped by an MKR was experimentally demonstrated. The resonance wavelength of the MKR can be tuned by applying electric current to the copper wire. The wavelength shift is due to thermally induced optical phase shifts, a result of heat produced by the current flow. The tuning slope of the MKR can be controlled by using different cross-sectional area and resistivity of the conductor wire. It was found that the tuning slopes for single-wire and two-wire configurations were 51.3 pm/A^2 and 19.5 pm/A^2 respectively. This modified MKR can be used as low-cost and fast response tunable optical filters which are useful in the applications of optical signal processing, wavelength division multiplexing (WDM) communication and etc.

In conclusion, the fabrication techniques developed and practiced for the manufacture of microfibers and microfiber devices had been experimentally demonstrated and investigated in this work. The good quality microfiber devices are assembled from low-loss tapered fiber. Characteristic equations derived from the theoretical model for various microfiber devices are reviewed. The experimental results are analysed in accompanied with the theoretical result to achieve more in-depth understanding on these microfiber devices. In the investigation, several characteristics of microfiber devices particularly MLR and MKR have been observed and exploited in multiwavelength laser systems and sensor applications in this research. The experiments have shown promising results and they are very encouraging. In overall, this research on microfiber devices has been a great success.

6.2 Future Work

In future, more advanced fabrication techniques should be developed to simplify the fabrication process and to increase the success rate. Mass production for microfiber devices (except couplers) remains a challenge. Different microfiber structures should be explored and investigated to enrich the list of microfiber devices such as coil resonator, loop mirror and coupler. Effort should be put into expanding and improving the functionalities of these microfiber devices. One of the obstacles in developing more complex microfiber structures is the difficulty in reducing the excess loss of the microfiber devices. Worse still, higher loss will be introduced into the devices when embedded in a low-index material for the protection of microfiber devices. Different technique or material should be opted and attempted to achieve low loss for the embedding process.